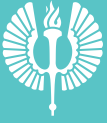

TURUN YLIOPISTO
UNIVERSITY OF TURKU

MEMRISTOR DEVICES BASED ON LOW-BANDWIDTH MANGANITES

Ville Lähteenlahti

TURUN YLIOPISTON JULKAISUJA – ANNALES UNIVERSITATIS TURKUENSIS
SARJA – SER. AI OSA – TOM. 679 | ASTRONOMICA – CHEMICA – PHYSICA – MATHEMATICA | TURKU 2022

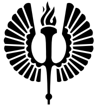

TURUN
YLIOPISTO
UNIVERSITY
OF TURKU

MEMRISTOR DEVICES BASED ON LOW-BANDWIDTH MANGANITES

Ville Lähteenlahti

TURUN YLIOPISTON JULKAISUJA – ANNALES UNIVERSITATIS TURKUENSIS
SARJA – SER. AI OSA – TOM. 679 | ASTRONOMICA – CHEMICA – PHYSICA – MATHEMATICA | TURKU 2022

University of Turku

Faculty of Science
Department of Physics and Astronomy
Physics
Doctoral Programme in Exact Sciences

Supervised by

Prof. Petriina Paturi
Wihuri Physical Laboratory
Dept. of Physics and Astronomy
University of Turku
Turku, Finland

Dr. Hannu Huhtinen
Wihuri Physical Laboratory
Dept. of Physics and Astronomy
University of Turku
Turku, Finland

Dr. Alejandro Schulman
Wihuri Physical Laboratory
Dept. of Physics and Astronomy
University of Turku
Turku, Finland

Reviewed by

Prof. Tamalika Banerjee
Zernike Institute for Advanced Materials
University of Groningen
Groningen, Netherlands

Dr. Diego Rubi
Laboratorio de Ablación Láser
Instituto de Nanociencia y Nanotecnologia
CNEA-CONICET
San Martín, Argentina

Opponent

Dr. Felix Gunkel
Peter Grünberg Institute
Forschungszentrum Jülich
Jülich, Germany

The originality of this publication has been checked in accordance with the University of Turku quality assurance system using the Turnitin OriginalityCheck service.

ISBN 978-951-29-9072-6 (PRINT)
ISBN 978-951-29-9073-3 (PDF)
ISSN 0082-7002 (PRINT)
ISSN 2343-3175 (ONLINE)
Painosalama, Turku, Finland, 2022

UNIVERSITY OF TURKU
Faculty of Science
Department of Physics and Astronomy
Physics
VILLE, LÄHTEENLAHTI: Memristor devices based on low-bandwidth manganites
Doctoral dissertation, 89 pp.
Doctoral Programme in Exact Sciences
December 2022

ABSTRACT

This dissertation investigates the phenomenon of resistive switching (RS) in low-bandwidth mixed-valence perovskite manganite oxides. In particular, the compounds $Pr_{0.6}Ca_{0.4}MnO_3$ and $Gd_{1-x}Ca_xMnO_3$ with x between 0 and 1 are studied. The steps of sample fabrication, crystalline properties and measurements to verify the quality of the devices are also reported. The thin film memristor devices were fabricated from target pellets using pulsed laser deposition on single crystal $SrTiO_3$ substrates. The crystallinity was verified using X-ray diffraction and the elemental composition by energy dispersive X-ray spectroscopy. The fabricated thin films were used to create memristor devices by depositing patterned metal electrodes on them by either DC magnetron sputtering or e-beam physical vapor deposition.

When the studied materials were combined with a reactive electrode material, the formed interface exhibited the phenomenon of resistive switching, where the resistance of the device can be modified non-volatilely by application of electric field to the terminals of the device. The noble metals Au and Ag were found to be optimal for the passive interfaces, and Al as the active interface. The RS properties of the devices made with the optimal electrode configuration were studied in detail. The devices were found to have asymmetric bipolar RS with promising characteristics. The studies encompassed varying the calcium doping of the samples, studying the endurance and timing characteristics of the RS phenomenon as well as measuring the device characteristics as a function of temperature. The RS properties were found to vary significantly over the calcium doping range. When the measurement results were used in a conduction model analysis, the switching properties were found to be correlated with the trap-energy level of the Al/GCMO-interface region. Lastly, the GCMO memristor devices were modeled successfully using a compact model compatible with circuit simulators and the biologically-inspired spike-timing-dependent plasticity learning rule was demonstrated.

In conclusion, GCMO is a promising new material for RS-based neuromorphic applications due to its stable switching properties. The unexpected differences between GCMO and PCMO show that there are still many unexplored RS properties and behaviors within the manganite family that can be explored in future research.

KEYWORDS: manganite, thin film, memristor, resistive switching

TURUN YLIOPISTO
Matemaattis-luonnontieteellinen tiedekunta
Fysiikan ja tähtitieteen laitos
Fysiikka
VILLE, LÄHTEENLAHTI: Memristor devices based on low-bandwidth manganites
Väitöskirja, 89 s.
Eksaktien tieteiden tohtoriohjelma
Joulukuu 2022

TIIVISTELMÄ

Tässä väitöskirjassa tutkitaan resistiivisen kytkennän (RS) ilmiötä matalan elektronikaistan sekavalenssisissa perovskiittimanganiittioksideissa. Erityisesti tutkitaan yhdisteitä $\mathrm{Pr_{0.6}Ca_{0.4}MnO_3}$ ja $\mathrm{Gd_{1-x}Ca_xMnO_3}$ useilla kalsiumsubstituutioilla x. Lisäksi raportoidaan näytteiden valmistusvaiheet, kiteiset ominaisuudet ja mittaukset laitteiden laadun varmistamiseksi. Ohutkalvomemristorilaitteet valmistettiin kohdepelleteistä pulssilaserpinnoituksella yksikiteisille $\mathrm{SrTiO_3}$-substraateille. Kiteisyys todennettiin röntgendiffraktiolla ja alkuainekoostumus energiadispersiivisellä röntgenspektroskopialla. Valmistettuja ohutkalvoja käytettiin memristorilaitteiden valmistamiseen pinnoittamalla ne kuvioiduilla metallielektrodeilla joko tasavirtamagnetronisputteroinnilla tai elektronisäteeseen perustuvalla fysikaalisella höyrystyspinnoituksella.

Kun tutkitut materiaalit yhdistettiin reaktiiviseen elektrodimateriaaliin, muodostuneessa rajapinnassa esiintyy resistiivisen kytkennän ilmiö, jossa laitteen resistanssia voidaan muuttaa hallitusti kohdistamalla sähkökenttä laitteen yli. Erilaisia elektrodiyhdistelmiä tutkittiin, ja jalometalleista Au ja Ag todettiin optimaalisiksi passiivisiksi rajapinnoiksi ja Al aktiiviseksi rajapinnaksi. Optimaalisilla elektrodeilla valmistettujen laitteiden RS-ominaisuuksia tutkittiin yksityiskohtaisesti. Laitteiden toiminta todettiin epäsymmetriseksi bipolaariseksi resistiiviseksi kytkennäksi lupaavin ominaisuuksin. Tutkimukset kattoivat näytteiden kalsiumsubstituution muuttamisen, RS-ilmiön kestävyys- ja ajoitusominaisuuksien tutkimisen sekä laitteen ominaisuuksien mittaamisen lämpötilan funktiona. RS-ominaisuuksien havaittiin vaihtelevan merkittävästi kalsiumsubstituution funktiona. Kun mittaustuloksia käytettiin johtavuusmallianalyysissä, kytkentäominaisuuksien havaittiin korreloivan Al/GCMO-rajapinta-alueen loukkuenergiatason kanssa. Lopuksi GCMO-memristorilaitteet mallinnettiin onnistuneesti käyttäen piirisimulaattoreiden kanssa yhteensopivaa kompaktia mallia ja laitteissa demonstroitiin piikittävien neuroverkkojen piikkien ajoituksesta riippuvan plastisuuden oppimissääntö.

Yhteenvetona voidaan todeta, että GCMO on lupaava uusi materiaali RS-pohjaisiin neuromorfisiin sovelluksiin sen vakaiden kytkentäominaisuuksien ansiosta. GCMO:n ja PCMO:n väliset erot osoittavat, että manganiittiperheessä on vielä monia tutkimattomia RS-ominaisuuksia ja käyttäytymismalleja.

ASIASANAT: manganiitti, ohutkalvo, memristori, resistiivinen kytkentä

Acknowledgements

I wish to thank Prof. Tamalika Banerjee and Dr. Diego Rubi for the reviewing of this dissertation and Dr. Felix Gunkel, it is an honor to have you as my opponent. I would also like to express my gratitude to Dr. Alejandro Schulman for being an excellent supervisor, Prof. Petriina Paturi and Dr. Hannu Huhtinen for guiding and shaping my skills as a physicist over the years, and warm thanks go to all the other people who worked at the laboratory during my years at Wihuri.

The research was carried out at the Wihuri Physical Laboratory, Department of Physics and Astronomy, University of Turku during the years 2018 – 2021. The Academy of Finland, University of Turku Graduate School's Doctoral Program and the Jenny and Antti Wihuri Foundation are acknowledged for their financial support.

July 2022
Ville Lähteenlahti

Table of Contents

Acknowledgements . . . . **v**

Table of Contents . . . . **vi**

List of Original Publications . . . . **viii**

1 Introduction **1**
- 1.1 Motivation 1
- 1.2 History of resistive switching 2
- 1.3 Resistive switching in transition metal oxides 3
  - 1.3.1 Physical mechanism 3
- 1.4 Mixed-valence manganites 5
  - 1.4.1 $Pr_{1-x}Ca_xMnO_3$ 8
  - 1.4.2 $Gd_{1-x}Ca_xMnO_3$ 8
  - 1.4.3 Conduction mechanisms in oxide materials 9
  - 1.4.4 Resistive switching in mixed-valence manganites 10
- 1.5 Applications of resistive switching 10

2 Experimental details **13**
- 2.1 Physical vapor deposition 13
  - 2.1.1 Pulsed laser deposition 13
  - 2.1.2 Magnetron sputter deposition 14
  - 2.1.3 Electron-beam physical vapor deposition 16
- 2.2 Thin film characterization 17
  - 2.2.1 X-ray diffraction 17
  - 2.2.2 Energy-dispersive X-ray spectroscopy 19
- 2.3 Device patterning and preparation 19
- 2.4 Data acquisition 20
  - 2.4.1 Measurement sequences 21

3 Thin film properties **25**
- 3.1 Memristor fabrication process 25
- 3.2 Assessing device quality 27

3.3 Phase diagram of the GCMO 28

4 Resistive switching properties 30

4.1 Characterization of resistive switching 32

4.2 Effect of calcium composition 33

4.3 Comparison to other manganites 34

4.4 Endurance characteristics 34

4.5 Control of resistive states 36

5 Models and simulations 39

5.1 Conduction behavior 39

5.1.1 Conduction model 41

5.1.2 Model fit results 42

5.2 Compact modeling 44

5.2.1 The memdiode model 45

5.2.2 Applying the model to the GCMO device 49

5.3 Spike-timing-dependent plasticity 51

6 Conclusions 53

List of References 54

Original Publications 61

List of Original Publications

This dissertation is based on the following original publications:

I V. Lähteenlahti, A. Schulman, H. Huhtinen and P. Paturi: *Transport Properties of Resistive Switching in Ag/$Pr_{0.6}Ca_{0.4}MnO_3$/Al Thin Film Structures*, Journal of Alloys and Compounds, 786, 84–90 (2019).

II A. Schulman, A. Beiranvand, V. Lähteenlahti, H. Huhtinen and P. Paturi : *Appearance of glassy ferromagnetic behavior in $Gd_{1-x}Ca_xMnO_3$($0 \leq x \leq 1$) thin films: A revised phase diagram*, Journal of Magnetism and Magnetic Materials, 498, 166149 (2020).

III V. Lähteenlahti, A. Schulman, A. Beiranvand, H. Huhtinen and P. Paturi: *Electron doping effect in resistive switching properties of Al/$Gd_{1-x}Ca_xMnO_3$-/Au memristor devices*, ACS Applied Materials & Interfaces, 13, 18365–18371 (2021).

IV E. Miranda, V. Lähteenlahti, H. Huhtinen, A. Schulman and P. Paturi: *Compact modeling and SPICE simulation of GCMO-based resistive switching devices*, IEEE Transactions on Nanotechnology, 21, 285–288 (2022).

Articles relevant to this work but not included in this dissertation:

V A. Schulman, H. Palonen, V. Lähteenlahti, A. Beiranvand, H. Huhtinen and P. Paturi : *Metastable ferromagnetic flux closure-type domains in strain relaxed $Gd_{0.1}Ca_{0.9}MnO_3$ thin films*, Journal of Physics: Condensed Matter, 33, 035803 (2020).

VI A. Beiranvand, M. Liedke, C. Haalisto, V. Lähteenlahti, A. Schulman, S. Granroth, H. Palonen, M. Butterling, A. Wagner, H. Huhtinen and P. Paturi : *Tuned AFM-FM coupling by the formation of vacancy complex in $Gd_{0.6}Ca_{0.4}MnO_3$ thin film lattice*, Journal of Physics: Condensed Matter 33, 255803 (2021).

VII A. Beiranvand, M. Liedke, C. Haalisto, V. Lähteenlahti, A. Schulman, S. Granroth, H. Palonen, M. Butterling, A. Wagner, H. Huhtinen and P. Paturi : *Manipulating magnetic and magnetoresistive properties by oxygen vacancy complexes in GCMO thin films*, Journal of Physics: Condensed Matter, 34, 155804 (2022).

The original publications have been reproduced with the permission of the copyright holders.

1 Introduction

1.1 Motivation

The advances in information technology and digitalization of society have resulted in an exponential increase in the total amount of information in circulation [1]. From the hardware point of view, this necessitates new approaches to data processing and storage, as the limits are being reached in the conventional charge-confinement based complementary metal oxide semiconductor devices (CMOS) [2]. The individual transistor devices are reaching their physical size limits, and the performance improvements of the last decade are mainly due to the downsizing and geometry changes of the gate dielectric.

From an architectural point of view the current computers also suffer from the von Neumann bottleneck, where the processing speed is fundamentally limited by the bus which connects central processing units and memory [3] (Fig. 1). To overcome the issue, the the trend has been to build multiple computation units which process given data in parallel and share a common memory. However, the separated computation units are not suitable for general purpose computation without complex interconnects, which enable communication between the units. This imposes limitations on the maximum number of computation units with current two-dimensional chip manufacturing techniques in the terms of latency, yield and power consumption constraints. To overcome the limitations of the von Neumann architecture, alternative approaches to computation are being explored with the aim of either complementing or replacing existing systems [4; 5; 6].

Neuromorphic devices and computer architectures show a possible way to overcome the current limitations by combining memory and computation. Neuromorphic circuits often consist of many simple interconnected units which can both hold state and perform computation locally without depending on the global state of the system [7]. These architectures often resemble the information processing schemes present in biological systems [7]. Various potential emerging technologies have been proposed to be used in the hardware implementation of the neuromophic computing, including devices based on phase change, resistivity change, spin-transfer torque magnetoresistance and ferroelectricity. Out of them, the resistivity change based resistive switching (RS) has gained steady traction owing to its promising characteristics, which have been found to be potentially more performant and efficient than the conventional CMOS-based devices [8; 9].

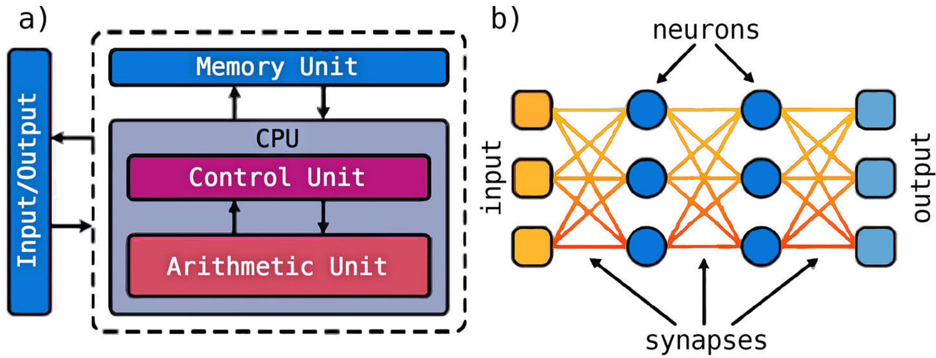

Figure 1. a) The von Neumann architecture with distinct processing and memory units. b) An example of a neuromorphic architecture.

1.2 History of resistive switching

The basic research on resistive switching devices has been active for decades, beginning with the observation of non-volatile $I(V)$-characteristics in Al/Al_2O_3/Al thin films in 1962 [10]. However, at the time, fabrication and characterization methods had not matured enough and the advances in silicon technology and computing overshadowed the interest to investigate the phenomenon further. The first theory for RS devices [11] was envisioned by Leon Chua in 1964 [12], as an exploration of a missing circuit element termed as memristor, which behaves like a non-linear resistor with a memory (the existing elements being the resistor, capacitor and inductor). Originally the theory postulated a missing circuit element which relates magnetic flux linkage to the electric charge, but later on the term was extended to encompass more general memristive systems [13]:

$$y(t) = g(x, u, t)$$
$$\frac{dx}{dt} = f(x, u, t),$$

where $u(t)$ is the input signal, $y(t)$ is the output signal, x is a variable describing the device state and f and g are continuous functions. The theory has been used as a basis for other models, such as the memdiode model discussed later in the context of compact modeling, and has been shown to reproduce real devices with convincing accuracy [14],**[IV]**.

Later on in year 2008, decades after the introduction of the Chua's memristor model, a team led by R. Stanley Williams at Hewlett-Packard Labs reported that they had fabricated a functioning Ti-based memristor [15; 16]. The announcement caught the attention of the public for the first time, and cemented memristor into the vocabulary of many scientifically-minded people. At the time various other materials were also being explored for their potential as RS devices. Naturally,

compounds which were already being used in semiconductor industry and material research were under close attention and yielded promising results, such as devices based on manganite oxides and HfO_2 [17; 18]. The advances in RS research have led to demonstrations in memory devices and biologically inspired computing devices [19] with high switching speeds, robust endurance, low power consumption, spatial scalability, persistent non-volatility and in some cases, compatibility with existing electronics [20; 21]. These characteristics make them an emerging technology with many favorable properties for use in future electronics.

1.3 Resistive switching in transition metal oxides

Resistive switching is a phenomenon where the resistance of a two-terminal device can be controlled non-volatilely by applying an electric field to its terminals. The electric field can be used to either modify the devices state, or to read the state non-destructively depending on the field amplitude and polarity. The resistance changes resulting from the application of the field are caused by structural modification of the device, in contrast to the conventional charge-based transistor technology, where the state is stored in confined electrical charge. As the materials studied in this dissertation are perovskite structured low-bandwidth transition metal oxides, the scope of the discussion will be constrained to RS devices based on transition-metal-oxides (TMO). Despite this, the presented explanations are often applicable to other RS materials.

1.3.1 Physical mechanism

The physical mechanism behind the phenomenon is rather complicated, but the main causes have been identified and grouped into two main mechanisms, electrochemical metallization based switching and valence-change based switching [22; 23]. However, even though the base framework for explaining the phenomenon exists, different interpretations are possible, and there is no unified procedure for measuring RS devices [24]. Additionally, the RS effect is dependent on the device design, and multiple different phenomena can cause the resistive switching depending on the sample geometry, fabrication parameters and the device state. Several models have been presented for the origin of the phenomenon in oxide-based devices, most of which explain the changes in resistance with the movement of oxygen vacancies [25; 26; 27; 28; 29; 30].

One of the two possible origins of non-volatile RS in TMO materials is caused by a local phase change from insulating to metallic (electrochemical metallization). The RS devices which utilize electrochemical metallization mechanism usually consist of capacitor structures of oxide layer between two electrodes, of which one is made from an active material, most commonly Ag or Cu. Upon application

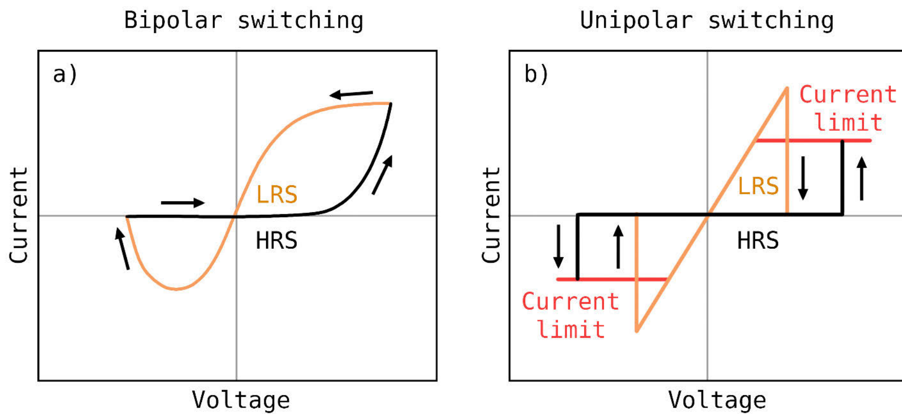

Figure 2. Simplified $I(V)$-behavior for unipolar and bipolar memristor devices. Unipolar switching does not depend on the polarity of the electric field, while bipolar switching does.

of electric field, the active material supplies cations, which migrate to the bulk of the oxide material, where they are reduced and nucleate to form metallic filaments [22; 31]. The subsequent application of the electric field then controllably dissolves and re-forms the weakest point of the percolation path [32], resulting in high resistance state (HRS) and low resistance state (LRS).

The other origin mechanism in TMO materials is called valence-change based switching, where the conductive pathway consist of either oxygen or oxygen vacancies, depending on the semiconductor type. In the valence-change-based devices the application of electric field causes migration of oxygen at the oxide/electrode-interface, which modulates properties of a Schottky-like barrier at the interface, changing the resistive state [22].

In some cases the switching has been linked to the simultaneous occurrence of both filament formation inside the RS oxide and interface oxygen stoichiometry changes [33; 34]. Studies have also observed switching based on phase changes [35; 32] and the transport of silver and copper ions [36; 37].

The two main mechanisms can result in two types of non-volatile $I(V)$-behavior: unipolar switching (often electrochemical metallization) and bipolar switching (valence-change). In bipolar switching the modification of the device state depends on the polarity and amplitude of the applied electric field, one polarity induces a change to low resistance state (LRS) and the other to high resistance state (HRS) (Fig. 2 a). Intermediate resistive states are also possible, and the switching amplitudes can be asymmetric. In the unipolar switching the device state is only dependent on the amplitude of the applied electric field, after a switching threshold a conducive filament is formed and the device transitions into LRS, after the voltage is applied again the filament dissolves at a different threshold resulting in HRS (Fig. 2 b). The formation and dissolution of the filament are independent

of field polarity. In unipolar switching, current limitation is important during the LRS transition in order to avoid device breakdown. Both phenomena can also be achieved using current-controlled field application instead of voltage control.

The two RS phenomena lie in the mesoscopic physics, which is an interesting intersection of macro- and microscales. The filament formation theories often draw concepts from mathematics of fractals and stochastic processes [32] and exhibit observable quantum effects. As an example, studies have been made which accurately measure individual quantum conductance steps in oxide RS devices [38; 39].

The bipolar and unipolar switching behaviors can be distinguished from their area scaling and capacitance properties in addition to their behavior when subjected to an electric field [22]. The bipolar switching from valence-change happens over the whole active interface, making it proportional to the interface area, whereas unipolar switching is localized to filaments in the nanometer-scale, resulting in lesser area dependence [22]. In some cases the switching can irreversibly change from bipolar to unipolar after an application of high field [40]. However, the bipolar switching tends to have better endurance characteristics, device-to-device variability, energy requirements [41] and sharper resistance distributions, which often makes it preferable over unipolar switching. However, the unipolar device performance can often be improved by via device shape and interface engineering [42].

Both bipolar and unipolar switching can benefit from device engineering, and many techniques to enhance the RS properties have been discovered [42]. In the case of manganites, changing the stoichiometry of the oxide material plays a major role in the resulting interface properties and filament formation [25; 43; 44], as the flexibility of the perovskite structure allows for substitution with materials of different properties without destroying the crystal structure. Other methods include the addition of buffer layers, doping of the electrode materials by introducing a homogeneous mixture, or by introduction of particle clusters. Particle clusters can be used to control and localize the formation of conductive filaments, these clusters dictate where the filament will form, leading to the possibility to have more control over the stochastic percolation formation process [45]. Adding an intermediate buffer layer between the RS oxide and electrode has also been found to improve the RS properties in some cases, as the buffer layer can be used to trap and control the oxygen movement in the device [45].

1.4 Mixed-valence manganites

The materials studied in this dissertation, $\mathrm{Gd_{1-x}Ca_xMnO_3}$ and $\mathrm{Pr_{1-x}Ca_xMnO_3}$ (GCMO and PCMO, respectively), both belong to the group of perovskite structured manganite compounds. The possible structural configurations of perovskite

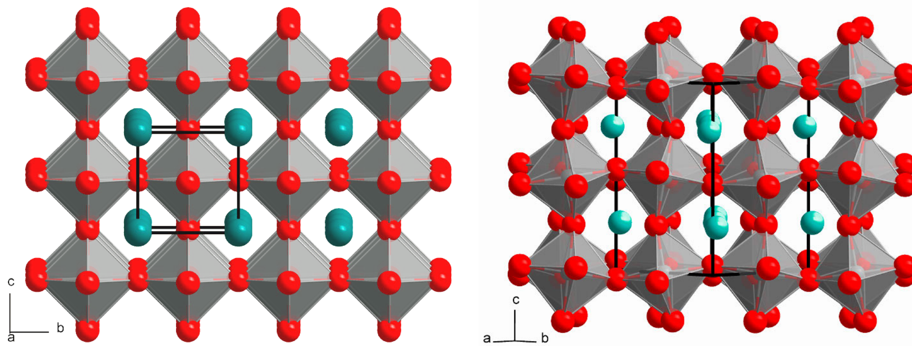

Figure 3. a) An ideal cubic perovskite structure. b) An example of distorted perovskite structure. A-sites are shown in teal and the X-sites which make up the octahedra around the B-site cations are shown in red. Figures from [46].

materials give rise to rich properties and interesting phenomena, such as charge ordering [47], ferroelectricity [48], Mott-transition [49], high temperature superconductivity [50] and colossal magnetoresistance [51].

The perovskite crystal structure gets its name from a mineral $CaTiO_3$, originally discovered by Lev Perovski [52]. The crystal structure itself was first defined by Victor Goldschmidt as a part of his work on crystal tolerance factors [53]. The perovskite structure is of importance from the galactic scale to nanoscale, as the perovskite-structured materials are used for purposes ranging from distinguishing dwarf stars [54] to the electronics applications in photovoltaic cells, sensors [55] and lastly, the resistive switching devices studied in this dissertation. The simplest way to describe the perovskite structure is a compound of the form ABX_3, where the A and B are cations or molecules and the X is an anion which interacts with both A and B (Fig. 3). The B site can also be replaced with a mixture of cations, resulting into a double perovskite structure.

A more involved description of the ideal perovskite structure is a cubic unit cell which is made up of six X atoms (often oxygen) which occupy the face-centered sides of the face-centered cubic (FCC) structure, forming an octahedra around the B-site cations, while the A-sites reside at the corners of the unit cell (Fig. 3). In the general description of the structure, distortions of the structure are also considered, which are the source of many interesting phenomena mentioned earlier [56]. The main sources of distortion are tilting and deformation of the X octahedra. These transformations stem from the size mismatch of the sites and the Jahn-Teller effect, in which the energy of the system is minimized by undergoing a geometrical distortion [57]. The extent of the effect varies depending on the size and properties of the elements occupying the A, B and X sites. The structural deformation can also be caused by B-site spin arrangements, displacement of the B-sites or B-site vacancies [58].

The distortions of the perovskite structure cause the ideal cubic structure to turn into either tetragonal or orthorhombic configuration, or in the extreme cases (small lanthanides) result in loss of perovskite structure and formation of hexagonal structure. Work has been done to predict how the different elements affect the distortion in the resulting perovskite structure. One of the first (and simplest) empirical models is the Goldschmidt's tolerance factor, which indicates the degree of distortion in the perovskite structure and the compatibility of different ion pairs with the crystalline structure [53]. The formula for the factor is

$$t = \frac{r_A + r_O}{\sqrt{2}(r_B + r_O)},$$

where r_A is the radius of the A cation, r_B is the radius of the B cation and r_O is the radius of the anion, which most commonly is oxygen. The formula assumes a hard sphere approximation and the rigidity of the X octahedra and thus cannot be used to explain real materials accurately. However, the scenarios resulting from different factors are useful for qualitatively explaining the observed behavior in perovskite materials. Other more complex tolerance factors have also been proposed for predict the stability of the perovskite structure [59].

Utilizing the Goldschmidt's tolerance factor t, the perovskite structure can be approximately categorized into three possible tolerance factor configurations, accounting in that at the low and high values of t the perovskite structures do not manifest. At the high tolerance factor values above the limit for perovskite structure formation ($t \approx 1$), the system will generally be hexagonal or tetragonal, since either the A ion is too large or the B ion too small for the ideal cubic structure. As the t is lowered, there is a range where the size of A and B ions is ideal for minimum structural distortion, resulting in a cubic structure. The lower end of the compatible t range ($t \approx 0.8$) results into a rhombohedral or orthorhombic crystalline structure, as the A ions are too small to fit into the space between B ions [59; 60].

The general formula for mixed-valence manganites studied in this dissertation is

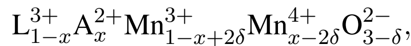

$$\mathrm{L}^{3+}_{1-x}\mathrm{A}^{2+}_{x}\mathrm{Mn}^{3+}_{1-x+2\delta}\mathrm{Mn}^{4+}_{x-2\delta}\mathrm{O}^{2-}_{3-\delta},$$

where L is a lanthanoid element, and A an alkaline earth element. The mixture between L and A elements is defined by the doping factor x, which varies in the range $0 \leq x \leq 1$. In the ABX_3 formalism L and A correspond to A, manganese to B and oxygen to X. In PCMO and GCMO, the A site of the ABX_3 has a praseodymium, gadolinium or calcium, the B site by manganese, and the X site is occupied by oxygen.

The element choices in both PCMO and GCMO cause considerable distortion of the perovskite structure. The comparatively small atomic radius of praseodymium and calcium ions distorts the perovskite structure of the PCMO over the whole

doping range and maximally at $x = 0.7$. Due to this, the electron bandwidth of PCMO is low and tunable by changing the doping x. The distortion effect in the GCMO is more pronounced due to the gadolinium's smaller atomic radius. Due to the distortion of the crystalline structure, the Jahn-Teller-splitting [57] is considerable [61] and both of the studied compounds have multiple possible magnetic orderings and related phenomena depending on the temperature and doping range.

1.4.1 $Pr_{1-x}Ca_xMnO_3$

Above $T \geq 280$ K $Pr_{1-x}Ca_xMnO_3$ has an orthorhombic Pnma space group, where the oxygen octahedra and Mn-O-Mn bonds have been turned from their undistorted cubic configuration. The degree of distortion varies over the calcium concentration x, which affects both electrical and magnetic properties, as well as the unit cell volume [62]. At the same temperature range, PCMO is a paramagnetic semiconductor with a gap varying from approximately 0.2 eV at calcium doping below $x \leq 0.4$ to values close to zero at $x \geq 0.5$. At higher doping, even metallic conduction is possible. The calcium doping also induces an n-type to p-type transition at $x = 0.3$ when the doping is increased above it [63; 62]. At the lower doping the distortion of the crystalline structure is considerable, which in turn disrupts many interesting phenomena, such as charge- and orbital ordering which begin manifesting at concentrations with $x \geq 0.4$ at lower temperatures. The charge ordering is a requisite for colossal magnetoresistance (CMR) and photoinduced colossal magnetoresistance [64; 65] which are also present in the PCMO, and could have interesting uses in both optical and memory devices [66; 62].

1.4.2 $Gd_{1-x}Ca_xMnO_3$

The calcium substitution x affects the magnetic properties of GCMO substantially, with marked differences between thin films [67] and bulk samples [68]. The bulk GCMO compounds are ferrimagnetic at the ground state, which can be caused partly by the polarization of the relatively large and oppositely directed magnetic moments of the Gd with respect to the Mn ions. The compounds also show complicated magnetic behavior below the magnetic ordering temperature (T_C or T_N). The Mn-ion ordering of the GCMO is ferromagnetic in the hole-doped region of $x \leq 0.5$. The charge ordering is also present in the middle doping of $0.5 \leq x \leq 0.7$ when the temperature is above T_N. In higher concentrations than $x = 0.7$, the ordering of the Mn ions is antiferromagnetic, most prominently at $x = 0.8$. Magnetic cluster glass phase of Mn-ions has been found in the electron-doped region of $0.8 \leq x \leq 0.9$. The resistive properties of the bulk GCMO are insulating for all concentrations of GCMO, except for $x = 0.9$ with almost metal-like degenerate semiconducting behavior. GCMO has also been found to

have colossal magnetoresistance (CMR) for fields exceeding 9 T for concentrations $0.8 \leq x \leq 0.9$, which is interesting, although the fields are higher than those needed in materials like PCMO [51]. The effect of photoexcitation in CMR of the GCMO still remains to be studied in detail.

1.4.3 Conduction mechanisms in oxide materials

Conduction models are used to describe the flow of electrical current through an oxide material. The four commonly discussed models are Ohmic conduction, space-charge limited conduction (SCLC), Poole-Frenkel (PF) conduction, and Schottky conduction, which are described briefly below, as they are of interest in the analysis of materials explored in this dissertation.

Ohmic conduction

In Ohmic conduction, current flow is proportional to the applied voltage, or in other words, the resistance of the material is constant. This is the simplest type of conduction and is often referred to as linear conduction [69].

Space-charge limited conduction

In space-charge limited conduction (SCLC), the current is limited by the space charge in the material. This type of conduction is often seen in semiconductors. A current flow which is quadratically proportional to the applied voltage is typical for the space-charge limited conduction [69].

Poole-Frenkel conduction

Poole-Frenkel conduction is a type of bulk conduction that occurs in insulators. In this type of conduction, the current is limited by the Poole-Frenkel effect, which describes trap-assisted electron transport in an electrical insulator under the influence of an electric field. The Poole-Frenkel effect occurs when applied electric field reduces the energy needed for electrons to enter the conduction band, as a result, the role of thermal fluctuations in electron transport is reduced [69].

Schottky conduction

Schottky conduction is a type of conduction which occurs in metal/semiconductor-interfaces. In this type of conduction, the current is limited by the Schottky effect, which describes a potential barrier formed at the junction between the metallic material and the semiconductor. The barrier height is defined by the difference of

the metal-vacuum work function and the semiconductor vacuum electron affinity [70]. For an n-type semiconductor the vacuum electron affinity has to be smaller than the metal-vacuum work function of the metal, and the other way around for an p-type semiconductor [69].

1.4.4 Resistive switching in mixed-valence manganites

There exists a lot of promising RS research on mixed-valence manganites. These compounds are versatile for RS applications, since as the doping level x of A cations changes, the compounds go through significant changes in the RS properties. Out of them, $Pr_{1-x}Ca_xMnO_3$ with $x = 0.3$ is one of the most commonly studied manganite compounds, which has been proven suitable for both memory and neuromorphic applications with crossbar arrays consisting of RS devices [21; 71; 72; 73; 74; 75],**[I]**. Other members of the mixed-valence manganite family, such as $La_{1-x}Ca_xMnO_3$ (LCMO) [76] and $La_{1-x}Sr_xMnO_3$ (LSMO) [77] share a similar RS mechanism [26], but have distinct RS characteristics which vary over the calcium substitution range. Manganite-based RS devices in general have been shown to possess small device-to-device variability [74], formingless operation **[I]**, well-controlled analog resistance states [78], all of which are beneficial in building both memory- and neuromorphic circuits [79].

The manganite-based RS devices consist of metal-oxide-metal structures, in which one of the metal-manganite interfaces acts as the active RS interface. The active interface is usually made from a reactive material, such as Al, Ti or TiN. The resistive switching in manganite-based devices obeys the general description for metal oxide based devices, where the switching is attributed to the electric field assisted migration of oxygen vacancies near the metal/oxide-interface [26], and the phenomenon tends to have similar characteristics between different manganites [26; 22; 80]. Due to the differences in the oxidation energies between the materials, the metal-manganite interface forms a rectifying oxide layer and depletes the structure of the perovskite manganite from oxygen in the region near the interface [81; 22].

The formation of AlO_x layer and oxygen-deficient perovskite region near the oxide layer has been observed in multiple manganite materials [25; 82; 83; 84; 85]. The modification of manganite bulk oxygen content is limited to the oxide/electrode interface due to the lower electric field inside the bulk in cases where the interface resistivity is substantially higher than the bulk resistivity.

1.5 Applications of resistive switching

Individual RS devices can be combined to create memory devices in many possible ways, one of them being the crossbar array. Crossbar arrays are structures with m

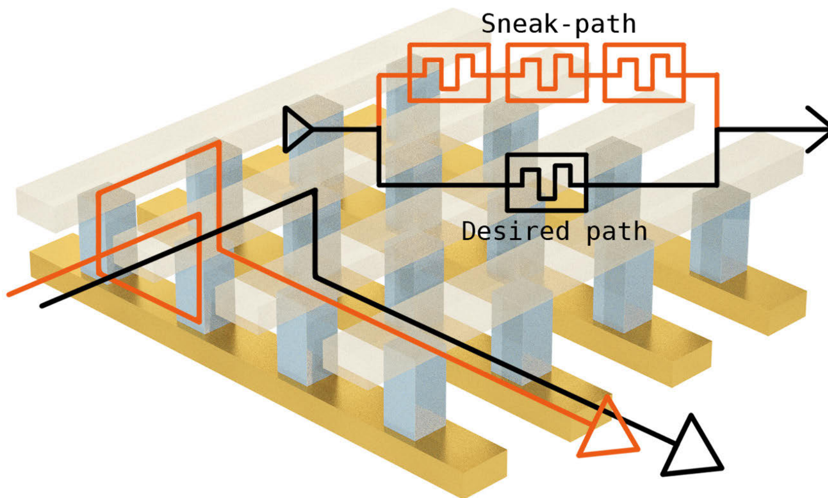

Figure 4. Crossbar array and the sneak-path problem. Sneak paths form when the current flow deviates from the intended path through low resistance state cells [32].

inputs and n outputs, which produce a 2D grid of $m \times n$ intersections (Fig. 4) [86]. These crossbar arrays can then be used to construct resistive random access memory (RRAM), which works by selecting rows and columns of the array and then sending a current through a selected RS cell, which modifies the state of the device. Some RS devices, including the ones studied in this dissertation can vary their resistance between a continuum of states. Due to this, the state density of the RRAM can be further increased by discerning multiple resistive states in each RS cell, as in the current transistor-based memory cells. Contrary to transistor devices, the RS devices often store the state non-volatilely, which is a clear advantage over the conventional charge-trap-based devices.

Despite the advantages, the crossbar array approach has problems which need to be addressed before it is ready for a widespread use. One of the largest issues is the sneak-path problem, where during the reading operation of one cell, the reading current passes through adjacent cells, resulting in misreads, especially when neighboring cells are in low resistance state (Fig. 4). Multiple solutions to the issue have been proposed, one of the most promising being complementary resistive switching (CRS), where two RS devices with differing threshold voltages are connected in series [87]. Other approaches include diode-based solutions where a simple to fabricate and low forward voltage drop Schottky-diode is built into each RS cell. These Schottky-diodes act as selectors, which prevent passing of current or modification of state below a threshold voltage [88]. The memristor can be added to a transistor device, forming a 1T1R device where one electrode of the memristor is connected to the drain of the transistor. The memristor can then be

accessed depending on the transistor state. However, this approach increases the circuit complexity and often requires separate manufacturing steps for the memristor and transistor manufacturing. Memristors are also inherently analog devices, and efficient integration to existing electronics requires additional circuitry in the form of efficient analog-to-digital and digital-to-analog converters and column decoders [89].

The oxide-based RS circuits have also been shown to be suitable for applications outside of memory devices. The advances in machine learning have created a need for more efficient hardware information processing using often biologically inspired approaches in a new field called neuromorphic computing [90]. Memristor arrays can be adapted well for this purpose [71] and provide a possible path to efficient hardware-based machine learning. Crossbar-based devices have been used to demonstrate RS in information processing applications, such as, matrix-vector multiplication [91] and convolution kernel operations [92; 93], leveraging the fact that the crossbar networks obey Kirchhoff's laws, and modifying the memristor weights enable $\mathcal{O}(1)$ computation of matrix products (multiply and accumulation, MAC). The above mentions enable the use of RS in use-cases like compute acceleration devices. Furthermore, many of these computation methods can function with high resistive state error tolerances [94], which counteract the downsides of many RS devices. There have also been promising results in mimicking the functionality of biological neurons and synapses [95; 96; 97; 19; 98; 99] with minimal amount of additional circuitry [100; 101; 102].

The RS devices have also found use in other domains. One of them being radiation resistant devices, which could be used in spacecrafts and aviation without the fear of radiation induced bit-flips, since the devices store the state in physical structure rather than in charge traps [103]. Other proposals include true random number generators [104]. Some RS devices, such as the ones studied in this dissertation can also function at low temperatures. However, despite the wide applications and promising results, more research is still needed to understand the physics behind the phenomenon, which will maximize the potential of these devices by enabling structured and rigorous engineering of the device characteristics.

2 Experimental details

2.1 Physical vapor deposition

Physical vapor deposition (PVD) is an umbrella term for vacuum deposition techniques in which can be used to create thin films, which can be used in various applications ranging from optical coatings to novel semiconductor devices. The PVD techniques are characterized by a process which begins with the material to be deposited in a condensed phase, after which it is turned into a vapor phase and then returned into a condensed phase at the target substrate. The memristor devices made during this dissertation work were all products of various PVD deposition processes.

2.1.1 Pulsed laser deposition

Pulsed laser deposition (PLD) is a method of depositing epitaxial thin films of material by using laser ablation. The setup consists of a vacuum chamber, a target material and a substrate on which the thin film made of the target material is deposited (Fig. 5). The deposition is done by focusing a high-power laser beam at the target pellet and firing it with short laser pulses in the timescale of nanoseconds. During the deposition the high energy fluence of each laser pulse causes evaporation of particles from the target material into a plasma plume. The surface of the substrate is positioned inside the space occupied by the plasma, and as a result, material from the plume gets deposited to it during each pulse. The shape and density of the plasma plume depends on the target material and the quality of the vacuum, and decreases in size as the partial pressure of the possible background gases increases.

In addition to the laser ablation, the steps before and after the deposition are equally important and should be done using a controlled procedure. These steps include the ramping up and ramping down of the temperature, and possible *in-situ* annealings. During the ramp-up, the substrate is heated to a controlled temperature before the deposition, which both enables and accelerates the chemical reactions happening at the surface of the substrate during the deposition. The thermal motion at a properly optimized temperature also helps the surface atoms to reach the state of minimum energy with higher probability, which in turn results in more

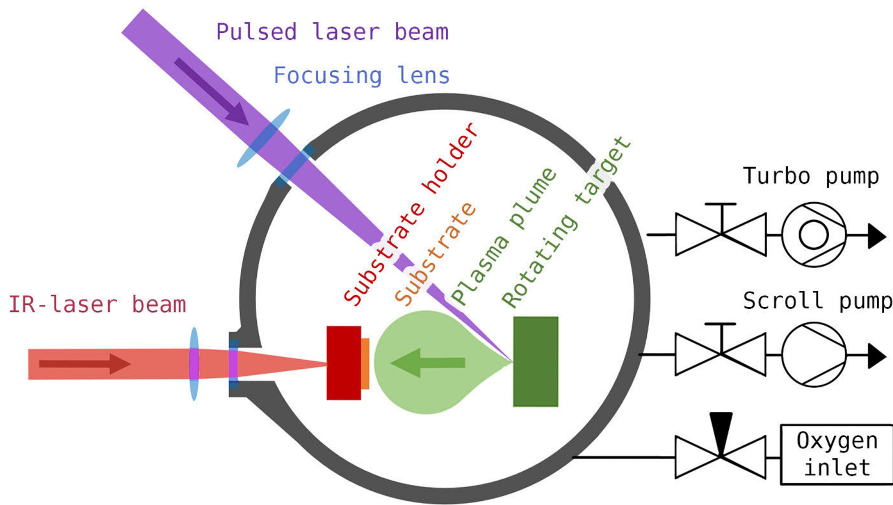

Figure 5. An illustration of a typical pulsed laser deposition system. The system is comprised of equipment for maintaining vacuum, heating the substrate and laser ablating the target pellet.

epitaxial crystalline structure. When making oxide thin films, oxygen is usually introduced into the vacuum chamber as a background gas in order to achieve a desired oxygen stoichiometry, which can be a requisite for effects like colossal magnetoresistance or superconductivity [51; 105].

The other parameters to consider are the positioning of the substrate with respect to the plasma plume and frequency, focusing and energy density of the pulsed laser beam. Optimizing the growth parameters is important, as incorrect deposition parameters can result in uneven layer growth, formation laser droplets which manifest as large particles on the surface of the deposited film or a complete absence of crystalline structure. Other factors affecting the film growth are the stoichiometry, grain size and preparation process of the target material. With the right operating parameters, the method allows deposition of smooth and epitaxial thin films with well-defined thicknesses and complex crystalline structures. However, due to the size of the plasma plume, the method is best suited for research purposes, where the area of the manufactured samples is small.

2.1.2 Magnetron sputter deposition

Magnetron sputtering is a thin film deposition technique which utilizes a spatially confined gaseous plasma in material deposition. In magnetron sputtering, the target material is consumed by a bombardment of high-energy ions originating from a plasma cloud, these collisions eject particles from the target material, which in turn travel through the vacuum onto a substrate material, forming a thin film on its

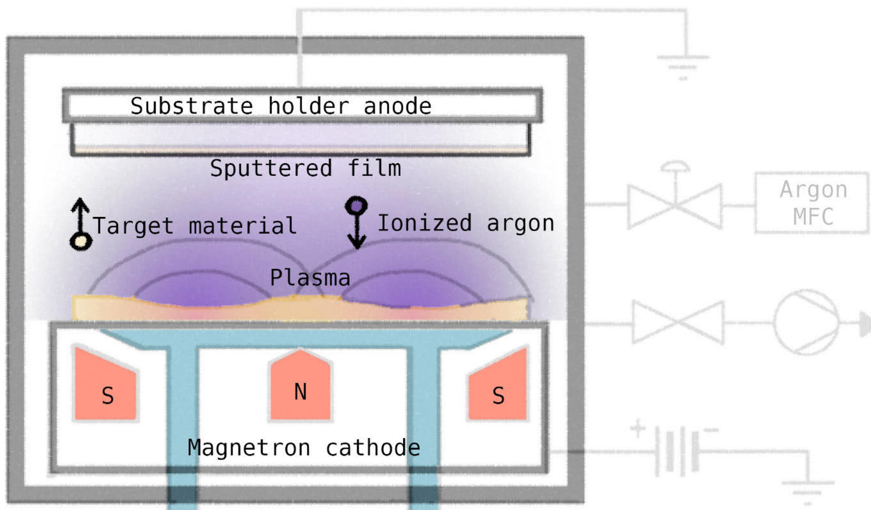

Figure 6. An illustration of a DC magnetron sputtering system used in this dissertation.

surface.

At the beginning of the process, a vacuum is pumped into a chamber, after which the chamber is flooded with a background gas and set to a regulated pressure. The gas is typically made of a high molecular weight gas, such as argon, in order to maximize the kinetic energy of the collisions. The gas is then ionized into plasma by applying a high voltage. The geometry of the used sputtering device has the cathode located behind the sputtering target and the anode is connected to the chamber grounding, which includes the substrate holder (Fig. 6). After the application of the field, the electrons in the gas are accelerated away from the cathode and collide with the nearby atoms. The collisions cause further ionization of the sputtering gas which, eventually turns into plasma. The positively charged ions of the plasma are accelerated towards the cathode, which results in high-energy collisions with the target material, causing ejection of material with high-enough kinetic energy to reach the substrate [106].

In magnetron sputtering, the electrons are confined near the surface of the sputter target material using strong magnets, which leads to increased density of the plasma and thus more collisions, which result in higher deposition rates. The magnetic confinement also prevents direct impact of electrons with the grown thin film, which is beneficial, since the electron bombardment could be detrimental for the fabricated thin film. The specific magnetron sputtering method used in this dissertation work was the direct current (DC) magnetron sputtering, which uses a constant current to accelerate electrons. This method can only be used with conductive target materials. Insulating materials become charged in a short duration of time, which diminishes the deposition rates. In order to alleviate this prob-

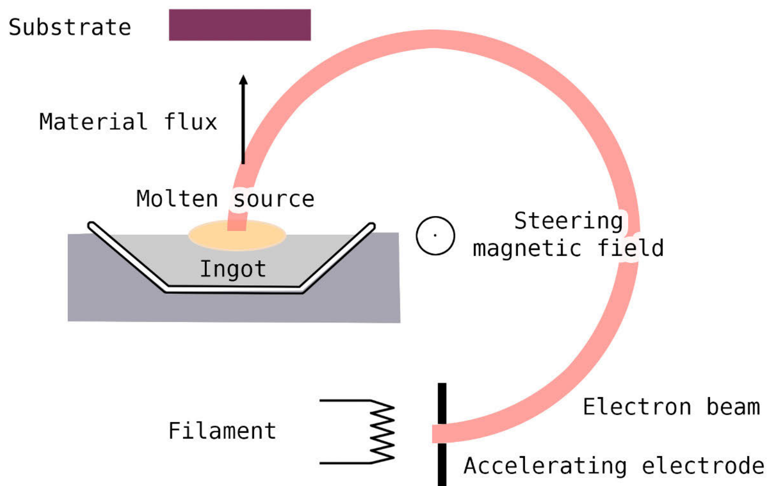

Figure 7. An illustration of an electron-beam physical vapor deposition process.

lem, an alternating electric field can be used to undo the charging effect (Radio Frequency sputtering, RF) [106].

Contrasting the PLD, magnetron sputtering can be used to deposit materials at low temperatures, and the requirements for deposited materials are less demanding due to the absence of high-energy laser ablation. The method can also be used to create thin films up to the 5 μm range due to the comparatively fast deposition rates, and the deposited area is technically limited only to the line of sight from the deposition target. However, the epitaxiality of the deposited films is often less than of those made with PLD, or the created films are completely amorphous. The sputtering might also remove elements from the target material at differing rates, resulting in stoichiometry differences between the target and the deposited film, and in case of vacuum contamination with air or gassing from the used substrate, the resulting films will be oxides instead of pure elements.

2.1.3 Electron-beam physical vapor deposition

Electron-beam physical vapor deposition (EBPVD) (Fig. 7) is a PVD method which works by bombarding the target material ingot with electrons in high vacuum, which causes the atoms in the target to eject in a gaseous phase. These atoms then deposit on all the surfaces of the vacuum chamber which are in the line of sight of the target. The electron bombardment is achieved by heating a tungsten filament, from which the ejected electrons are guided to the target ingot. The guiding is done by holding the ingot at a positive voltage, and a magnetic field is used to steer the electrons in an arc. The tungsten filament is kept out of sight of the

target in order to avoid chemical reactions with the target material. When the electrons hit the ingot, most of the kinetic energy is turned into heat, but some portion is lost to X-ray and secondary electron emission, and the method thus requires appropriate radiation shielding during the deposition. The heating effect of the bombardment either melts or sublimates the ingot material, causing material flux which is used in deposition. The method was used to deposit electrode materials on top of the manganite thin films during the dissertation work, both magnetron sputter deposition and EBPVD resulted in similar electrode properties.

2.2 Thin film characterization

2.2.1 X-ray diffraction

X-ray diffraction (XRD) is a structural characterization method which can determine atomic and structural properties of a crystalline material by taking advantage of the scattering of x-rays from a periodic lattice. In a periodic crystal lattice, the measured diffractogram forms sharp peaks at locations where the Bragg's law (1) is satisfied.

$$\lambda = 2d_{hkl}\sin\theta, \tag{1}$$

where d_{hkl} is the distance between the lattice layers, h, k, l are the Miller indices, λ is the wavelength and θ the angle between the incident rays and the surface of the lattice. The oxide thin films measured in this dissertation work were all of either cubic, tetragonal or orthorhombic structure, in which the spacing between the lattice layers obeys the equation:

$$\frac{1}{d_{hkl}^2} = \frac{h^2}{a^2} + \frac{k^2}{b^2} + \frac{l^2}{c^2}, \tag{2}$$

where a, b, c are the lattice parameters. When the indices and locations of the peaks of the epitaxial thin film and the substrate are known, the precise values of the peaks from the known substrate material ($SrTiO_3$ with a diagonal cubic cell dimension of 5.52 Å) can be used to correct the zero point of the diffraction measurements of the grown material. After the correction, the indexed peaks can be used to calculate the lattice parameters a, b, c along with the broadness of the diffraction peaks, which can be used to estimate the quality of the films in terms of epitaxiality and crystalline strain.

The X-ray measurements were made using a Bragg-Brentano-geometry diffractometer (Panalytical Empyrean) (Fig. 8). Copper was used as the anode material, which has a K_{α}- in the range of the wavelength of the measured samples' lattice parameters (1.54 Å). The measured characteristic radiation of copper was monochromatized by filtering out the K_{β}-peak using commercial Bragg-

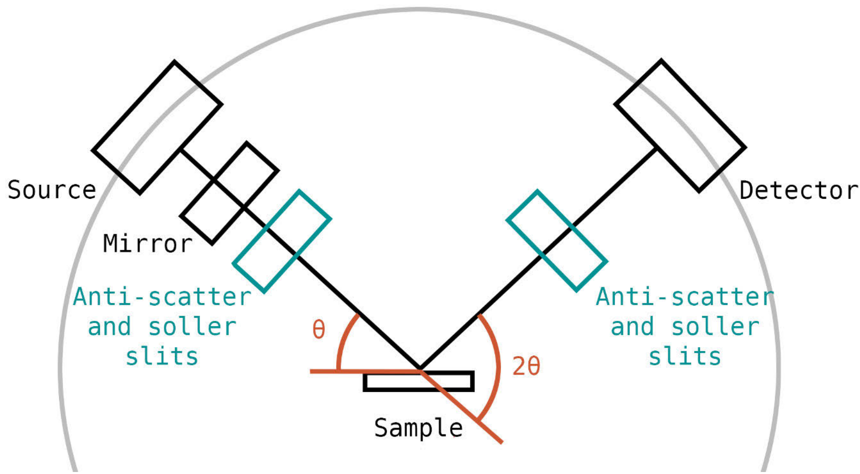

Figure 8. An illustration of an X-ray diffractometer with Bragg-Brentano-geometry.

BrentanoHD mirror optics from Malvern Panalytical on the incident side. On the incident side Soller slits of 0.04 rad (0.02 rad in XRR measurements) and 1/4 degree antiscatter slits were used to limit the spread and scattering of the incident beam. The diffracted side had 0.04 rad Soller 7.5 mm anti-scatter slit and Pixcel 3D two dimensional detector. The measurements were made using a 5-axis goniometer which allowed maneuvering the sample in all three axes using angles ϕ, χ and ω.

X-ray reflectivity

X-ray reflectivity (XRR) is a technique which can be used to determine the thickness, mass density, and roughness of single and multilayer stacks of thin films. The analysis can be made on both amorphous and crystalline materials. When X-rays hit the surface of the material at grazing angles of incidence, total reflection will occur at or below a critical angle, θ_c, which depends on the electronic density of the material:

$$\theta_c = \arcsin(1/n_r), \quad \theta_c = \lambda\sqrt{\rho/\pi},$$

where n_r and λ are the refractive index and wavelength of the X-rays and ρ the electron density of the material. Above the critical angle X-rays begin to penetrate the material and the reflectivity is rapidly lost.

The roughness of the surface causes decrease in the reflectivity, and if the thin film on top of the surface has a differing electronic density compared to the substrate material, the reflected X-rays from the interface between the thin film

and the substrate and from the surface of the thin film will interfere with each other either constructively or destructively. This interference causes an oscillation pattern to appear in the detected intensity as a function of grazing angle [107; 108].

The electron density of the material can be deduced from the measured intensity pattern, since the intensity of X-rays scattered by the sample is proportional to the square of the modulus of the Fourier transform of the electron density. As a result, the layer thicknesses and roughnesses of the characterized materials can be determined from the recorded pattern [108]. The film thickness can also be determined from the oscillation period in the measured intensity pattern amplitude over the grazing angle from angles above the critical angle θ_c, which was used in this dissertation to verify the thin film consistency of memristor devices.

2.2.2 Energy-dispersive X-ray spectroscopy

Energy-dispersive X-ray spectroscopy (EDS) is a method which was utilized to verify the calcium doping concentrations of the fabricated oxide thin films. In brief, the method works by focusing a beam of electrons to the studied sample. The electronic configuration of the atoms in the vicinity of the sample surface is initially at the ground state. The electron beam excites electrons of the inner shells of the atom, which causes formation of electron holes. These electron holes are then filled by electrons from the higher-energy shells. The energy difference may then be released as X-ray emission. A detector is then used to measure both the count and the energy of the emitted photons. The elemental composition of the sample can then be inferred from the measured energy spectrum, since the energy differences between shells are characteristic to the atomic composition of the measured material.

2.3 Device patterning and preparation

The fabrication of the resistive switching devices used in this dissertation requires patterning of thin films and electrode materials. Stencil lithography and photolithography were tested to pattern the devices, and stencil lithography was chosen as the used patterning method for the samples discussed in this work.

Stencil lithography is a method where a stencil (shadow mask) is placed above the substrate on which material will be deposited. The stencil blocks parts of the substrate during the deposition, and is removed after the deposition is complete. The resulting pattern of material is the inverse pattern of the stencil mask. The method is quite robust, and can be used to pattern a wide variety of materials without the need for chemical treatment, unlike resist-based photolithography methods. However, the pattern precision is limited by the tooling of the stencil mask, which in practice means simple and connected shapes at micrometer-scale

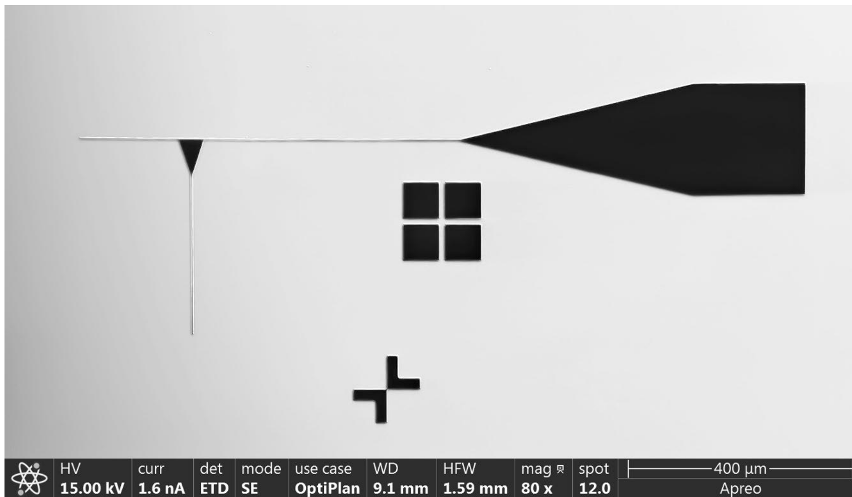

Figure 9. Photolithography patterned GCMO thin film, which can be overlaid with another key-patterned material to produce devices with relatively small interface areas.

feature resolution. The method also suffers from the shadowing effect caused by the gap distance between the mask and the substrate, which blurs the edges of the pattern. In addition to deposition, stencil lithography is equally suitable for removing material exposed through the mask by sputter bombardment.

Other patterning method tested in this work was photolithography (Fig. 9). Photolithography improves on stencil lithography by decreasing the pattern size. In the used positive resist photolithography a photosresist layer is prepared on the substrate by spin coater and the resist is hardened by heating, after which a mask is placed on the substrate to block off areas of the resist. Parts of the resist are then exposed to ultraviolet light, which makes the exposed parts more soluble to the photoresist developer. After the exposure, the resist is developed with a developer which depends on the photoresist polymer (in our case a NaOH-solution of 0.15 mol/dm^3). The developer removes the photoresist from the unmasked areas along with the base material, in case it is soluble as well. In this work the remaining photoresist material was used as a sacrificial layer in a separate sputter material removal step. The pattern features obtained from photolithography are sharper than those obtained by stencil lithography, as the theoretical resolution limitations are reduced to the optical diffraction limit and the result quality of the chemical etching process.

2.4 Data acquisition

The data acquisition was an important part of the work done in this dissertation. The measured materials have electrical hysteresis and fast switching in resistivity

measured in orders of magnitudes and their properties are highly dependent on multiple paramaters related to timings, electric field and temperature. There are no established software tools for memristor data acquisition, and thus the software to prepare the measurement devices for the measurements, execute the measurement sequences, analyze the results and plot them was written from the ground up, excluding the measuring of spike-timing-dependent plasticity.

The electrical characteristics of the memristor devices were measured using a Keithley 2614b source-measure unit (SMU). The used sourcemeter can source and measure both current and voltage with two channels which can function independently. The temperature controlled studies were done using the Keithley 2614b connected to the sample chamber of a physical property measurement system (PPMS) made by Quantum Design. The spike-timing-dependent plasticity (STDP) measurements were recorded using an ArcOne memristor characterization platform. The platform can measure the device state and supply short voltage pulses with greater timing control than the 2614b at resistances below 10^6 Ω. The used measurement devices were interfaced using the VISA-protocol and controlled via programs written in Python, LabVIEW and Lua.

The control flow of the sweep measurements ran on the Keithley 2614b with an embedded Lua-interpreter, this was done in order to achieve full control of the timings and sweep shapes. The device collected the datapoints into a buffer, which was periodically sent back to the measurement computer. The sweep functionality was achieved by constructing a list of desired voltage steps on the measurement computer, then sending the list to the device and using the list in combination with the hardware timers of the Keithley 2614b to enact the sweep. The timings were adjusted to take into account the worst-case rise-times of the source and appropriate integration times for all measurement and sourcing ranges.

2.4.1 Measurement sequences

Various different measurement sequences were used depending on the device properties under investigation. The main characterization was done using $I(V)$-sweep measurements, the pulse width and amplitude optimization measurements were used to determine optimal sweep measurement parameters, endurance measurements verified that the devices stay stable and withstand prolonged use, temperature measurements captured device characteristics for in-depth conduction model analysis and the spike-timing-dependent plasticity (STDP) measurements demonstrated that the devices can be used in novel neuromorphic computation approaches.

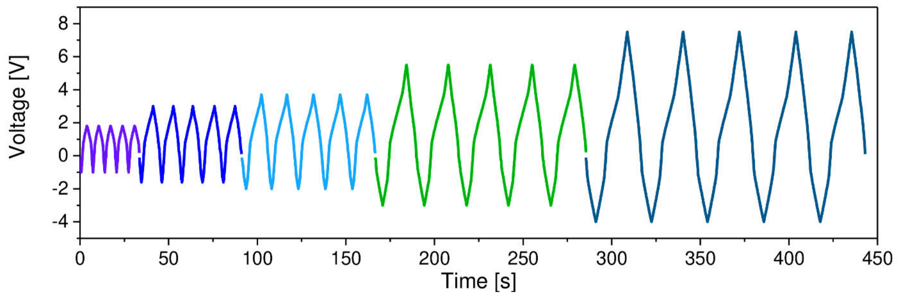

Figure 10. Pulse amplitudes used in sweep measurements, a read pulse of fixed amplitude was applied after each voltage pulse. The figure shows 5 measurements of differing voltage amplitudes, each of them composed of 3 repeated loops.

Sweep measurements for device characterization

The $I(V)$-sweeps for memristor devices were measured by sweeping the voltage in a sequence of steps $0 \rightarrow V_{max} \rightarrow -V_{min} \rightarrow 0$ with logarithmic amplitude progression, 100 ms step width and a 100 ms low-voltage read between each step (Fig. 10). Datapoints were measured during and after the writing pulse. The during-pulse datapoints were used in presented $I(V)$-curves and the after-pulse datapoints in remnant resistance calculations, which were also used when determining switching ratios. The measurements on thin film resistivity used 4-point probes method in order to remove the contribution from electrode interfaces and wiring.

The characterization of each device began by measuring the $I(V)$-behavior with two different approaches, at first by applying measurement sweeps with increasing voltage amplitudes till the device broke, and then using the limit parameters obtained from a broken device as the initial parameters for another device, where the amplitude was decreased till the switching was not present. The results were compared and the voltage amplitude was chosen from the region between best switching properties from both approaches. Once voltage amplitudes with maximal switching ratio and good repeatability were found, the results were noted and a new device with optimized parameters was used in final measurements which were used in analysis.

Pulse width and amplitude optimization measurements

The pulse width used in sweep measurements was optimized by measuring the change in device resistance in the linear region over many different pulse widths and voltage amplitudes. Between each pulse width and voltage amplitude combination the device was set into a stable HRS or LRS base resistance level with a fixed pulse. The sequence consisted of beginning from low voltage, doing 3 pulse

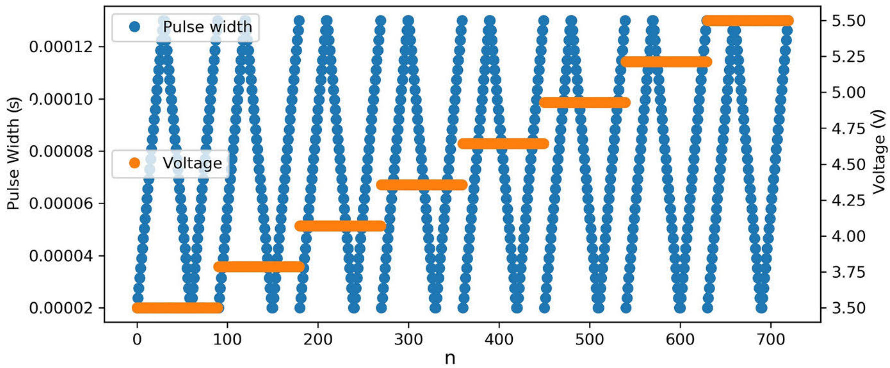

Figure 11. A measurement sequence used for optimizing pulse width and voltage amplitude.

width sweeps for repeatability and then moving to the next voltage level (Fig. 11). The pulse widths include a small constant delay from the measurement device, which causes a short delay for the pulse to initiate.

Device endurance measurements

The device endurance was measured by first verifying the repeatable switching in the device with optimal voltage amplitudes, after which the device was subjected to the repeated measurement sequence described below. First, the device state was read from the linear voltage amplitude region, then a fixed width and amplitude pulse was applied to the device to induce it into the HRS, the device state was read again at linear region and finally the device was put to LRS with a fixed LRS pulse. The described sequence was repeated for a prolonged time, and results were collected for analysis of the switching stability. The data was collected after each pulse (current-aware measurement) as opposed to current-blind measurements, where the device state is collected only during some set number of cycles, as is recommended by the best practices for RS device measurements [24]. This allowed us to verify that the switch between resistive states never failed to happen.

Device preparation for temperature measurements

The temperature measurements concentrated on measuring the positive polarity HRS $I(V)$-behavior across a wide range of temperatures T and different calcium concentrations x. The goal was to prepare the devices into as homogeneous and repeatable state as possible. Thus, the switching in each device was first stabilized by cycling them with above described voltage sweep cycles with optimal voltage amplitudes until the switching was stable at room temperature, 3 sweeps

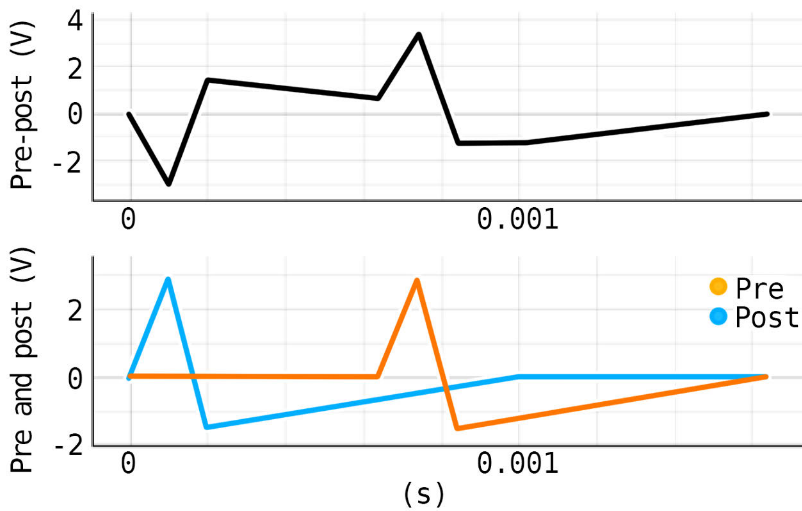

Figure 12. Waveforms used for post- and presynaptic pulses and their resulting waveform.

were determined to be enough. After the switching was confirmed to be stable and repeatable, the device was put to HRS and the temperature was raised to 350 K. Following that, the positive voltage amplitude polarity HRS quadrant was measured for each temperature step using dense measurement points and long integration times in order to minimize noise and allow adequate fitting at low voltage amplitudes.

STDP measurements

The device was connected to the ArcOne memristor characterization platform, which allowed input of pulses of precise timing and amplitude. The measurement program took in the pre- and postsynaptic pulse waveform shapes and simulated the resulting superposition of the two waveforms with varying time difference between the beginning of the pulses (Fig. 12). Each resulting waveform corresponding to different delay between the pulses was then fed into the device, and the change from base conductance was recorded, in-between the waveforms the device was set back the the base resistance state. The result of the measurements was the characteristic STDP shape, which is discussed further in section 5.3.

3 Thin film properties

The materials investigated in this dissertation were $Gd_{1-x}Ca_xMnO_3$ over the calcium doping range $0 \leq x \leq 1$ and $Pr_{1-x}Ca_xMnO_3$ at a single concentration of $x = 0.4$, both of which have RS properties which depend on the used thin film fabrication method, calcium concentration and used electrode materials [109]. During the dissertation work, the PCMO was used as a reference material in order to determine optimal characterization methods and to provide a reference for GCMO memristors. Later on the knowledge gained from the PCMO devices was used to study the effects of calcium concentration x in the RS and conduction properties of GCMO.

3.1 Memristor fabrication process

In order to create functioning RS devices, the thin films need to be of high quality, and the fabrication process has to be repeatable. Thus, the steps to create the devices are outlined below. Both PCMO and GCMO used the same base fabrication method with differing parameters. The thin films were deposited on 5 x 5 x 0.5 mm^3 (100) $SrTiO_3$ (Crystal GmbH) substrates by pulsed laser deposition (PLD) using λ = 308 nm XeCl-laser. The pulse duration was 25 ns, the pulse repetition rate 5 Hz and the pressure of flowing oxygen in the chamber 0.175 torr. The laser fluence was 2 J/cm^2 for GCMO films and 1.3 J/cm^2 for PCMO films. The film growth temperature was 700 °C for GCMO and 500 °C for PCMO, with *in situ* post-annealing treatment of 10 minutes in an atmospheric oxygen pressure. The PCMO films were deposited from a target with $x = 0.4$ and the GCMO films were made from targets spanning the whole calcium doping range in increments of 0.1, and for concentrations $x = 0.85$ and $x = 0.95$ [68]. The GCMO thin films used in the initial characterization steps were made using a constant pulse count of 1500 pulses. The final films used in RS measurements used calibrated pulse counts to reach the thickness of 100 nm for each calcium concentration. Both film manufacturing methods result in devices with same RS characteristics. More details on the PLD fabrication and target material creation process for GCMO can be found in [110; 67] and for PCMO in [111].

The active and passive interfaces of the memristor devices were patterned metal electrodes. The electrode fabrication process consisted of depositing 0.5

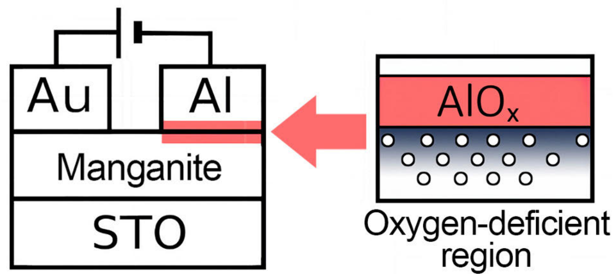

Figure 13. The planar device geometry.

mm diameter metal electrodes on top of the manganite thin film. The electrodes were deposited using either room temperature Ar-ion DC magnetron sputtering or EBPVD, both of which yielded devices with similar RS properties. The thickness of the electrodes was 100 nm, which was determined from calibrated deposition times. The accuracy of calibration was verified with X-ray reflectometry (XRR). The pattern thickness and edge shape were also tested using atomic force microscopy (AFM) and scanning electron microscopy (SEM). The separation distance between the electrodes was approximately 200 μm. The wiring from measurement device to memristor devices was made by connecting the sample casing to the electrodes with a wedge bonder (TBT, model HB05) with a 40 μm thick aluminum wire. The interface between electrode and wire was tested to be Ohmic for each electrode material used. The wiring from sample holder to the measurement device was made using a grounded coaxial cable of short length in order to minimize external electromagnetic interference.

The end results of the fabrication process were memristor devices of planar geometry (Fig. 13), which were determined to be consistently reproducible. In addition to the planar geometry devices used in the measurements, work was also carried out on designing a path for miniaturization of the devices by photolithography-based patterning and capacitor geometry, of which the incomplete results are presented. The alternative patterning method involved Ar-ion sputtering of GCMO thin films with a pattern of developed photolithography resist on them. Since the thickness of the photoresist layer (in the order of microns) greatly exceeds the thickness of the GCMO films (100 nm), the GCMO thin film was consumed first. This resulted in patterned films with photoresist layer on them. The photoresist was then dissolved, resulting in patterned GCMO thin films with minimum stripe width of 2 μm (Fig. 9). The devices based on this method were not used in the main body of the research due to the obstacles encountered in multilayer deposition and pattern alignment. However, a similar method could be used as a possible starting point in adapting the fabrication process used in this dissertation to produce smaller devices for future research.

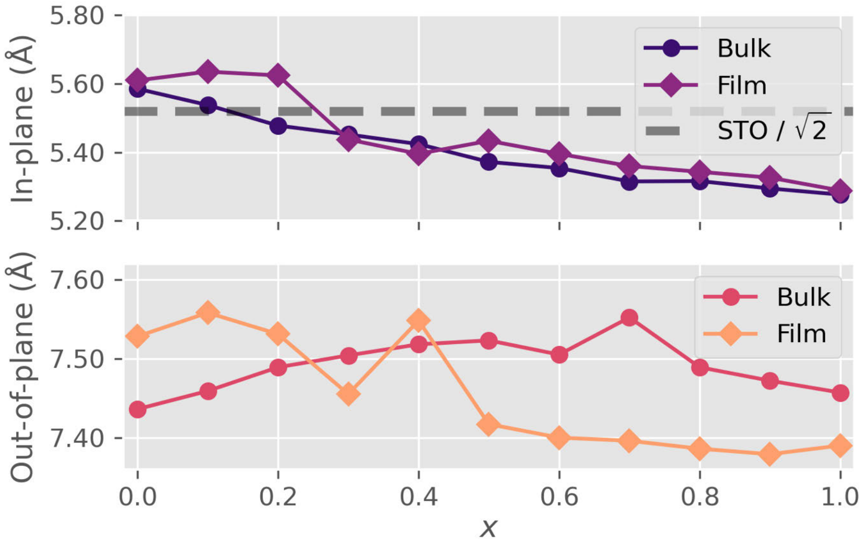

Figure 14. Lattice parameters of manufactured GCMO thin films over the calcium substitution range.

3.2 Assessing device quality

The combination of measurement methods discussed in the previous section provides an effective way of inspecting the surface morphology, crystalline structure, chemical composition and electrical properties of the fabricated devices. Before the main measurements of the dissertation, the grown GCMO and PCMO thin films were verified to be well-crystallized and epitaxially textured by X-ray diffraction (XRD). The elemental composition and calcium content of the GCMO samples was verified with energy-dispersive X-ray spectroscopy (EDS). The EDS measurements agree with the nominal calcium content of the films with no systematic deviation **[II]**, and the calcium content can be distinguished between steps of 5 %. The reproducibility of the RS was confirmed by testing multiple thin film devices made on separate substrates. The characteristics were found to be consistently similar.

The results of the XRD analysis for GCMO thin films grown on the STO (100) substrate are shown in the Fig. 14. The lattice parameters over the calcium doping range were determined from $\theta - 2\theta$-scans from different directions. The $(00l)$ was used to get the out-of-plane b and $(0kk)$ and $(hh2h)$ for the in-plane lattice parameters a and c. The lattice parameters a and c are referred as a singular in-plane lattice parameter as they cannot be distinquished in the made thin film measurements. The a and c directions match the diagonal dimension of the lattice parameter of the STO substrate (5.52 Å) (Fig. 14), which is expected, since the perovskite structure of the GCMO grows rotated 45° with respect to the STO

substrate, which minimizes the lattice mismatch. The lattice constants were found to follow their bulk counterparts over the whole calcium range [110]. $2\theta - \phi$ scans of (224) peaks were also measured, and they showed that the films were fully textured. More details on the XRD analysis of GCMO can be found in [110; 67],**[II]**. The lattice parameters of the PCMO $x = 0.4$ samples were measured to be a = 5.4354 Å, b = 7.6511 Å and c = 5.4277 Å. An extensive XRD analysis of the PCMO thin films can be found in [111],**[I]**.

3.3 Phase diagram of the GCMO

The initial work on the GCMO in this dissertation was begun by supplementing the previously measured magnetic phase diagram of GCMO thin films [67; 68] with electrical transport measurements and studies on the conduction mechanism. The results were combined into a full phase diagram of the GCMO (Fig. 15) **[II]**. The thin film samples of GCMO were found to differ from the bulk in both magnetic and transport properties.

At the hole doped region ($0.1 \leq x < 0.4$) the high temperature state was a paramagnetic insulator, and a ferrimagnetic insulator in the low temperature range. Compared to the base compound $GdMnO_3$, even a small amount of calcium doping was enough to change the compound from antiferromagnetic state into a ferrimagnetic state. A metamagnetic transition, where external field changes the magnetic state from antiferromagnetic to ferromagnetic was also observed by measuring the transition from magnetic hysteresis loops (magnetization versus external magnetic field) of the films in the hole doped region ($0.1 \leq x \leq 0.3$) at temperatures below 100 K. At the middle doping region ($0.4 \leq x \leq 0.7$) and low temperatures the films behave like soft ferromagnets. At higher temperatures the material is in a charge-ordered state, with the ordering temperature close to room temperature. The high doping region from $0.8 \leq x \leq 1.0$ is more involved and differs from the widely studied $CaMnO_3$. The behavior at low temperatures is an antiferromagnetic insulator for $x = 0.8$ and 1.0, measured by observing an antiferromagnetic transition in the zero field cooled (ZFC) curves, while the $x = 0.9$ has a hysteresis loop of a soft ferromagnet. At higher temperatures the material is in a conductive paramagnetic phase. The $x = 0.9$ also has a distinct minimum in the resistivity versus temperature curves (Fig. 16). The low temperature behavior of $x = 0.9$ also has irreversible thermal hysteresis. This first order phase transition could be attributed to a change from a glassy kinetically arrested metallic ferromagnetic phase to a stable antiferromagnetic insulator phase **[II,V]**.

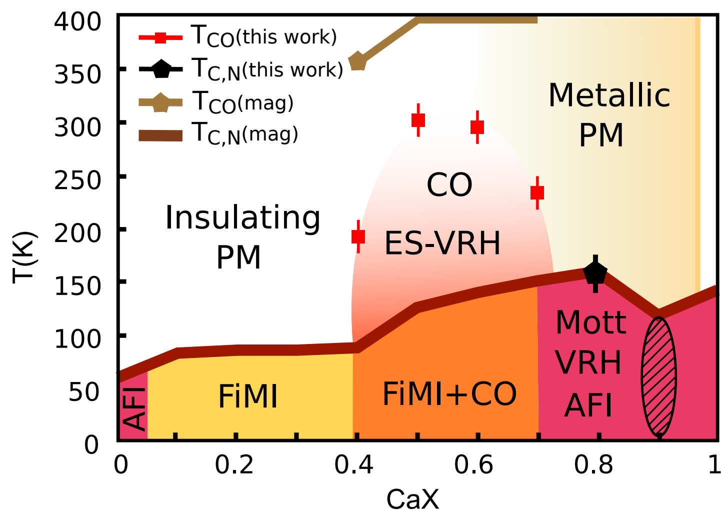

Figure 15. The magnetic phase diagram of GCMO. Figure from **[II]**.

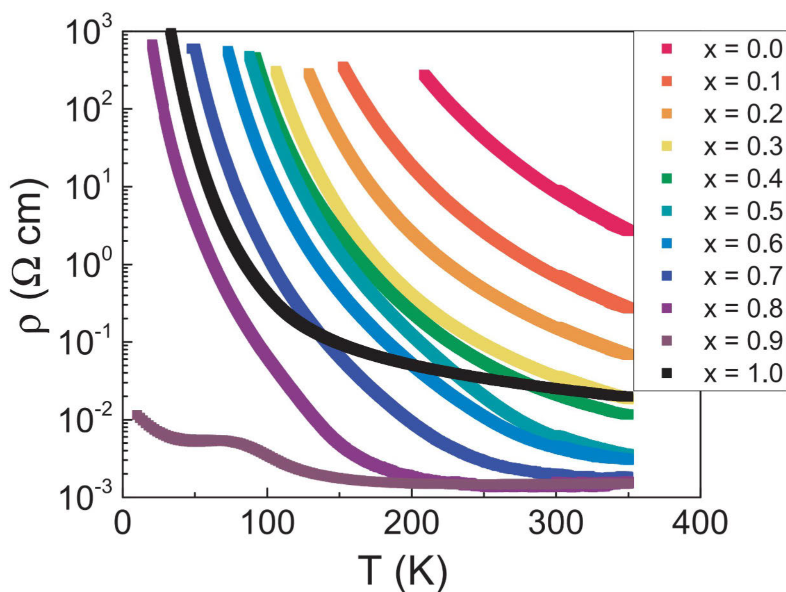

Figure 16. Four point probe measurements of GCMO thin films. Figure from **[II]**.

4 Resistive switching properties

As a preliminary work before the main measurements of the dissertation, several interface materials were tested for RS properties with the PCMO. Work function difference between the active oxide material and the electrode metal can be used as a reasonable predictor of the degree of rectification of the RS interface, although other factors, such as the surface chemistry of the materials, can also have a considerable effect on the final interface. The work function of a p-type $Pr_{0.6}Ca_{0.4}MnO_3$ is approximately similar to the values reported for other concentrations: $\phi \approx 4.9$ eV [112] for x = 0.3 and $\phi \approx 4.8$ eV for x = 0.5 [25], although measurement setup affects the obtained work function considerably. For PCMO/metal-interfaces a more rectifying interface is expected for the Al (ϕ = 4.06 - 4.26 eV [113]) and Ti (ϕ = 4.33 eV [113]) than for the Ag (ϕ = 4.26 - 4.74 eV [113]) or Au (ϕ = 5.10 - 5.47 eV [113]). The measurements also agree with the reasoning, and the noble metals silver and gold formed an Ohmic interface with PCMO $x = 0.4$, while metals like aluminum and titanium form a highly rectifying interface. Out of the electrode materials tested on PCMO (Cu, Ti, Al, Ag, Au, In), Al was the most rectifying.

The final devices used in measurements were designed to have only one active interface by choice, since single active interface localizes the phenomenon to one region, which is realistic for applications and simplifies the characterization. The chosen electrode materials were aluminum as the reactive interface and either gold or silver as the passive interface. Interfaces made from gold and silver do not contribute to the switching and form an Ohmic interface with both GCMO (Fig. 17 a) and PCMO (Fig. 17 b). The linearity of the passive interfaces with GCMO and PCMO was confirmed by fabricating devices with only passive interfaces (Au/oxide/Au, Ag/oxide/Ag, Au/oxide/Ag). These interface combinations were then confirmed to have no switching and negligible resistance contributions. The aluminum interface was chosen since it was the most reactive out of the tested materials.

Before the RS measurements are discussed, it is worthwhile to study the possible conduction paths in memristor devices with planar geometry (Fig. 13), which were used in the main body of the dissertation work. The planar configuration consists of a thin film deposited on a substrate, and electrodes with fixed separation distance and thickness on top of the film. In the devices used, the separation

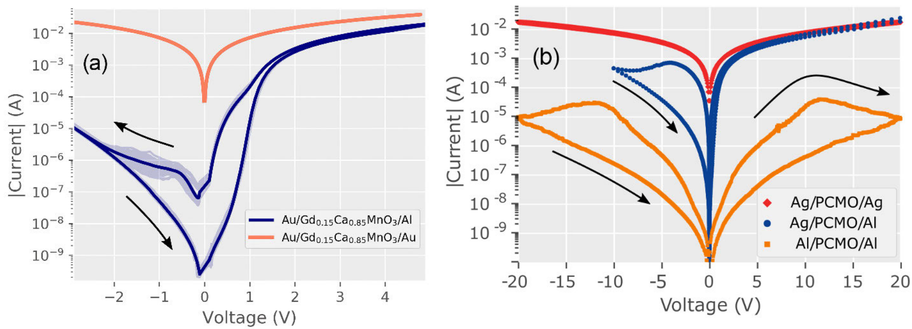

Figure 17. I(V)-loops for GCMO $x = 0.85$ (a) and PCMO $x = 0.4$ (b). The I(V)-curve of the Al/PCMO/Al shows symmetric table-with-legs behavior [26]. Figures from **[I,III]**.

distance was 200 μm and the oxide film thickness 100 nm. There exist multiple possible regions which can contribute to the overall conductive properties of planar devices. One of the possible conduction paths is the current flow through the interface between the oxide material and the substrate (STO) which exists in planar device geometry. However, it can be concluded that the contribution is linear and insignificant compared to the Al/oxide-interface, as the non-linear conduction happens only when an Al-interface is present (Fig. 17).

The linearity of the noble metal interfaces can also be seen from the constant logarithmic derivative with a value of one (Fig. 25), corresponding to the Ohmic conduction, which is discussed in more detail in section 5.1. Due to the observed linearity, even if the current flow happens through the substrate/manganite-interface, the contribution is linear and insignificant compared to the Al-interface contribution. Additionally, the measured resistance of a bare STO (100) substrate over the 200 μm distance is over 10^5 Ω, which is more than the resistance measured from the GCMO and PCMO samples with Ohmic Au-interfaces (Fig. 18) or with four-point probe measurements (Fig. 16). The manufactured devices also had no noticeable variation in switching behavior when the electrode separation distance was varied, indicating that the dominant switching effect is not caused by filamentary conduction paths inside the bulk of the manganite material. Together these observations imply that the RS-effect is confined to the vicinity of the Al-interface and is not based on metal ion movement in the case of Ag-electrodes. Another hint to oxygen vacancy based valence-change switching at the electrode interfaces is the presence of ”table-with-legs” profile on Al/PCMO/Al-devices (Fig. 17), which has been previously obtained by simulating dielectric with a changing oxygen vacancy profile between two electrodes [26].

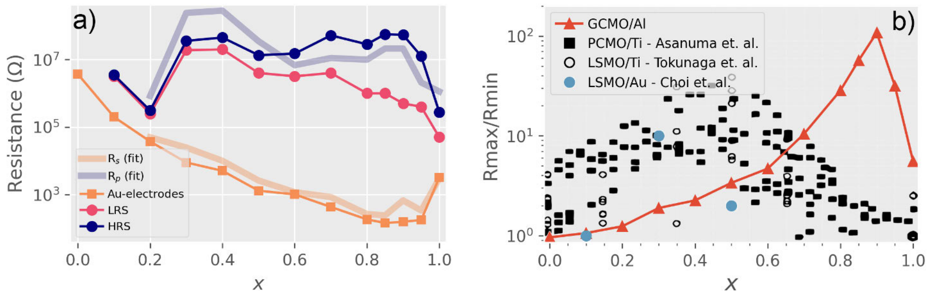

Figure 18. Resistances of GCMO with Ohmic Au-electrodes and Al-interfaces (HRS and LRS) over the calcium substitution range x at room temperature. R_s and R_p show results from the conduction model fit, R_s coincides with the Ohmic interface and R_p with the HRS. b) Comparison of the switching ratio over x for Al/GCMO, Ti/PCMO [25], Ti/LSMO [43] and Au/LSMO [44]. Figure from **[III]**.

4.1 Characterization of resistive switching

A typical example of a stable switching for GCMO is shown in Fig. 17 a) and for PCMO in Fig. 17 b). The switching in the devices is bipolar, where the high and low resistive states can be achieved by the application of opposite voltage polarities, similar to what has been reported for other manganite compounds [22; 114; 72; 25; 26; 27; 29; 30]. The negative polarity induces the transition to HRS and positive to LRS. The voltage amplitudes for RS are asymmetric, and the transition to the negative polarity induced HRS happens at a lower amplitude than the positive polarity induced LRS transition. Unless otherwise stated, the shown sweep measurements related to electrical properties of GCMO are averages of 50 stable sweeps, and multiple devices on separate substrates were used to confirm similar switching properties. The HRS and LRS voltages were chosen to obtain a reasonable compromise between a high switching ratio and device reliability.

The resistance of a pristine GCMO and PCMO devices is initially between the HRS and LRS resistances and does not require electroforming (introduction of temporary high current in order to introduce the presence of RS), although the first loops do show irregular step changes. Similar forming-free behavior has been observed for both bipolar and unipolar switching in other PCMO studies and has been found to be affected by both electrode materials and the growth conditions [115; 109]. As the switching in the devices does not require a high-field forming step or current limitation, the device homogeneity is good, and the devices show predictable behavior with similar HRS and LRS resistance values across samples. No switching is observed when the applied voltage is below a threshold, which for the PCMO $x = 0.4$ devices on both polarities is V_{th} = 3 V, and for the GCMO between 1 V $\leq V_{th} \leq$ 6 V on positive polarity depending on the calcium doping x. Using the region below this threshold during measurements is important, as it

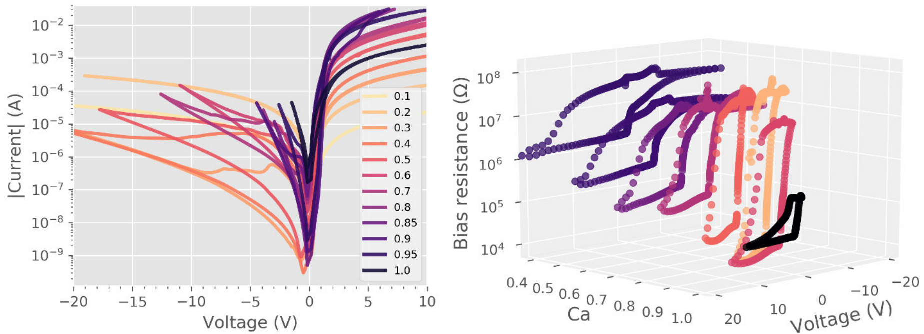

Figure 19. The $I(V)$ loops and linear-region resistance loop measurements for each calcium substitution level of GCMO. Required switching voltages decrease at higher x and the switching becomes more asymmetric. Figure from **[III]**.

enables non-destructive reading of the resistive state. As such, the low voltage read was set to -200 mV for PCMO and 450 mV for all calcium dopings of GCMO. The read polarity and amplitude differ for the two materials because the used non-switching linear region was optimized for higher read current in GCMO, which reduces noise and required integration time in measurements.

4.2 Effect of calcium composition

The doping effect on the manganite layer was one of the main interests of this dissertation. To study the effect, $I(V)$-loops of the GCMO/Al-interface as a function of calcium substitution level x are shown in the Fig. 19 and the corresponding switching ratios in the Fig. 18 b. The switching ratio is defined as the ratio of stable minimum and maximum resistances measured at the read voltage (450 mV), which is in the linear region and below the switching threshold for all concentrations. The calcium substitution x greatly affects the RS properties of the GCMO (Figs. 18 and 19). The resistivity of the Au-interface is lower at higher x, with minimum at $x = 0.85$. The resistance values of the Au-interfaces coincide with the four point probe measurements on GCMO thin films (Fig. 16).

The non-volatile bipolar RS is present in the range $0.4 < x < 0.95$, and the switching properties peak in the range $0.7 < x < 0.95$. The concentrations with low x have high bulk resistivity and require large voltage amplitudes to induce switching. The required switching voltages decrease and the asymmetry in switching voltages increases at substitution levels above $x = 0.7$. The optimal calcium concentration for RS was found to be near $x = 0.85$, which is the point where the maximum HRS resistance, the lowest switching voltages and the lowest bulk resistivity are reached (Figs. 18 and 19). The HRS remains above 10^7 Ω in all switching samples, which is beneficial in reducing the sneak-path currents in

crossbar arrays, although full mitigation requires additional measures [116].

4.3 Comparison to other manganites

In order to highlight the differences between the GCMO and other manganite materials, the switching ratios obtained from Al/GCMO over the calcium concentration range x were compared with other studies on manganites (Fig. 18 b). The other materials used in the comparison were Ti/LSMO [43], Au/LSMO [44] and Ti/PCMO [25]. The comparison was made against studies which included a series of devices made with different calcium concentrations, which allowed the determination of the optimal x for each material/electrode combination. The switching ratio was used in the comparison, since absolute values, such as resistances and threshold voltages depend on the size and geometry of the device. The included systems (single crystal $La_{1-x}Sr_{1+x}MnO_4$ and polycrystalline $Pr_{1-x}Ca_xMnO_3$ were chosen in order to highlight the similarity of the phenomenon in Mn-based devices and to show how the GCMO differs from the rest. Some compared materials use Ti as the interface material, which forms a rectifying interface similar to Al. The authors of the Ti/LSMO study point out that the Al-switching in LSMO is equivalent to the Ti-switching, with a slightly lesser switching ratio [43].

Compared to the LSMO and PCMO samples, the high optimum calcium doping of the GCMO is unusual for manganite RS devices, since studies on other materials tend to indicate that a moderate hole-carrier concentration of manganite oxide is a prerequisite for the RS and that a heavy hole doping reduces the effect [25; 44; 43]. In LSMO and PCMO the maximum switching ratio is achieved at the half doping and the optimal region for the GCMO is at $x = 0.9$, a composition where the other materials do not show switching. The result is worth noting, since the compared materials share similar structural and magnetic properties, and the physical mechanism behind the redox-based RS process has been thought to to be similar for all manganite-based devices [26; 22; 80]. Conversely, the results on the GCMO indicate that this conclusion cannot be generalized to all manganite family-based devices. The ability of the GCMO to operate at high calcium dopings also makes it possible to manufacture RS devices with reduced rare-earth metal usage and demonstrates that the understanding of RS in manganites is still incomplete.

4.4 Endurance characteristics

Reliability is an important factor in the design of new electronics and a known weakness of the RS-based devices. It is also an important factor of reproducibility of research results. For this reason, the endurance characteristics of the fabricated devices were analyzed. Both GCMO and PCMO devices were tested by pulsing

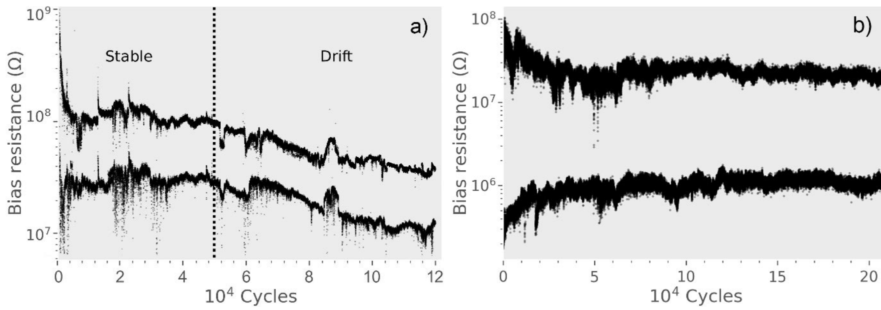

Figure 20. Repeated alternating HRS and LRS pulses on the PCMO device (a) and the GCMO $x = 0.85$ device (b). Figures from **[I,III]**.

them with repeated alternating HRS and LRS write voltages, with a readout in-between the writes. The read voltage was selected to be in the Ohmic voltage region, which ensures a correct reading of the non-volatile state and to avoid possible accidental writes. The used calcium doping for the GMCO was $x = 0.85$, which had been found optimal during the RS characterization.

Devices made of GCMO were tested for $2{\cdot}10^5$ repeated HRS-LRS cycles (Fig. 20 b) and the PCMO devices for 10^5 (Fig. 20 a). The PCMO devices had initially large changes in HRS and LRS resistances, after which the switching ratio stabilized. HRS and LRS states stayed distinguishable with respect to the previous state over the whole experiment, although a visible drift towards lower resistances was seen after $5 \cdot 10^4$ writes. The GCMO devices did not show the resistance drift observed in the PCMO devices and were thus more robust. The observed drift in the PCMO can be explained with the used constant write voltages. A similar effect has been observed in other RS compounds [117], where the local electric field inside the bulk region is lower than at the interface, which causes some vacancies to get stuck inside the bulk instead of returning to the interface region. This lowers the amount of vacancies at the interface over repeated cycling with constant write voltage amplitudes, which in turn lowers the interface resistance. It can be corrected by introducing a feedback loop which adjusts voltage amplitudes dynamically for the optimal switching ratio during operation [118; 117].

The impact of temperature in switching properties of in GCMO was also explored, first by observing the switching loops over different temperature ranges and later by more in-depth investigation on how the materials' conduction model parameters change over the temperature range. The exploratory analysis was made by varying the operating temperature of the device in the range from 100 K to 350 K. Lowering the operating temperature reduced the volatile portion of the switching in GCMO $x = 0.95$, which can be seen in the flattening of the traced LRS-curve in-between the state transitions (Fig. 21). Lowering the temperature increases the minimum LRS resistance, which is sensible, due to the increase in

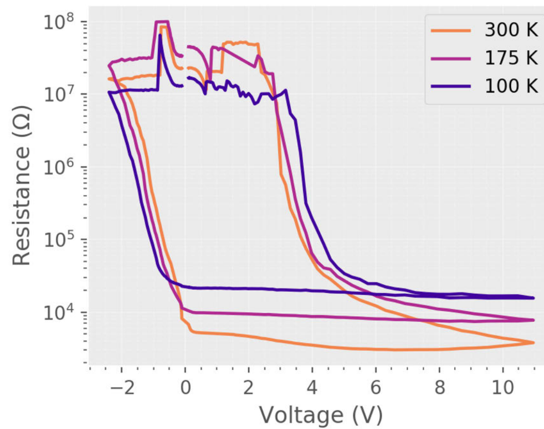

Figure 21. The effect of temperature in switching loops in GCMO $x = 0.85$.

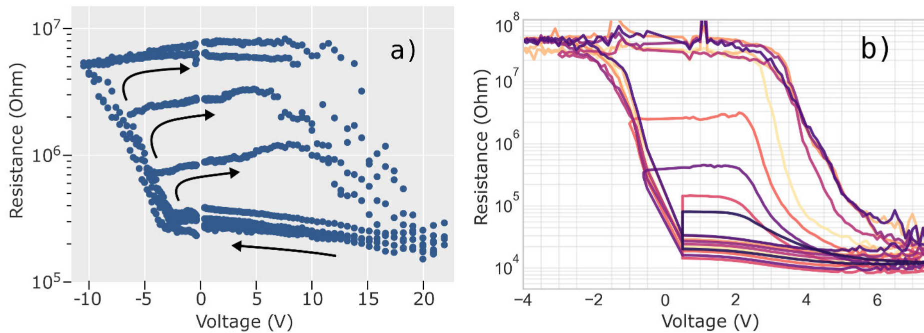

Figure 22. Multilevel switching in PCMO (a) and GCMO $x = 0.8$ (b) with varying negative voltage amplitude. Figures from **[I,III]**.

bulk resistivity. The devices remained functional over the whole tested operating temperature range. The small volatile component of the switching present at higher temperatures could potentially be exploited in spiking neural networks, where information is stored temporally in the volatility of the state. The effect can be modeled using the dynamic memdiode model (DMM)[119] shown in section 5.2.1.

4.5 Control of resistive states

The dependence of the HRS-resistance on the HRS writing voltage amplitude was measured in PCMO in order to demonstrate multistate switching (Fig. 22 a). The HRS write amplitude was varied to give rise to multiple different intermediate resistance states spanning from the HRS resistance to the LRS resistance. The applied LRS write placed the device into a known and stable state which worked

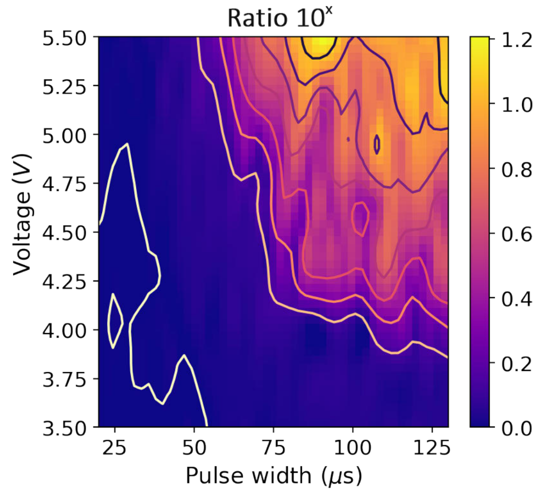

Figure 23. The effect of programming pulse width and amplitude in the switching ratio in GCMO $x = 0.85$.

as a reference point. The remnant resistance measured between the writes (Fig. 22) shows a continuous dependence between the write amplitude and the resistive state. As a result, the resistance of the device can be tuned to a desired value between the limiting HRS and LRS resistances.

Similar studies were repeated with GCMO in addition to more finely controlled timing measurements. The controllability of the RS state in GCMO devices was investigated by measuring the HRS to LRS switching ratio as a function of programming pulse width and voltage amplitude for concentration $x = 0.8$ (Fig. 23). The results from these measurements were used to determine optimal pulse widths and voltage amplitudes which induce the largest switching ratio without damaging the device. The used read voltage for GCMO devices was 450 mV, which was in the linear region. Once the optimal parameters for the GCMO were found, they were used to study the multistate capabilities (Figs. 22 b and 24). The control of the state was repeatable, and both HRS and LRS could be controlled by changing the HRS amplitude, LRS amplitude or both of them simultaneously. The results were used to construct a compact model of the device, which is discussed in more detail in section 5.2. For improved usability in memory and neuromorphic applications, the demonstrated resistive states of both GCMO and PCMO can be extended by introducing more steps in the writing voltages [98; 19].

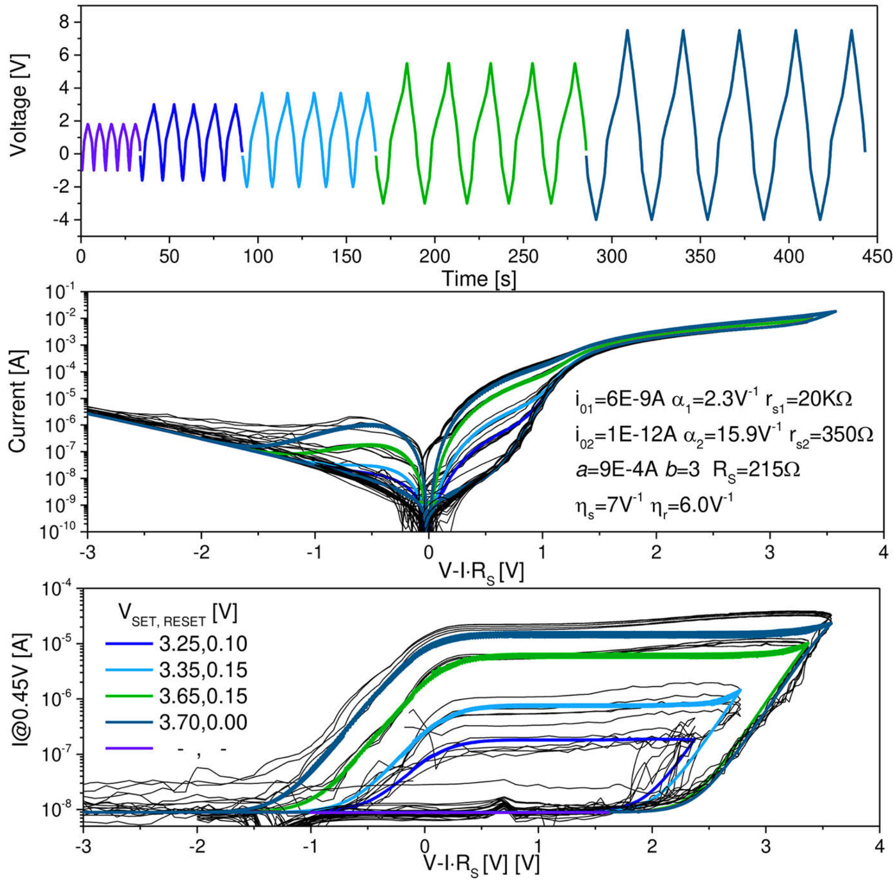

Figure 24. Multilevel switching loops for GCMO $x = 0.8$ with increasing minimum and maximum voltages along with a fitted compact model which reproduces the switching characteristics convincingly, which is discussed in more detail in section 5.2. Figures from **[IV]**.

5 Models and simulations

5.1 Conduction behavior

Better understanding of the physical origin of the RS in the studied devices requires a deeper analysis of the conduction mechanism at the metal-oxide-interface. The exploratory analysis was done by interpreting the measured $I(V)$-curves with the power exponent representation [120]. The method displays the power exponents over the whole measurement range (Fig. 25), which allows for a more in-depth determination of the dominant conduction mechanism than the commonly used method where individual power exponents are obtained by fitting to manually selected regions of interest. The power exponent analysis is done by considering the quantity:

$$\gamma = \mathrm{d}(\ln(|I|))/\mathrm{d}(\ln(|V|)), \tag{3}$$

which shows changes in the conduction exponent by taking the logarithmic derivative of current with respect to voltage, similar to the reduced activation energy method, which has been successfully used in determining thermal transport properties in manganites [121],**[II]**. Different non-linear (NL) elements and their combinations [69] produce distinct $\gamma(V^{1/2})$-relations, which can be used to differentiate between different conduction models. For example, an Ohmic interface ($I \propto V$) will result in a constant $\gamma = 1$, while a space-charge limited conduction (SCLC) ($I \propto V^2$) dominated interface will have a constant of $\gamma = 2$. Conduction mechanisms which have an exponential dependence between current and voltage, such as the Poole-Frenkel (PF) conduction and Schottky conduction, will result in a straight line which will only differ in the y-intercept value (0 for Schottky and 1 for PF) [120].

However, since the electric transport in both GCMO and PCMO devices is not dominated by a single conduction mechanism, the $\gamma(V^{1/2})$ will take on varying shapes due to different dominant conduction mechanisms over the voltage range. In both of the studied materials, the positive polarity has a peak-shaped γ-dependence in both HRS and LRS, which is characteristic for a combination of Ohmic- and Poole-Frenkel-conduction [120]. The γ-dependence of the materials at the negative polarity has two different modes of conduction depending on the resistive state.

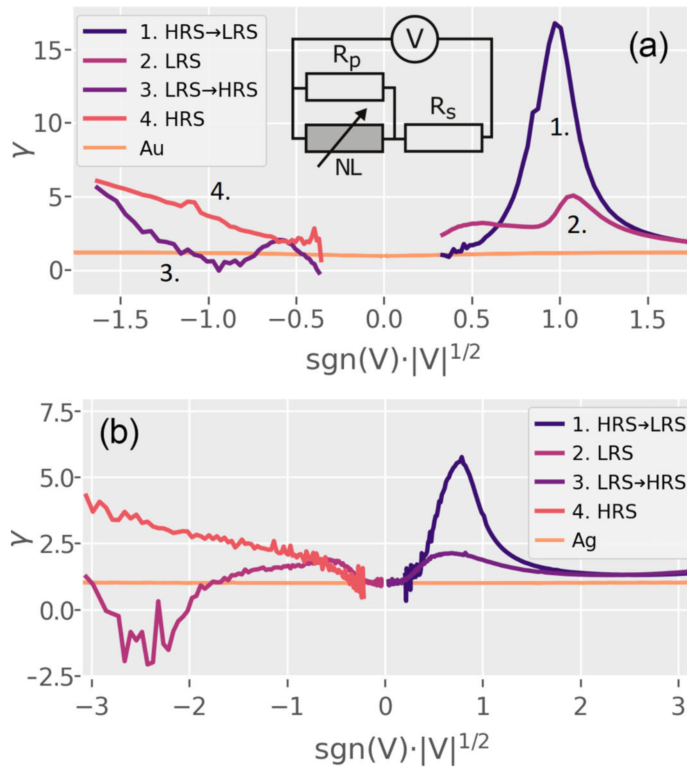

Figure 25. Voltage sweep $\gamma(V^{1/2})$-curves of Ohmic Au-interfaces and Al/GCMO/Au for $x = 0.85$ (a) and Ag/PCMO/Al for $x = 0.4$ (b). The RS and non-linear conduction happen only when an Al-interface is present. The inset in (a) shows the equivalent circuit used in model fits, which consists of a non-linear element NL with series and parallel linear resistances R_s and R_p. Figures from **[I,III]**.

In addition to the polarity, the resistive state affects the γ-behavior as well. In the LRS at both polarities the LRS γ-characteristics are close to symmetrical at amplitudes below the RS transition, indicating a bulk-dominated conduction mechanism. This can be seen from the negative polarity LRS γ-curve, which initially mirrors the peak shape observed at the positive polarity, until the transition to HRS begins. After the transition from LRS to HRS the behavior changes from peak-shaped to linear conduction with a constant slope and an y-intercept of approximately 0 at the negative polarity, indicating a formation of a rectifying barrier. The linear γ-dependence of the negative polarity HRS can be interpreted as a Schottky-like conduction. The mechanism for simultaneous presence of both conduction mechanisms has also been modeled theoretically [122].

The PCMO and GCMO devices display similar characteristics (Fig. 25), which highlights the similarity of conduction mechanisms in manganite memristors. Between the devices, the LRS in PCMO is symmetrical up to higher ampli-

tude than in GCMO, which is consistent with the lower LRS to HRS transition voltage amplitude of GCMO. At the positive polarity the peak voltage of γ is similar in both GCMO and PCMO at calcium concentration $x = 0.4$, but the GCMO has a higher maximum amplitude in γ, owing to its steeper state transition.

5.1.1 Conduction model

To explain the peak-shaped $\gamma(V^{1/2})$-behavior in the positive polarity of the devices, a more complex circuit needs to be introduced. The positive polarity curves of devices with an aluminum interface can be reproduced by creating an equivalent circuit consisting of a non-linear conduction element with Ohmic series and parallel resistances R_s and R_p (Fig. 25). The non-linear element representing the contribution of the aluminum interface can be thought of as a bulk-limited Poole-Frenkel conduction in series with a Schottky diode [122]. The model can be expressed as an implicit equation for I and V at constant temperature:

$$I = A(V\text{-}I \cdot R_s)\left[\exp\left(B\sqrt{V\text{-}I \cdot R_s}\right)\right] + \frac{V\text{-}I \cdot R_s}{R_p}, \tag{4}$$

with $A = \tilde{A}_{PF}\exp\left(\text{-}\,q\phi/k_BT\right)$, $B = q^{3/2}/k_BT\sqrt{\pi\epsilon_0\epsilon' d}$, where T is the temperature, $\tilde{A}_{PF}$ is a normalization factor which also depends on temperature, q the electron charge, ϕ the trap energy level, k_B the Boltzmann constant, ϵ_0 the vacuum permittivity, ϵ' the real part of the dielectric constant, d the distance where the voltage drop is produced, R_s the series resistance and R_p the parallel resistance [120]. The series resistance R_s represents the Ohmic RS-state dependent contribution from the oxide layer and the bulk i.e. R_s is high in HRS and low in LRS. The parallel resistance R_p represents the Ohmic contribution from regions of the interface which do not contribute to the switching, an R_p higher than the bulk resistivity is a requirement for RS.

The resistive switching influences the AlO_x layer, which translates into modulation of the rectifying barrier of the NL-element [123] and determines its contribution to the total resistance of the device. In the LRS the oxide layer represented by the R_s is thinner and the amount of rectification is reduced. Conversely, in the HRS the barrier is thicker and the interface becomes more rectifying. When the NL element is forward biased the PF contribution dominates over the Schottky mechanism and while in the reverse bias the dominating mechanism can be either Schottky or PF depending on the RS state.

The introduced circuit model can be used in analysis when the RS devices are in a state where the Poole-Frenkel-based conduction dominates. Based on the qualitative analysis presented earlier, the studied materials have a dominating PF-contribution with linear series and parallel resistances R_s and R_p at positive polarity over both HRS and LRS, and at the negative polarity before the LRS

to HRS transition. Out of the PF-shaped curves the HRS has higher maximum exponent than the LRS. Similar peak shape has also been seen in other perovskite compounds in addition to PCMO and GCMO, such as the $La_{1-x}Sr_xCoO_3$ [124]. The negative polarity HRS was excluded from the model-based analysis, since the conduction resembles rectifying Schottky conduction instead of PF-conduction (Figs. 25). The highly rectifying interface and the stochastic transition from PF to Schottky-like conduction is difficult to reproduce using physical models [14].

5.1.2 Model fit results

The conduction model (4) can be used to separate Ohmic components from the positive $I(V)$ curve and examine the underlying Poole-Frenkel conduction, which combined with the temperature measurements gives an access to the Poole-Frenkel trap energy level ϕ. The fitting for free parameters A, B, R_s and R_p of equation (4) was made by numerically solving the implicit equation by iteratively minimizing the error with respect to the experimental data by using a combination of basin-hopping and Broyden-Fletcher-Goldfarb-Shanno (BGFS) algorithm. The data used in the fits was collected from the positive polarity where Schottky-like conduction was not present.

In PCMO the used calcium concentration was $x = 0.4$. The fits were made at the positive polarity for both HRS and LRS in order to gauge how well the model was able to reproduce the two extremes of the possible RS states. The obtained results agree with experimental observations and reproduce the γ behavior (Fig. 26). The series resistance values R_s are close to the measured experimental values of $6.8 \cdot 10^6\ \Omega$ for HRS and $5.6 \cdot 10^4\ \Omega$ for LRS, and the parallel resistance R_p is close to the resistance measured from Ohmic Ag/PCMO/Ag interfaces, which corresponds to a situation where the oxide layer R_s and the PF-element are not present. From the parameter A it can be qualitatively deduced, that the trap energy level ϕ_B is larger in HRS than in the LRS ($A_{\text{HRS}} \approx 10^{-10}$ vs. $A_{\text{LRS}} \approx 10^{-6}$), which is in line with the proposed modification of the AlO_x interface layer thickness, which also reduces the oxygen content of the perovskite structure near the interface at HRS.

In GCMO, the whole calcium series was analyzed using the method described earlier. The comparisons between the calcium concentrations were made on the positive voltage polarity of the HRS, because there is a continuum of possible RS states, out of which HRS represent the maximal difference from the non-switching Ohmic interface (Fig. 25). The room-temperature fits were measured for samples in range $0.1 \leq x \leq 1.0$. The model coincided with the experimental data at room temperature and reproduced the experimental $I(V)$-relation for voltages above 400 mV (Fig. 26). The series resistances R_s coincide with the resistance of GCMO with Ohmic electrodes (Fig. 18). The parallel resistances R_p were also in

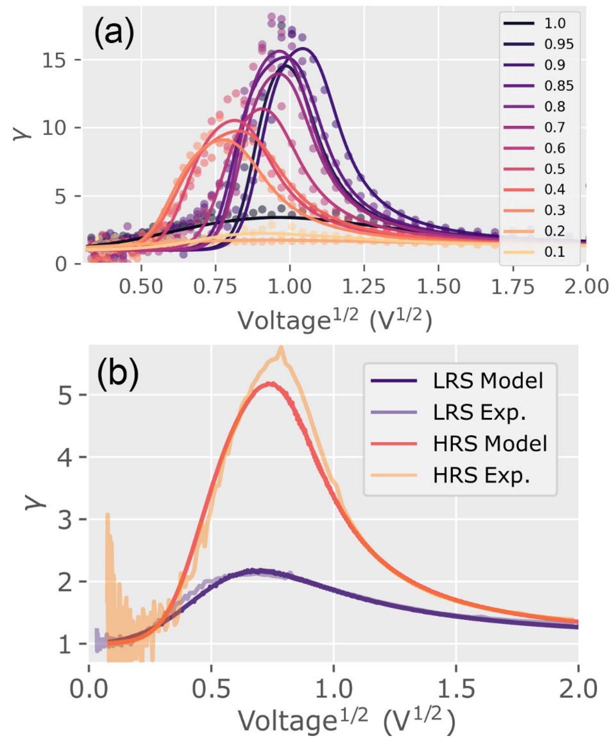

Figure 26. Fitted and experimental values of $\gamma(V^{1/2})$ and $I(V)$ over the doping x at room temperature for GCMO (a) and PCMO (b). In GCMO the transition is more abrupt at higher substitutions. The PCMO result shows that the LRS behavior is closer to Ohmic conduction. Figures from **[I,III]**.

the same order of magnitude as the HRS states in switching Al/GCMO interfaces (Fig. 18).

Temperature dependence

The PF trap energy level ϕ was determined over the GCMO calcium doping range by measuring the $I(V)$-properties as a function of temperature. The samples were set to the HRS at 300 K, after which they were measured over the temperature range. The $I(V)$-measurements used the maximum voltage amplitude which did not induce switching at the used temperatures. The measurements consisted of initially going to the maximum temperature of 350 K, after which the temperature was lowered to 250 K in steps of 25 K. Experimental data from each temperature measurement was fitted to the conduction model (Fig. 27). Fitting for ϕ was made for concentrations which had RS and a linear Arrhenius relation $\ln(A) - 1/T$, this corresponded to the x range from 0.4 to 0.95 (Fig. 28). The trap-energy level for x in the range from 0.4 to 0.6 is close to 1 eV. In the x range from 0.6 to 0.8 the value

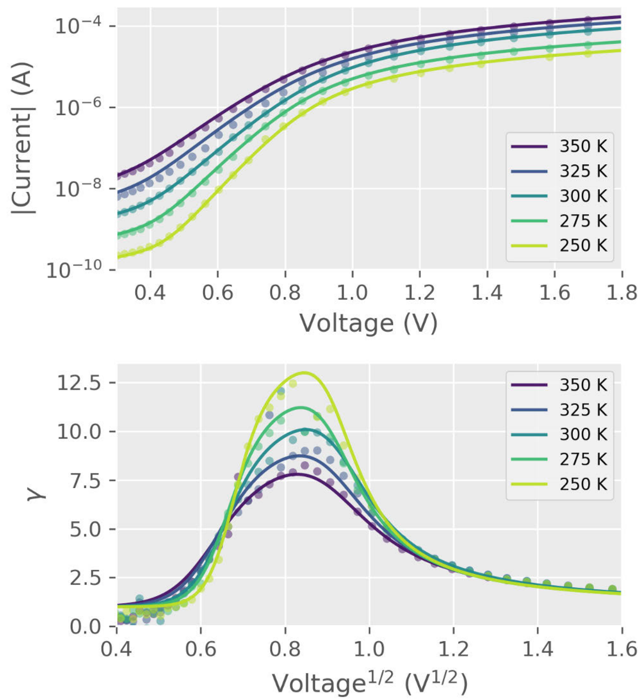

Figure 27. Fitted and experimental values for $\gamma(V^{1/2})$ and $I(V)$ for $x = 0.4$ over the temperature range. Figures from **[III]**.

of ϕ decreases to 0.3 eV and begins to increase again at x above 0.8. The lowest point of ϕ at $x = 0.8$ coincides with the region of the highest switching ratio (Fig. 18), which suggests that the magnitude of resistive switching is related to changes in trap-energy level. The minimum also has the lowest threshold voltage needed for inducing HRS to LRS transition and corresponds to the lowest point in bulk resistance of GCMO (Fig. 18). The RS in Al/GCMO seems to be correlated with low bulk resistance and shallow traps at the active interface, which is useful knowledge for the further optimization of the interface layer.

5.2 Compact modeling

The RS behavior of GCMO can be accurately modeled with compact modeling (Fig. 24). Compact models of circuit elements are models that are sufficiently simple to be incorporated in circuit simulators, but also sufficiently accurate to be useful to circuit designers. Compact models focus on the representation of the system, but not how it functions physically. In case of memristor devices, the models should be compatible with experiments by reproducing the hysteretic behavior and other related phenomena.

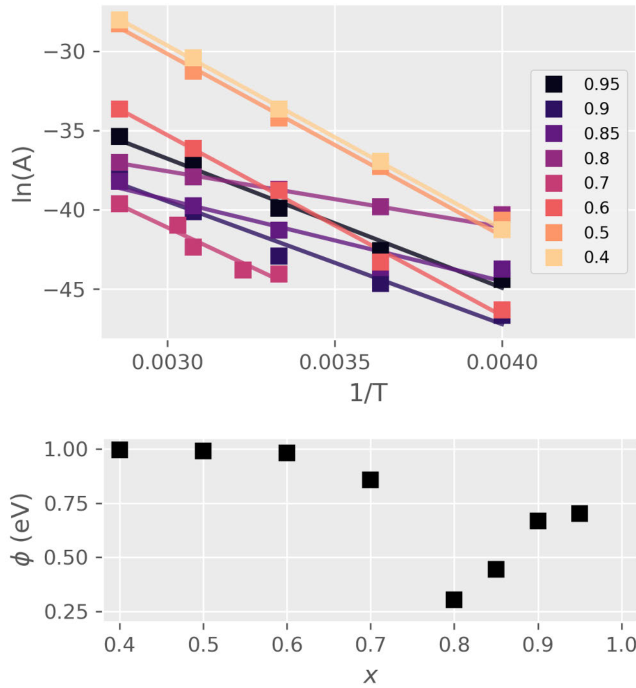

Figure 28. Arrhenius plots and PF trap energy levels ϕ from the model fit. The substitution values x where trap energy level ϕ deviates from 1 eV also correspond to good RS properties in terms of switching ratio. Figures from **[III]**.

5.2.1 The memdiode model

The compact model which was used to model the $I(V)$-curves of the memristor devices (Figs. 29 d and 30 a) consists of equations which model the memristive system by modeling the current conduction and hysteretic behavior by assuming that the system consists of multiple small filamentary conduction paths which can be ruptured and formed controllably.

Memdiode current equation

In order to model the current passing through the memristive device, we consider the device as an ensemble of individual conductive pathways, which have a distribution of confinement barrier heights ϕ:

$$i(V) = \frac{2e}{h\alpha}\exp(-2\alpha\phi)\sinh(\alpha eV)$$

The total current passing through the device as a function of voltage V requires considering the effective total barrier height ϕ_{eff}, which we can do by assuming

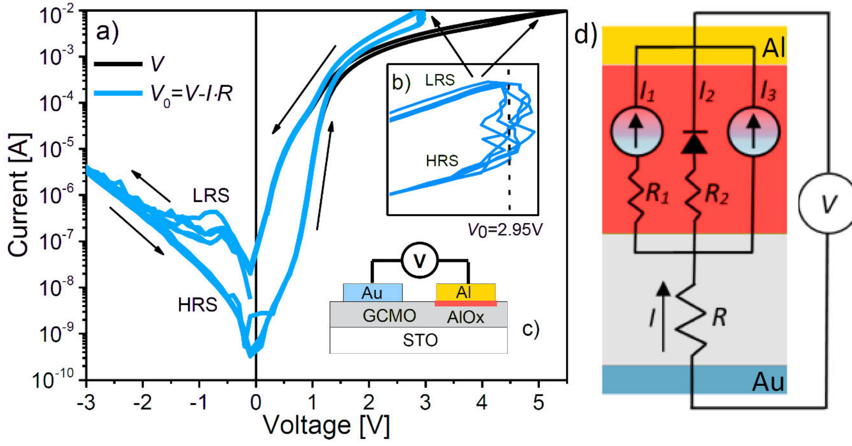

Figure 29. a) Experimental $I(V)$-curve ($R = 265\Omega$). b) Detail of the current increse at V_{T}. c) Structure of the investigated devices. d) The equivalent circuit model. Figures from **[IV]**.

that the individual barrier heights are normally distributed:

$$f(\phi) = \frac{1}{\sqrt{2\pi}\sigma} \exp\left[-\frac{(\phi - \phi_0)^2}{2\sigma^2}\right]$$

With this assumption, the total current I at voltage V with effective barrier height ϕ_{eff} can be gotten by taking a superposition of all individual conductive pathways:

$$I(V) = \int_{-\infty}^{+\infty} f(\phi) i(V, \phi) d\phi = \frac{2e}{h\alpha} \exp\left(-2\alpha\phi_{\text{eff}}\right) \sinh(\alpha e V)$$

The resulting equation implies that the current dependence on V is exponential in HRS and linear in LRS ($\alpha \rightarrow 0$), which is in agreement with experimental measurements (Fig. 25). The equation can be seen as two back-to-back connected diodes when modeled as circuit elements.

Memdiode state equation

As with the memdiode current equation, the memdiode state equation also assumes that the memristive device consists of multiple individual conductive pathways, which have a normal distribution of individual set voltages V_S:

$$f(V_S) = \frac{1}{\sqrt{2\pi}\sigma} \exp\left[-\frac{(V_S - V_{S0})^2}{2\sigma^2}\right]$$

The number of active conductive pathways can be normalized by taking a convolution over the individual set voltages V_S:

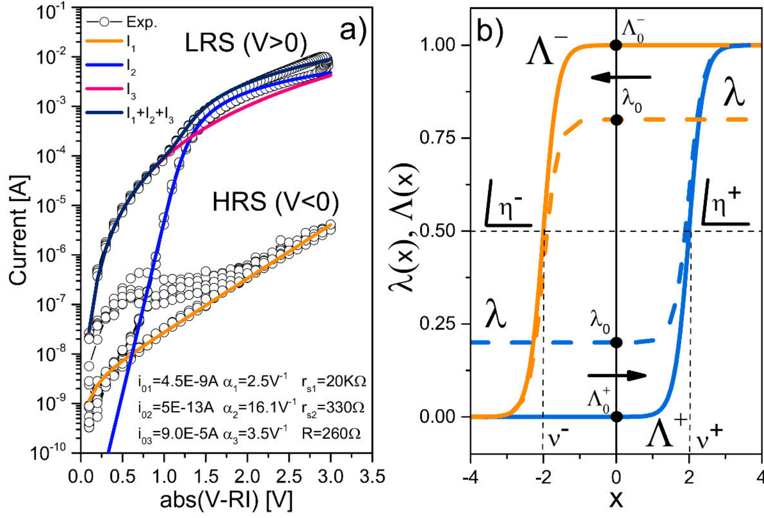

Figure 30. a) The experimental and model $I(V)$-curves (8)-(10). b) The Hysteron (solid) and self-similar minor loop (dashed) corresponding to equations for $\lambda(x)$ (5) and $\Lambda^{\pm}(x)$ (7) respectively, $\eta^{\pm}$ are the transition rates and $v^{\pm}$ are the set and reset parameters. Figures from **[IV]**.

$$\lambda(V) = \int_{-\infty}^{+\infty} H\left(V - V_S\right) f\left(V_S\right) dV_S,$$

where H is the Heaviside step function. The result is the following equation, which implies that the number of conductive pathways as a function of V follows the logistic curve:

$$\lambda(V) = \frac{1}{2}\left[1 + \operatorname{erf}\left(\frac{V - V_{S0}}{\sqrt{2}\sigma}\right)\right] \approx \left\{1 + \exp\left[-\eta\left(V - V_{S0}\right)\right]\right\}^{-1}$$

From this result we get:

$$\frac{d\lambda}{dV} = \eta\lambda(1-\lambda),$$

and arrive into the final form of the memdiode state equation [125]:

$$\frac{d\lambda}{dt} = \frac{d\lambda}{dV}\frac{dV}{dt} = \eta\lambda(1-\lambda)\frac{dV}{dt} = \eta\lambda(1-\lambda)\dot{V},$$

which is a differential equation for a voltage-controlled current source, where λ is the memory state (Fig. 31), which corresponds to the Strukov's window function $\dot{\Lambda} \sim \Lambda(1-\Lambda)$ [15; 126; 127]. The derived candidate memory equation does not take into account the ionic movement over time when the voltage stays constant. Our static model predicts $\frac{d\lambda}{dt} = 0$ when the supplied voltage V remains

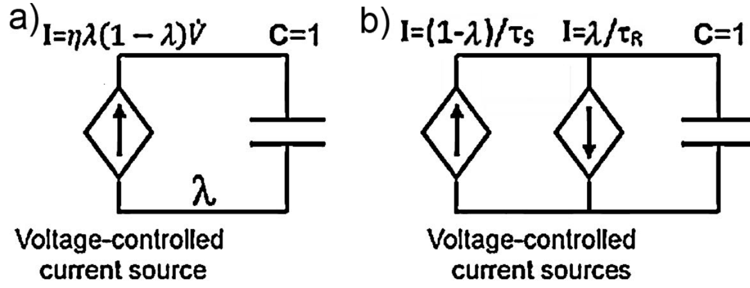

Figure 31. a) Memdiode state equation equivalent circuit. b) Equivalent circuit with ion movement over time taken into account.

constant, which is not correct for every real RS device. The time dependence can be taken into account by using the dynamic memdiode model (DMM)[119], which takes into consideration ionic hopping by including time constants for set and reset events:

$$I(V) = I_0(\lambda)\sinh(\alpha e V)$$
$$\frac{d\lambda}{dt} = \frac{1-\lambda}{\tau_{SET}} - \frac{\lambda}{\tau_{RES}},$$

where the time constant equations describing ion hopping frequency are:

$$\tau_{SET} = \tau_{0S}\exp\left(-\tau_{0S}|V|\right)$$
$$\tau_{RES} = \tau_{0R}\exp\left(-\tau_{0R}|V|\right).$$

However, the static model provides an adequate approximation to model the general behavior of the device, and as such was used to model the non-dynamic behavior of the GCMO.

Memdiode memory equation

The memory equation describes the hysteretic behavior of the device using Ridge functions. The Ridge functions obey $f(\boldsymbol{x}) = g(\boldsymbol{x}\cdot\boldsymbol{a})$ for some $g : \mathbb{R} \to \mathbb{R}$ and $\boldsymbol{a} \in \mathbb{R}^d$ i.e. the function is an affine transformation composed with a function of one variable. To form the memory equation, we begin with the Krasnosel'skii-Pokrovskii (KP) hysteresis operator [128], which is defined as:

$$L\left[t_0, \lambda_0\right]V(t) \equiv \min\left\{\Lambda^-[V(t)], \max\left[\lambda_0, \Lambda^+[V(t)]\right]\right\},$$

where $\lambda(t) = L\left[t_0, \lambda_0\right]V(t)$ and $\lambda\left(t_0\right) = \lambda_0$. The Λ^- and Λ^+ are taken to be sigmoidal functions which satisfy the condition:

$$\Lambda(x) = \begin{cases} 1 & x \to \infty \\ 0 & x \to -\infty \end{cases}.$$

The operator adheres the Takács principle of self-similarity of the inner loops: $\lambda(V_l) = A\Lambda(V_l) + B$, which makes it suitable for modeling the observed self-similar hysteretic loops of the memristive devices (Fig. 24).

With the KP operator as a basis, we arrive into a form of the memory equation which is an affine transformation of $\Lambda^{\pm}$, and can be used in the device simulations [119; 129]:

$$\lambda(x) = \begin{cases} \frac{\lambda_0 - 1}{\Lambda_0^+ - 1}\Lambda^+(x) + \frac{\Lambda_0^+ - \lambda_0}{\Lambda_0^+ - 1} & \dot{x} \geqslant 0 \\ \frac{\lambda_0}{\Lambda_0^-}\Lambda^-(x) & \dot{x} < 0 \end{cases}, \tag{5}$$

where $\Lambda_0^{\pm} = \Lambda^{\pm}(0)$ and $\lambda_0 = \lambda(0)$ and $\dot{x}$ is the time derivative of x. The $\Lambda^{\pm}$ can be any sigmoidal function satisfying $\Lambda^{\pm}(x \to \infty) = 1$ and $\Lambda^{\pm}(x \to -\infty) = 0$. The equation (5) generalizes the method introduced in [125] by introducing soft transitions into the hysteron structure.

Solving the memory state evolution (5) for an arbitrary input signal $V(t) = V_{\mathrm{t}}$ requires discretizing it using $\lambda = \lambda_t$, $\lambda_0 = \lambda_{\mathrm{t}-1}$, $\Lambda^{\pm} = \Lambda^{\pm}$ and $\Lambda^{\pm}{}_0 = \Lambda^{\pm}\mathrm{t} - 1$ so that the current memory state (t) depends on the previous state (t-1) as expected for a Markovian behavior:

$$\lambda_t = \left\{ \frac{\lambda_{t-1} - 1}{\Lambda^+(V_{t-1}) - 1}\left[\Lambda^+(V_t) - 1\right] + 1 \right\} H(V_t) + \left\{ \frac{\lambda_{t-1}}{\Lambda^-(V_{t-1})}\Lambda^-(V_t) \right\} H(-V_t) \tag{6}$$

The choice of $\Lambda^{\pm}$ affects the resulting switching dynamics. It is used to describe the creation and destruction of conducting channels in the RS device. Our compact model uses the logistic hysteron, justified by the derivation above:

$$\Lambda^{\pm}(x) = \left\{1 + \exp\left[-\eta^{\pm}\left(x - v^{\pm}\right)\right]\right\}^{-1}, \tag{7}$$

where $\eta^{\pm}$ are the set and reset transition rates and $v^{\pm}$ the set and reset threshold parameters, $-\infty \leq x \leq \infty$ and $0 < \Lambda^{\pm}(x) < 1$.

5.2.2 Applying the model to the GCMO device

The RS behavior of GCMO can be accurately modeled with the introduced memdiode model. The model is tied to the GCMO memristor device with the following equations:

$$I_1 = I_{01}\sinh\left[\alpha_1\left(V_0 - I_1 R_1\right)\right] \tag{8}$$

$$I_2 = I_{02}\left\{\exp\left[\alpha_2\left(V_0 - I_2 R_2\right)\right] - 1\right\} \tag{9}$$

$$I_3 = I_{03}\lambda\left(V_0\right)V_0^{\alpha_3}, \tag{10}$$

where $I = I_1 + I_2 + I_3$ and $V_0 = V - IR$, and the three current equations I_1, I_2 and I_3 are associated with the tunneling (memdiode state equation), Schottky-like conduction, and the soft-breakdown conduction in the AlO_x layer (memdiode memory equation) respectively (Fig. 29) [20; 130; 69; 131; 132],**[III]**, without ruling out the possibility of the Poole-Frenkel conduction. The α_i, I_{0i} and R_i, $i = 1, 2, 3$ are fitting parameters, R the GCMO bulk resistance found from the vertical current increase happening at the HRS to LRS transition voltage V_T, which can be seen from the $V_0 = V - IR$ curve of the device (Fig. 29 b). The equations (8) and (9) are independent of memory state, but the third equation (10) with λ from equation (5) and $0 \leq \lambda \leq 1$ takes into account the reversible changes in the effective area of the micro-filaments caused by the oxygen vacancy movement at the interface. The equations (8)-(10) constitute the compact model as a system of non-linear equations, which were formulated as a circuit model and solved numerically using a Spice simulator.

Results and qualitative assessment

The resulting LTSpice model is presented below:

```
* Model parameters
.subckt GCMO + - R
.params
+ H0=0 rs=215 CH0=1e-4 del=0.01 vp=0.1
+ i01=6E-9 a1=2.3 rs1=20K
+ i02=1E-12 a2=15.9 rs2=350
+ i03=9e-4 a3=3
+ nset=7 vset=2 nres=6 vres=0
* Memory equation
BH 0 H I=if(ddt(V(A,-))>=0,((D(V(H))-1)*S(V(A,-))
+ +S(D(V(A,-)))-D(V(H)))/(S(D(V(A,-)))-1),
+ D(V(H))/R(D(V(A,-)))*R(V(A,-))) Rpar=1
CH H 0{CH0} ic={H0}
* I-V curve
RS + A {rs}
RS1 A B {rs1}
BD1 B - I=i01*sinh(a1*V(B,-)
RS2 A C {rs2}
BD2 C - I=i02*(exp(a2*V(C,-))-1)
BPL A - I=V(H)*i03*V(A,-)**a3
* Read current
BI 0 R I=i01*sinh(a1*vp)+i02*(exp(a2*vp)-1)
+ +V(H)*i03*vp**a3
* Auxiliary functions
.func D(x)=delay(x,del)
.func S(x)=1/(1+exp(-nset*(x-vset)))
.func R(x)=1/(1+exp(-nres*(x-vres)))
.ends
```

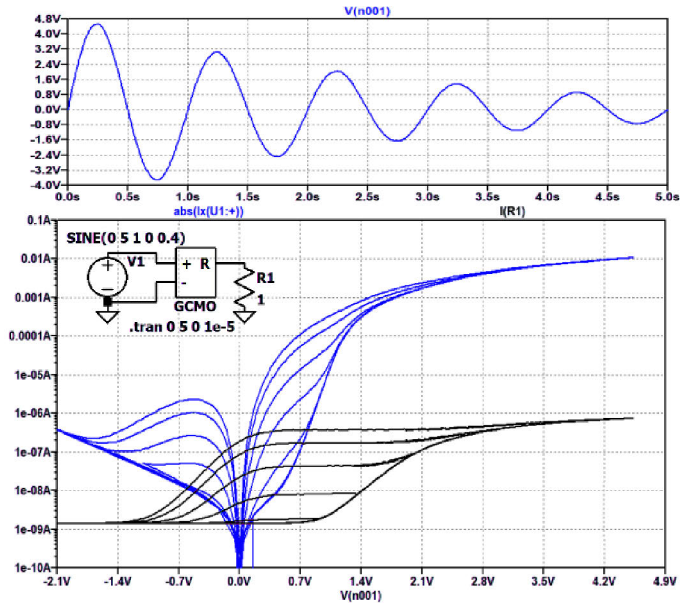

Figure 32. Input signal and simulation results for a read current $vp = 0.1\mathrm{V}$. Figures from **[IV]**.

Visualized results of a simulation with input signal similar to voltage sweeps used in real devices can be seen in the Figs. 24 and 32. The simulation loops were driven by a damped sinusoidal voltage instead of triangular waveforms in order to improve the stability of the simulation. The results show that the proposed model can be used in a circuit simulator and reproduces the hysteretic behavior of the real GCMO devices. The compact model can be used as a part of a larger system, which allows exploring the usage of GCMO memristors in a variety of circuit design applications ranging from memory devices to neuromorphic systems.

5.3 Spike-timing-dependent plasticity

Spike timing dependent plasticity (STDP) is a type of synaptic plasticity that is dependent on the timing of the pre- and post-synaptic voltage spikes supplied into a spiking neuromorphic device [133] consisting of a synapse and neuron (Fig. 1 b). The STDP learning rule leads to Hebbian learning, where the timing of the pre- and post-synaptic spikes determines the strength of the synaptic connection. STDP can be used as a learning rule in neuromorphic computing, where it can be used to learn temporal relationships between input spikes, resulting in ability to perform unsupervised learning tasks, such as pattern recognition [134].

In order to implement STDP in hardware, a memristor device with temporal volatility, or a clocked non-volatile memristor circuit with well controlled resistive state is used [135]. In our devices, the STDP is achieved with a clocked circuit,

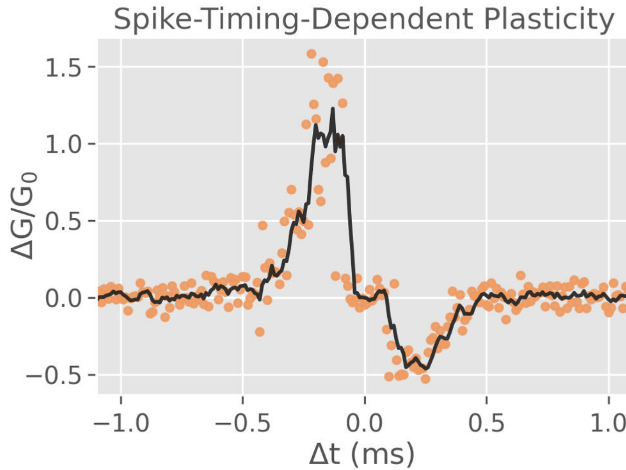

Figure 33. Spike-timing-dependent plasticity (STDP) in a GCMO $x = 0.7$ memristor device. The memristor was subjected to a series of pre- and post-synaptic spikes with different amplitudes and timings. The results show the typical STDP behavior, with the synaptic strength (conductance ratio) increasing when the pre- and post-synaptic spikes are close in time and in correct temporal order, and decreasing when they are not in right order. Spikes which are temporally far apart have no effect in device state.

where each clock cycle represents a discrete step in time. Pre- and post-synaptic spikes are represented as waveforms of individual pulses of the shape seen in the Fig. 12, which are fed through the device, affecting the device state. As a result, we can observe the characteristic STDP behavior, as seen in Fig. 33. The synaptic strength (conductance ratio) of the device increases when the pre- and post-synaptic spikes are close in time and in correct temporal order, and decreases when the post-synaptic spike is not not causal with the pre-synaptic spike. Spikes which are temporally far apart have no effect in device state.

The results indicate that the GCMO-based memristor circuit can be used to learn temporal relationships between input spikes, similar to how STDP works in biological synapses. Furthermore, the results can be fitted to a simple exponential model:

$$W(\Delta t) = \begin{cases} A_{\text{pre}}\, e^{-\Delta t/\tau_{\text{pre}}} & \text{if } \Delta t > 0 \\ A_{\text{post}}\, e^{\Delta t/\tau_{\text{post}}} & \text{if } \Delta t < 0 \end{cases}$$

where A_{pre} and A_{post} are the maximal changes in conductance, and τ_{pre} and τ_{post} the time constants [134], and the obtained parameters can then be used in a neuronal dynamic simulation, such as the leaky integrate-and-fire-based unsupervised learning network proposed by Diehl and Cook [134]. Such demonstration was done in [136], based on the groundwork and an omitted spiking neural network (SNN) simulation developed during this dissertation work.

6 Conclusions

To summarize, resistive switching devices were fabricated from the mixed-valence manganites $Pr_{0.6}Ca_{0.4}MnO_3$ and $Gd_{1-x}Ca_xMnO_3$. The devices exhibit bipolar switching with multiple intermediate resistive states when fabricated with an asymmetric combination of passive Ohmic interface and a rectifying Al-interface. The switching was shown to be non-volatile and repeatable between samples and measurement runs. The optimal RS concentration for GCMO with operating voltages and switching ratio taken into account was determined to be near $x = 0.9$. This is an unusual result compared to other similar manganites, where the optimal value is close to the half-doping, and no switching is observed at high calcium substitution values.

An analysis of the conduction model for both GCMO and PCMO suggests an interplay of bulk-limited Poole-Frenkel conduction and interface-limited Schottky conduction, which depends on the device state. The negative polarity HRS conduction was Schottky-like, while other states obeyed Poole-Frenkel conduction with linear series and parallel resistances. Temperature measurements performed on GCMO showed changes in the Poole-Frenkel trap energy ϕ in the range from 0.3 eV to 1.0 eV. The lower ϕ values were associated with low bulk resistivity good RS properties in terms of high switching ratio. The results suggest that the switching is caused by modulation of the AlO_x barrier thickness due to a field-assisted oxygen vacancy migration.

The resistance states of both GCMO and PCMO show a well-defined dependence on the write voltages, which allows for a selection of resistance values between two limiting values when a suitable programming sequence is used. The switching behavior of the GCMO memristor was also successfully modeled with a compact model, reproducing the hysteretic behavior of the device.

The work of this dissertation shows that the GCMO-based devices are on par with the other manganite RS materials. The high optimal calcium doping of the GCMO could lead to competitive RS devices with reduced rare-earth metal usage, and the well-controlled resistive state makes them a good candidate for both memory and neuromorphic applications.

List of References

[1] A Holst. Amount of data created, consumed, and stored 2010-2025. *Technology & Telecommunications Retrieved*, pages 06–29, 2021.

[2] S Kim and M Popovici. Future of dynamic random-access memory as main memory. *MRS Bulletin*, 43(5):334–339, 2018.

[3] D Ielmini. Brain-inspired computing with resistive switching memory (RRAM): Devices, synapses and neural networks. *Microelectronics Engineering*, 190:44–53, 2018.

[4] D Ielmini and H Wong. In-memory computing with resistive switching devices. *Nature Electronics*, 1:333–343, 2018.

[5] M Zidan, J Strachan, and W Lu. The future of electronics based on memristive systems. *Nature Electronics*, 1:22, 2018.

[6] E Linn, R Rosezin, S Tappertzhofen, U Böttger, and R Waser. Beyond von neumann—logic operations in passive crossbar arrays alongside memory operations. *Nanotechnology*, 23: 305205, 2012.

[7] K Roy, A Jaiswal, and P Panda. Towards spike-based machine intelligence with neuromorphic computing. *Nature*, 575(7784):607–617, 2019.

[8] S Moradi and R Manohar. The impact of on-chip communication on memory technologies for neuromorphic systems. *Journal of Physics D: Applied Physics*, 52:014003, 2019.

[9] W Maass. Energy-efficient neural network chips approach human recognition capabilities. *Proceedings of the National Academy of Sciences*, 113:11387–11389, 2016.

[10] T Hickmott. Low-frequency negative resistance in thin anodic oxide films. *Journal of Applied Physics*, 33(9):2669–2682, 1962.

[11] L Chua. Memristor-the missing circuit element. *IEEE Transactions on circuit theory*, 18(5): 507–519, 1971.

[12] L Chua. How we predicted the memristor. *Nature Electronics*, 1(5):322–322, 2018.

[13] L Chua and S Kang. Memristive devices and systems. *Proceedings of the IEEE*, 64(2): 209–223, 1976.

[14] F Aguirre, S Pazos, F Palumbo, J Suñé, and E Miranda. Application of the quasi-static memdiode model in cross-point arrays for large dataset pattern recognition. *IEEE Access*, 8: 202174–202193, 2020.

[15] D Strukov, G Snider, D Stewart, and R Williams. The missing memristor found. *Nature*, 453 (7191):80–83, 2008.

[16] Editorial. The memristor revisited. *Nature Electronics*, 1:261, 2018.

[17] L Goux, P Czarnecki, Y Chen, L Pantisano, X Wang, R Degraeve, B Govoreanu, M Jurczak, DJ Wouters, and L Altimime. Evidences of oxygen-mediated resistive-switching mechanism in $TiN\backslash HfO_2\backslash Pt$ cells. *Applied Physics Letters*, 97(24):243509, 2010.

[18] X Hong, D Loy, P Dananjaya, F Tan, C Ng, and W Lew. Oxide–based RRAM materials for neuromorphic computing. *Journal of Materials Science*, 53:8720–8746, 2018. ISSN 1573-4803.

[19] S Jo, T Chang, I Ebong, B Bhadviya, P Mazumder, and W Lu. Nanoscale memristor device as synapse in neuromorphic systems. *Nano Letters*, 10:1297–1301, 2010.

[20] F Zahoor, Azni Z, and F Khanday. Resistive random access memory (RRAM): an overview of materials, switching mechanism, performance, multilevel cell (MLC) storage, modeling, and applications. *Nanoscale Research Letters*, 15:1–26, 2020.

[21] D Lee and Hwang H. $Pr_{0.7}Ca_{0.3}MnO_3$ (PCMO)-based synaptic devices. In *Neuro-inspired Computing Using Resistive Synaptic Devices, $Pr_{0.7}Ca_{0.3}MnO_3$ (PCMO)-Based Synaptic Devices*, pages 53–71. Springer, 2017.

[22] A Sawa. Resistive switching in transition metal oxides. *Materials Today*, 11:28–36, 2008.

[23] T Shi, R Wang, Z Wu, Y Sun, J An, and Q Liu. A review of resistive switching devices: Performance improvement, characterization, and applications. *Small Structures*, 2(4):2000109, 2021.

[24] M Lanza, H Wong, E Pop, D Ielmini, D Strukov, B Regan, L Larcher, M Villena, J Yang, and L Goux. Recommended methods to study resistive switching devices. *Advanced Electronic Materials*, 5(1):1800143, 2019.

[25] S Asanuma, H Akoh, H Yamada, and A Sawa. Relationship between resistive switching characteristics and band diagrams of Ti/$Pr_{1-x}Ca_xMnO_3$ junctions. *Physical Review B*, 80: 235113, 2009.

[26] M Rozenberg, M J Sanchez, R Weht, C Acha, F Gomez-Marlasca, and P Levy. Mechanism for bipolar resistive switching in transition-metal oxides. *Physical Review B*, 81:115101, 2010.

[27] T Kramer, M Scherff, D Mierwaldt, J Hoffmann, and C Jooss. Role of oxygen vacancies for resistive switching in noble metal sandwiched $Pr_{0.67}Ca_{0.33}MnO_3$-δ. *Applied Physics Letters*, 110:243502, 2017.

[28] N Tulina, A Ivanov, A Rossolenko, I Shmytko, A Ionov, R Mozhchil, S Bozhko, I Borisenko, and V Tulin. X-ray photoelectron spectroscopy studies of electronic structure of $Nd_{2-x}Ce_xCuO_{4-y}$ and $YBa_2Cu_3O_{7-y}$ epitaxial film surfaces and resistive switchings in high temperature superconductor-based heterostructures. *Materials Letters*, 203:97–99, 2017.

[29] T Seong, B Lee, K Choi, S Kweon, B Kim, K Jung, J Moon, K Lee, K Hong, and S Nahm. Unipolar resistive switching properties of amorphous $Pr_{0.7}Ca_{0.3}MnO_3$ films grown on a Pt/Ti/SiO_2/Si substrate. *Current Applied Physics*, 14:538–542, 2014.

[30] S Toyoda, T Namiki, E Sakai, K Nakata, M Oshima, and H Kumigashira. Chemical-state-resolved depth profiles of Al/$Pr_{0.7}Ca_{0.3}MnO_3$ stacked structures for application in resistive switching devices. *Journal of Applied Physics*, 114:243711, 2013.

[31] Z Zhang, Y Wang, Y Luo, Y He, M Ma, R Yang, and H Li. Electrochemical metallization cell with anion supplying active electrode. *Scientific reports*, 8(1):1–9, 2018.

[32] J Lee, S Lee, and T Noh. Resistive switching phenomena: A review of statistical physics approaches. *Applied Physics Reviews*, 2:031303, 2015.

[33] C Schindler, S Thermadam, R Waser, and M Kozicki. Bipolar and unipolar resistive switching in Cu-doped SiO_2. *IEEE Transactions on Electron Devices*, 54(10):2762–2768, 2007.

[34] D Jeong, H Schroeder, and R Waser. Coexistence of bipolar and unipolar resistive switching behaviors in a $Pt\backslash TiO_2\backslash Pt$ stack. *Electrochemical and Solid State Letters*, 10(8):G51, 2007.

[35] L Yao, S Inkinen, and S Van Dijken. Direct observation of oxygen vacancy-driven structural and resistive phase transitions in $La_{2/3}Sr_{1/3}MnO_3$. *Nature communications*, 8(1):1–9, 2017.

[36] W Wang, M Laudato, E Ambrosi, A Bricalli, E Covi, Y Lin, and D Ielmini. Volatile resistive switching memory based on Ag ion drift/diffusion Part I: Numerical modeling. *IEEE Transactions on Electron Devices*, 66(9):3795–3801, 2019.

[37] S Rehman, J Hur, and D Kim. Resistive switching in solution-processed copper oxide (Cu_xO) by stoichiometry tuning. *The Journal of Physical Chemistry C*, 122(20):11076–11085, 2018.

[38] A Mehonic, A Vrajitoarea, S Cueff, S Hudziak, H Howe, C Labbe, R Rizk, M Pepper, and A Kenyon. Quantum conductance in silicon oxide resistive memory devices. *Scientific reports*, 3(1):1–8, 2013.

[39] D Ielmini and R Waser. *Resistive switching: from fundamentals of nanoionic redox processes to memristive device applications*. John Wiley & Sons, 2015.

[40] H Ju and M Yang. Duality characteristics of bipolar and unipolar resistive switching in a Pt/$SrZrO_3$/TiO_x/Pt stack. *AIP Advances*, 10(6):065221, 2020.

[41] Y Bai, H Wu, Y Zhang, M Wu, J Zhang, N Deng, H Qian, and Z Yu. Low power W: AlO_x/WO_x bilayer resistive switching structure based on conductive filament formation and rupture mechanism. *Applied Physics Letters*, 102(17):173503, 2013.

[42] S Gao, G Liu, Q Chen, W Xue, H Yang, J Shang, B Chen, F Zeng, C Song, and F Pan. Improving unipolar resistive switching uniformity with cone-shaped conducting filaments and its logic-in-memory application. *ACS applied materials & interfaces*, 10(7):6453–6462, 2018.

[43] Y Tokunaga, Y Kaneko, JP He, T Arima, A Sawa, T Fujii, M Kawasaki, and Y Tokura. Colossal electroresistance effect at metal electrode/$La_{1-x}Sr_{1+x}MnO_4$ interfaces. *Applied Physics Letters*, 88:223507, 2006.

[44] S G Choi, H S Lee, H Choi, S W Chung, and H Park. The effect of Sr concentration on resistive switching properties of $La_{1-x}Sr_xMnO_3$ films. *Thin Solid Films*, 529:352–355, 2013.

[45] S Wang and T Tseng. Interface engineering in resistive switching memories. *Journal of Advanced Dielectrics*, 1(02):141–162, 2011.

[46] Wikimedia Commons. Crystal structure of the mineral perovskite (calcium titanate, $CaTiO_3$; orthorhombic, space group Pbmn), 2012. URL `https://commons.wikimedia.org/wiki/File:CaTiO3_perovskite_structure.png`.

[47] T Elovaara, H Huhtinen, S Majumdar, and P Paturi. Irreversible metamagnetic transition and magnetic memory in small-bandwidth manganite $Pr_{1-x}Ca_xMnO_3$ ($x = 0.0 - 0.5$). *Journal of Physics: Condensed Matter*, 24(21):216002, 2012.

[48] K Xu and H Xiang. Unusual ferroelectricity induced by the Jahn-Teller effect: A case study on lacunar spinel compounds. *Physical Review B*, 92(12):121112, 2015.

[49] N Mott. *Metal-insulator transitions*. CRC Press, 2004.

[50] M Aye, E Rivasto, M Khan, H Rijckaert, E Salojärvi, C Haalisto, E Mäkilä, H Palonen, H Huhtinen, and I Van Driessche. Control of the nanosized defect network in superconducting thin films by target grain size. *Scientific reports*, 11(1):1–11, 2021.

[51] T Elovaara, S Majumdar, H Huhtinen, and P Paturi. Photoinduced colossal magnetoresistance under substantially reduced magnetic field. *Advanced Functional Materials*, 25:5030–5037, 2015.

[52] E Katz. Perovskite: name puzzle and German-Russian odyssey of discovery. *Helvetica Chimica Acta*, 103(6):e2000061, 2020.

[53] V Goldschmidt. Die gesetze der krystallochemie. *Naturwissenschaften*, 14(21):477–485, 1926.

[54] F Allard, P Hauschildt, D Alexander, A Tamanai, and A Schweitzer. The limiting effects of dust in brown dwarf model atmospheres. *The Astrophysical Journal*, 556(1):357, 2001.

[55] H Snaith. Present status and future prospects of perovskite photovoltaics. *Nature materials*, 17(5):372–376, 2018.

[56] A Herklotz, A Wong, T Meyer, M Biegalski, H Lee, and T Ward. Controlling octahedral rotations in a perovskite via strain doping. *Scientific reports*, 6(1):1–7, 2016.

[57] K Kugel and D Khomski. The Jahn-Teller effect and magnetism: transition metal compounds. *Soviet Physics Uspekhi*, 25(4):231, 1982.

[58] Y Gao, J Wang, L Wu, S Bao, Y Shen, Y Lin, and C Nan. Tunable magnetic and electrical behaviors in perovskite oxides by oxygen octahedral tilting. *Science China Materials*, 58(4): 302–312, 2015.

[59] C Bartel, C Sutton, B Goldsmith, R Ouyang, C Musgrave, L Ghiringhelli, and M Scheffler. New tolerance factor to predict the stability of perovskite oxides and halides. *Science advances*, 5(2):eaav0693, 2019.

[60] Z Li, M Yang, J Park, S Wei, J Berry, and K Zhu. Stabilizing perovskite structures by tuning tolerance factor: formation of formamidinium and cesium lead iodide solid-state alloys. *Chemistry of Materials*, 28(1):284–292, 2016.

[61] S Majumdar, H Huhtinen, P Paturi, and R Palai. The effect of oxygen on the Jahn–Teller distortion and magnetization dynamics of $Pr_{0.9}Ca_{0.1}MnO_3$ thin films. *Journal of Physics: Condensed Matter*, 25(6):066005, 2013.

[62] J Tikkanen et al. Praseodymium calcium manganites: Magnetism across length scales. 2017.

[63] Z Jirak, S Krupička, Z Šimša, M Dlouha, and S Vratislav. Neutron diffraction study of $Pr_{1-x}Ca_xMnO_3$ perovskites. *Journal of magnetism and magnetic materials*, 53(1-2):153–166, 1985.

[64] E Dagotto, T Hotta, and A Moreo. Colossal magnetoresistant materials: the key role of phase separation. *Physics reports*, 344(1-3):1–153, 2001.

[65] E Dagotto. *Nanoscale phase separation and colossal magnetoresistance: the physics of manganites and related compounds*. Springer Science & Business Media, 2003.

[66] T Elovaara et al. Magnetophotoresistance in $Pr_{1-x}Ca_xMnO_3$ thin films. 2016.

[67] A Beiranvand, J Tikkanen, H Huhtinen, and P Paturi. Metamagnetic transition and spin memory effect in epitaxial $Gd_{1-x}Ca_xMnO_3$ (0<x<1) thin films. *Journal of Magnetism and Magnetic Materials*, 469:253–258, 2019.

[68] A Beiranvand, J Tikkanen, H Huhtinen, and P Paturi. Electronic and magnetic phase diagram of polycrystalline $Gd_{1-x}Ca_xMnO_3$ manganites. *Journal of Alloys and Compounds*, 720: 126–130, 2017.

[69] F Chiu. A review on conduction mechanisms in dielectric films. *Advances in Materials Science and Engineering*, 2014:578168, 2014.

[70] T Nakayama, Y Kangawa, and K Shiraishi. Atomic structures and electronic properties of semiconductor interfaces. *Comprehensive Semiconductor Science and Technology*, page 113, 2011.

[71] S Lashkare, S Chouhan, T Chavan, A Bhat, P Kumbhare, and U Ganguly. PCMO RRAM for integrate-and-fire neuron in spiking neural networks. *IEEE Electron Device Letters*, 39: 484–487, 2018.

[72] S Bagdzevicius, K Maas, M Boudard, and M Burriel. Interface-type resistive switching in perovskite materials. *Journal of Electroceramics*, 39:157–184, 2017.

[73] N Kanegami, Y Nishi, and T Kimoto. Unique resistive switching phenomena exhibiting both filament-type and interface-type switching in Ti/$Pr_{0.7}Ca_{0.3}MnO_{3-\delta}$/Pt ReRAM cells. *Applied Physics Letters*, 116:013501, 2020.

[74] S Park, H Kim, M Choo, J Noh, A Sheri, S Jung, K Seo, J Park, S Kim, W Lee, J Shin, Lee D, G Choi, J Woo, E Cha, J Jang, C Park, M Jeon, B Lee, B H Lee, and H Hwang. RRAM-based synapse for neuromorphic system with pattern recognition function. In *2012 international electron devices meeting*, pages 10–2. IEEE, 2012.

[75] S Park, A Sheri, J Kim, J Noh, J Jang, M Jeon, B Lee, BR Lee, BH Lee, and H-J Hwang. Neuromorphic speech systems using advanced reram-based synapse. In *2013 IEEE IEDM*, pages 25–6. IEEE, 2013.

[76] E Miranda, W Román Acevedo, D Rubi, U Lüders, P Granell, J Suñé, and P Levy. Modeling of the multilevel conduction characteristics and fatigue profile of Ag/$La_{1/3}Ca_{2/3}MnO_3$/Pt structures using a compact memristive approach. *Journal of Applied Physics*, 121:205302, 2017.

[77] R Ortega-Hernandez, M Coll, J Gonzalez-Rosillo, A Palau, X Obradors, E Miranda, T Puig, and J Sune. Resistive switching in CeO_2/$La_{0.8}Sr_{0.2}MnO_3$ bilayer for non-volatile memory applications. *Microelectronics Engineering*, 147:37–40, 2015.

[78] J W Jang, S Park, G W Burr, H Hwang, and Y H Jeong. Optimization of conductance change in $Pr_{1-x}Ca_xMnO_3$-based synaptic devices for neuromorphic systems. *IEEE Electron Device Letters*, 36:457–459, 2015.

[79] M Zhao, B Gao, J Tang, H Qian, and H Wu. Reliability of analog resistive switching memory for neuromorphic computing. *Applied Physics Reviews*, 7:011301, 2020.

[80] R Waser, R Dittmann, G Staikov, and K Szot. Redox-based resistive switching memories–nanoionic mechanisms, prospects, and challenges. *Advanced Materials*, 21:2632–2663, 2009.

[81] D Lee, J Park, K Moon, J Jang, S Park, M Chu, J Kim, J Noh, M Jeon, B Lee, B Lee, Hwang H, and B Lee. Oxide based nanoscale analog synapse device for neural signal recognition system. In *2015 IEEE International Electron Device Meeting*, pages 4–7. IEEE, 2015.

[82] Z Liao, Z Wang, Y Meng, Z Liu, P Gao, J Gang, H Zhao, X Liang, X Bai, and D Chen. Categorization of resistive switching of metal-$Pr_{0.7}Ca_{0.3}MnO_3$-metal devices. *Applied Physics Letters*, 94:253503, 2009.

[83] R Yang, X M Li, W D Yu, X J Liu, X Cao, Q Wang, and L D Chen. Multiform resistance switching effects in the Al/$La_{0.7}Ca_{0.3}MnO_3$/Pt structure. *Electrochemical and Solid State Letters*, 12:H281–H283, 2009.

[84] DJ Seong, M Hassan, H Choi, J Lee, J Yoon, JB Park, W Lee, MS Oh, and H Hwang. Resistive-switching characteristics of Al/$Pr_{0.7}Ca_{0.3}MnO_3$ for nonvolatile memory applications. *IEEE Electron Device Letters*, 30:919–921, 2009.

[85] T Nakamura, K Homma, and K Tachibana. Thin film deposition of metal oxides in resistance switching devices: Electrode material dependence of resistance switching in manganite films. *Nanoscale Research Letters*, 8:76, 2013.

[86] D Joksas and A Mehonic. badcrossbar: A python tool for computing and plotting currents and voltages in passive crossbar arrays. *SoftwareX*, 12:100617, 2020.

[87] Y Yang, P Sheridan, and W Lu. Complementary resistive switching in tantalum oxide-based resistive memory devices. *Applied Physics Letters*, 100(20):203112, 2012.

[88] H Li, S Wang, X Zhang, W Wang, R Yang, Z Sun, W Feng, P Lin, Z Wang, L Sun, et al. Memristive crossbar arrays for storage and computing applications. *Advanced Intelligent Systems*, 3(9):2100017, 2021.

[89] F Gul. Addressing the sneak-path problem in crossbar RRAM devices using memristor-based one Schottky diode-one resistor array. *Results in Physics*, 12:1091–1096, 2019.

[90] G Burr, R Shelby, A Sebastian, S Kim, S Kim, S Sidler, K Virwani, M Ishii, P Narayanan, and A Fumarola. Neuromorphic computing using non-volatile memory. *Advances in Physics: X*, 2(1):89–124, 2017.

[91] C Li, M Hu, Y Li, H Jiang, N Ge, E Montgomery, J Zhang, W Song, N Dávila, C E Graves, Z Li, J P Strachan, P Lin, Z Wang, M Barnell, Q Wu, R S Williams, J J Yang, and Q Xia. Analogue signal and image processing with large memristor crossbars. *Nature Electronics*, 1:52, 2018.

[92] P Yao, H Wu, B Gao, J Tang, Q Zhang, W Zhang, J J Yang, and H Qian. Fully hardware-implemented memristor convolutional neural network. *Nature*, 577:641–646, 2020.

[93] L Gao, P Chen, and S Yu. Demonstration of convolution kernel operation on resistive cross-point array. *IEEE Electron Device Letters*, 37:870–873, 2016.

[94] Z Du, K Palem, A Lingamneni, O Temam, Y Chen, and C Wu. Leveraging the error resilience of machine-learning applications for designing highly energy efficient accelerators. In *2014 19th Asia and South Pacific design automation conference (ASP-DAC)*, pages 201–206. IEEE, 2014.

[95] P Stoliar, J Tranchant, B Corraze, E Janod, M Besland, F Tesler, M Rozenberg, and L Cario. A leaky-integrate-and-fire neuron analog realized with a Mott insulator. *Advances in Functional Materials*, 27:1604740, 2017.

[96] Y Pan, T Wan, H Du, B Qu, D Wang, T Ha, and D Chu. Mimicking synaptic plasticity and learning behaviours in solution processed SnO_2 memristor. *Journal of Alloys and Compounds*, 757:496–503, 2018.

[97] C Adda, J Tranchant, P Stoliar, B Corraze, E Janod, R Gay, R Llopis, M Besland, L. E Hueso, and L. Cario. An artificial neuron founded on resistive switching of Mott insulators. *2017 IEEE International Memory Workshop (IMW)*, pages 1–4, 2017.

[98] K Moon, A Fumarola, S Sidler, J Jang, P Narayanan, R Shelby, G Burr, and H Hwang. Bidirectional non–filamentary RRAM as an analog neuromorphic synapse, Part I: Al/Mo/$Pr_{0.7}Ca_{0.3}MnO_3$ material improvements and device measurements. *IEEE Journal of the Electron Devices Society*, 6:146–155, 2018.

[99] N Panwar and U Ganguly. Variability assessment and mitigation by predictive programming in $Pr_{0.7}Ca_{0.3}MnO_3$ based RRAM. *IEEE 2015 73rd Annual Device Research Conference (DRC)*, pages 141–142, 2015.

[100] Z Wang, S Joshi, S Savel'ev, W Song, R Midya, Y Li, M Rao, P Yan, S Asapu, Y Zhuo, et al. Fully memristive neural networks for pattern classification with unsupervised learning. *National Electronics*, 1:137, 2018.

[101] D Jeong and C Hwang. Nonvolatile memory materials for neuromorphic intelligent machines. *Advanced Materials*, 30:1704729, 2018.

[102] S Yu. *Neuro-inspired Computing Using Resistive Synaptic Devices*. Springer International Publishing, 2017. ISBN 978-3-319-54312-3.

[103] C Acha, M Barella, G Sanca, F Marlasca, H Huhtinen, P Paturi, P Levy, and F Golmar. YBCO-based non-volatile ReRAM tested in low earth orbit. *Journal of Materials Science: Materials in Electronics*, 31(19):16389–16397, 2020.

[104] H Jiang, D Belkin, S Savel'ev, S Lin, Z Wang, Y Li, S Joshi, R Midya, C Li, and M Rao. A novel true random number generator based on a stochastic diffusive memristor. *Nature communications*, 8(1):1–9, 2017.

[105] M Aye, E Rivasto, M Khan, H Rijckaert, H Palonen, H Huhtinen, I Van Driessche, and P Paturi. Multilayering BZO nanocolumns with different defect densities for YBCO high field applications. *New Journal of Physics*, 23(11):113031, 2021.

[106] S Swann. Magnetron sputtering. *Physics in technology*, 19(2):67, 1988.

[107] H Zabel. X-ray and neutron reflectivity analysis of thin films and superlattices. *Applied physics A*, 58(3):159–168, 1994.

[108] H Voorma, E Louis, N Koster, F Bijkerk, and E Spiller. Characterization of multilayers by Fourier analysis of x-ray reflectivity. *Journal of applied physics*, 81(9):6112–6119, 1997.

[109] K Tsubouchi, I Ohkubo, H Kumigashira, M Oshima, Y Matsumoto, K Itaka, T Ohnishi, M Lippmaa, and H Koinuma. High-throughput characterization of metal electrode performance for electric-field-induced resistance switching in metal/$Pr_{0.7}Ca_{0.3}MnO_3$/metal structures. *Advanced Materials*, 19:1711–1713, 2007.

[110] P Paturi, J Tikkanen, and H Huhtinen. Room temperature charge-ordered phase in $Gd_{0.6}Ca_{0.4}MnO_3$ and $Sm_{0.6}Ca_{0.4}MnO_3$ thin films. *Journal of Magnetism and Magnetic Materials*, 432:164–168, 2017.

[111] M Nyman, T Elovaara, J Tikkanen, S Majumdar, H Huhtinen, and P Paturi. Epitaxially textured $Pr_{0.6}Ca_{0.4}MnO_3$ thin films under considerably low substrate temperature. *Physics Procedia*, 75:1122–1132, 2015.

[112] D Reagor, S Lee, Y Li, and Q Jia. Work function of the mixed-valent manganese perovskites. *Journal of Applied Physics*, 95:7971–7975, 2004.

[113] D Lide. *CRC Handbook of Chemistry and Physics*. CRC Press I, LLC, 2009.

[114] K Baek, S Park, J Park, Y Kim, H Hwang, and S Oh. In situ tem observation on the interface-type resistive switching by electrochemical redox reactions at a TiN/PCMO interface. *Nanoscale*, 9:582–593, 2017.

[115] SL Li, J Li, Y Zhang, DN Zheng, and K Tsukagoshi. Unipolar resistive switching in high-resistivity $Pr_{0.7}Ca_{0.3}MnO_3$ junctions. *Applied Physics A*, 103:21–26, 2011.

[116] M A Zidan, H Fahmy, M Hussain, and K Salama. Memristor-based memory: The sneak paths problem and solutions. *Microelectronics Journal*, 44:176–183, 2013.

[117] F Gomez-Marlasca, N Ghenzi, P Stoliar, M Sánchez, M Rozenberg, G Leyva, and P Levy. Asymmetric pulsing for reliable operation of titanium/manganite memristors. *Applied Physics Letters*, 98:123502, 2011.

[118] P Stoliar, Pablo Levy, MJ Sánchez, AG Leyva, CA Albornoz, F Gomez-Marlasca, A Zanini, C Toro Salazar, N Ghenzi, and MJ Rozenberg. Nonvolatile multilevel resistive switching memory cell: A transition metal oxide-based circuit. *IEEE Transactions on Circuits and Systems II: Express Briefs*, 61:21–25, 2014.

[119] E Miranda and J Suñé. Memristive state equation for bipolar resistive switching devices based on a dynamic balance model and its equivalent circuit representation. *IEEE Transactions on Nanotechnology*, 19:837–840, 2020.

[120] C Acha. Graphical analysis of current-voltage characteristics in memristive interfaces. *Journal of Applied Physics*, 121:134502, 2017.

[121] A Zabrodskii. The coulomb gap: the view of an experimenter. *Philosophical Magazine B*, 81 (9):1131–1151, 2001.

[122] W Lau. An extended unified Schottky-Poole-Frenkel theory to explain the current-voltage characteristics of thin film metal-insulator-metal capacitors with examples for various high-k dielectric materials. *ECS Journal of Solid State Science and Technology*, 1:N139, 2012.

[123] A Sawa, T Fujii, M Kawasaki, and Y Tokura. Interface transport properties and resistance switching in perovskite-oxide heterojunctions. *SPIE Conference Proceedings*, 5932:59322C, 2005.

[124] C Acha, A Schulman, M Boudard, K Daoudi, and T Tsuchiya. Transport mechanism through metal-cobaltite interfaces. *Applied Physics Letters*, 109:011603, 2016.

[125] E Miranda. Compact model for the major and minor hysteretic I-V loops in nonlinear memristive devices. *IEEE Transactions on Nanotechnology*, 14(5):787–789, 2015.

[126] T Prodromakis, B Peh, C Papavassiliou, and C Toumazou. A versatile memristor model with nonlinear dopant kinetics. *IEEE transactions on electron devices*, 58(9):3099–3105, 2011.

[127] A Isah, A Nguetcho, S Binczak, and J Bilbault. Comparison of the performance of the memristor models in 2D cellular nonlinear network. *Electronics*, 10(13):1577, 2021.

[128] M Krasnosel'skii and A Pokrovskii. *Systems with hysteresis*. Springer Science & Business Media, 2012.

[129] J Takács. Mathematics of hysteretic phenomena, 2003 Wiley.

[130] Rui Yang, XM Li, WD Yu, XD Gao, XJ Liu, Xun Cao, Qun Wang, and LD Chen. Stable bipolar resistance switching behaviour induced by a soft breakdown process at the Al/$La_{0.7}Ca_{0.3}MnO_3$ interface. *Journal of Physics D: Applied Physics*, 42(17):175408, 2009.

[131] E Miranda, J Suñé, R Rodriguez, M Nafria, X Aymerich, L Fonseca, and F Campabadal. Soft breakdown conduction in ultrathin (3-5 nm) gate dielectrics. *IEEE Transactions on Electron Devices*, 47(1):82–89, 2000.

[132] G Cellere, L Larcher, M Valentini, and A Paccagnella. Micro breakdown in small-area ultrathin gate oxides. *IEEE Transactions on Electron Devices*, 49(8):1367–1374, 2002.

[133] S Ghosh-Dastidar and H Adeli. Spiking neural networks. *International journal of neural systems*, 19(04):295–308, 2009.

[134] P Diehl and M Cook. Unsupervised learning of digit recognition using spike-timing-dependent plasticity. *Frontiers in computational neuroscience*, 9:99, 2015.

[135] A Thomas. Memristor-based neural networks. *Journal of Physics D: Applied Physics*, 46(9): 093001, 2013.

[136] T Hynnä. Optimizing synaptic properties of $Gd_{1-x}Ca_xMnO_3$ memristor devices. *University of Turku, Master's thesis*, 2022.

Original Publications

V. Lähteenlahti & A. Schulman & H. Huhtinen & P. Paturi

Transport Properties of Resistive Switching in $Ag/Pr_{0.6}Ca_{0.4}MnO_3/Al$ Thin Film Structures

Journal of Alloys and Compounds, 786, 2019, 84–90

I

Journal of Alloys and Compounds 786 (2019) 84–90

Contents lists available at ScienceDirect

Journal of Alloys and Compounds

journal homepage: http://www.elsevier.com/locate/jalcom

Transport properties of resistive switching in Ag/$Pr_{0.6}Ca_{0.4}MnO_3$/Al thin film structures

V. Lähteenlahti*, A. Schulman, H. Huhtinen, P. Paturi

Wihuri Physical Laboratory, Department of Physics and Astronomy, University of Turku, FI-20014 Turku, Finland

A R T I C L E I N F O

Article history:
Received 10 October 2018
Received in revised form
21 January 2019
Accepted 24 January 2019
Available online 30 January 2019

Keywords:
Resistive switching
Perovskite oxides
Switching mechanics
PCMO
Memristor
Neuromorphic

A B S T R A C T

Thin films of $Pr_{0.6}Ca_{0.4}MnO_3$ were prepared by pulsed laser deposition with an asymmetric pair of Ag and Al metal electrodes in order to study their resistive switching properties. The devices exhibited stable voltage controlled bipolar switching which proved to be reliable and non-volatile. The resistive states show a well-defined dependence on the write voltage, which was used to achieve several intermediate states, indicating that the devices could be utilized in hardware implementations of neuromorphic computing. The switching mechanism was attributed to the electric-field assisted migration of oxygen vacancies at the Al-electrode interface, resulting in a formation and modulation of a rectifying interfacial AlO_x layer. The current-voltage characteristics were analyzed by means of the power exponent representation, which hinted to a device state dependent interplay of bulk-limited Poole-Frenkel conduction and interface-limited Schottky conduction. A deeper understanding of resistive switching characteristics in Ag/$Pr_{0.6}Ca_{0.4}MnO_3$/Al will lead towards further advances in manganite-based neuromorphic circuits.

© 2019 The Authors. Published by Elsevier B.V. This is an open access article under the CC BY license (http://creativecommons.org/licenses/by/4.0/).

1. Introduction

Present day's computers suffer from the von Neumann bottleneck, in which the processing speed is limited by the bus which connects memory and the central processing unit [1]. Neuromorphic computer architectures show a possible way to bypass this limit since they do not divide memory and computations into separate units, which enables highly parallel computations [2–4]. In possible hardware implementations of neuromorphic computing, devices that behave more similarly to biological synapses and neurons are preferable over the traditional CMOS (complementary metal-oxide-semiconductor) solutions, which are not efficient for these tasks since the technology was designed for a different purpose [5,6].

The implementation of these new technologies will require the utilization of new and more efficient materials. In particular, metal oxides, which have gained a lot of attention for their rich chemical and physical properties and versatile applicability in many areas, such as energy storage, solar cells and sensors [7–14]. Metal oxides have also found their place in resistive switching (RS) devices [15,16]. Due to the RS property present in many metal oxides, they now present a notable portion of promising memristive materials [17].

Oxide based resistive switching devices are suitable for mimicking neurons and storing synaptic weights [18–23]. Indeed, neuromorphic circuits containing RS elements are starting to show promising results, particularly in the field of spiking neural networks, where the RS oxide can reproduce dynamics found in biological systems with minimal amount of additional circuitry [24]. However, more research is still needed to understand the physics behind the RS in order to maximize the capabilities of these systems [25,26].

Among the oxides which present the RS behavior, the perovskite oxide $Pr_{1-x}Ca_xMnO_3$ has been proven to be versatile, exhibiting both bipolar [22] and unipolar [27] switching with and without forming [28,29]. The interface-type bipolar switching in particular has been found useful in neuromorphic applications, which has led to PCMO-based implementations of single neurons as well as neuromorphic arrays [26,30–32].

Even though the RS in $Pr_{1-x}Ca_xMnO_3$ has been extensively studied [17,28,29,33–38], new ways to improve the switching properties are still being found by the means of interface engineering with buffer layers and oxygen treatments [22,39]. In addition, the core of the work on RS in PCMO has been performed with $x = 0.3$, although it has been shown that other concentrations can result in better RS properties [36]. The conduction model of

* Corresponding author.
E-mail address: visalah@utu.fi (V. Lähteenlahti).

https://doi.org/10.1016/j.jallcom.2019.01.279
0925-8388/© 2019 The Authors. Published by Elsevier B.V. This is an open access article under the CC BY license (http://creativecommons.org/licenses/by/4.0/).

bipolar switching has also been usually attributed to the trap-controlled space-charge-limited current (SCLC) conduction [33,38,40–44] with exponentially distributed traps, although the use of a more in depth analysis method [45] gives an alternative explanation. Thus improving the understanding of RS and conduction mechanisms in PCMO is still possible and a remains as a path towards realization of more robust neuromorphic devices.

In this work we studied the RS characteristics of $Pr_{1-x}Ca_xMnO_3$ with an optimal concentration of $x = 0.4$, hereafter labeled PCMO. In PCMO, the bipolar switching is determined by the interfaces [28]. Due to this, we studied the interface properties of Metal/PCMO/Metal structures with different metallic electrode combinations. The utilized metals were Ag, Au and Al, of which we found that only the Al interface produces a strong bipolar RS effect. The switching attained by using Al/PCMO/Ag interfaces exhibits multiple states and was both reliable and non-volatile. The cause of the switching is attributed to oxygen vacancy migration at the Al/PCMO interface. The conduction model is analyzed, hinting to an interplay of bulk-limited PF conduction and interface-limited Schottky conduction depending on the device state and polarity of the electric field.

2. Experimental details

$Pr_{0.6}Ca_{0.4}MnO_3$ thin films with thicknesses of approximately 100 nm were deposited on $5 \times 5 \times 0.5$ mm^3 (100) $SrTiO_3$ substrates by pulsed laser deposition (PLD) using excimer XeCl 308 nm laser. The pulse duration was 25 ns, repetition rate 5 Hz, laser fluence 1.3 J/cm^2 and the pressure of flowing oxygen in the chamber 0.175 torr. The films were grown at a temperature of 500 °C, with *in situ* post-annealing treatment of 10 min in atmospheric oxygen pressure. The used rate for cooling and heating was 25 °C/min. The grown films were verified to be well-crystallized and epitaxially textured by X-ray diffraction (Fig. 1a) with lattice parameters $a = 5.4354$ Å, $b = 7.6511$ Å and $c = 5.4277$ Å. More details on the growth process can be found in Ref. [46].

0.5 mm diameter Au and Ag metal contacts were deposited on top of the films using room-temperature Ar-ion sputtering. Wiring was done with a wedge bonder using a 40 μm diameter Al-wire. Measurements were performed in a planar configuration as schematized in the inset of Fig. 1c using a Keithley 2614b source/measure unit. The separation distance between the electrodes was approximately 200 μm.

Loop measurements of electrical characteristics were done at room temperature by sweeping the voltage in a sequence of steps $0 \rightarrow V_{max} \rightarrow -V_{min} \rightarrow 0$ with logarithmic amplitude progression, 10 ms step width and a 10 ms low-voltage read between each step. Multiple films were studied, and the characteristics were found to be consistent between the samples.

All combinations of Al, Ag and Au Metal/PCMO/Metal interfaces were measured, and only combinations containing Al were found to produce switching. Both Ag and Au interfaces formed a linear Ohmic contact with PCMO (Fig. 1b), and thus didn't contribute to the switching. When Al interface was present, the conduction was non-linear.

Since the work function of p-type [36] $Pr_{0.6}Ca_{0.4}MnO_3$ is close to values reported for other concentrations: $\phi \approx 4.9$ eV [47] for $x = 0.3$ and $\phi \approx 4.8$ eV for $x = 0.5$ [36], a more rectifying interface is expected for the Al ($\phi = 4.06$–4.26 eV [48]) than for the Ag ($\phi = 4.26$–4.47 eV [48]) due to the differences in work functions, which is in agreement with the measurements (Fig. 1b).

In the case of Al/PCMO/Al, the conduction reproduced the “table-with-legs” profile (Fig. 1b), which has previously been obtained by simulating dielectric with a changing oxygen vacancy profile between two electrodes [49]. The presence of the table-with-legs shape indicates that both of the Al interfaces are active in switching, and introducing asymmetry in the electrodes will enhance the bipolar switching properties.

When asymmetry was introduced into the electrodes by using Au/PCMO/Al or Ag/PCMO/Al (Fig. 1b) the RS properties were greatly increased as predicted by the simulations. Thus we selected the combination of rectifying Al and Ohmic Ag interfaces for further studies. The combination ensures us that the RS is dominated by the Al/PCMO interface and only one of the two interfaces is active in switching.

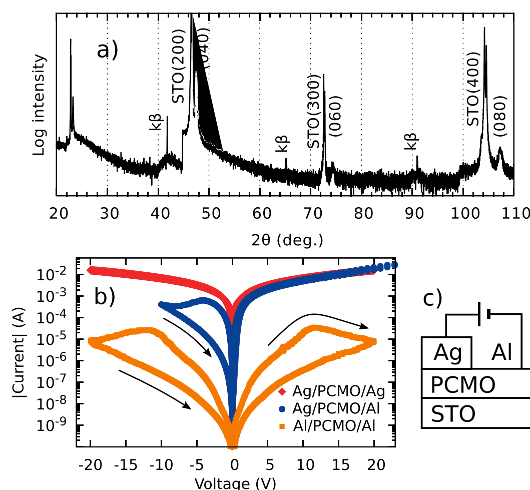

Fig. 1. a) XRD diffractogram of (lkl) peaks. b) I-V loops for PCMO with combinations of Ag and Al interfaces, symmetrical Ag-interfaces show Ohmic conduction, while interfaces containing Al show non-linear conduction and rectifying behavior. c) Measurement geometry.

3. Results and discussion

3.1. Bistable switching

A typical example of a stable bipolar switching is presented in Fig. 2. The device can be switched between HRS (high resistance state) and LRS (low resistance state) in a closed loop by applying positive and negative voltage sweeps. Negative polarity induces the

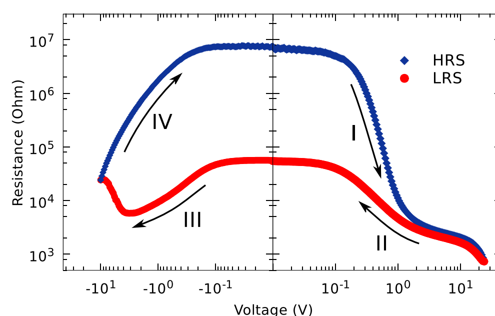

Fig. 2. A single bipolar switching loop showing device resistance as a function of applied voltage. Positive polarity induces the LRS while the negative polarity resets device into the HRS.

transition to HRS and positive to LRS. The resistance of a pristine device is initially between the HRS and LRS resistances and doesn't need electroforming in the conventional sense, although the first loops show irregular step changes. Similar forming-free behavior has been observed for both bipolar and unipolar switching in PCMO and has been found to be affected by both electrode materials and growth conditions [28,29]. As there is no high-voltage forming process or current limitation involved, the device homogeneity is good and the devices show predictable behavior with similar resistance values across different samples. The HRS and LRS voltages were chosen to obtain a reasonable compromise between a high switching ratio and reliability. The voltages needed for switching could be further reduced by miniaturizing the device dimensions. It is worth noting that no switching is observed if the applied voltage is below certain threshold which for our geometry is $V_{th} = 3$ V. This is of great importance since neuromorphic devices require a possibility of non-destructive reading of the resistive state.

We didn't notice any variation in the behavior of the devices when changing the electrode separation distance, indicating that the dominant switching effect is not caused by filamentary conduction paths. The measurements rule out the involvement of Ag-ions, as well as intrinsic switching PCMO bulk, since it has been shown that the bulk PCMO switches with unipolar behavior [29]. This leaves oxygen vacancy movement near the interface region as the main culprit for changes in conductivity.

Within the generally accepted framework for the origin of the RS in oxides [27,36,49–52], the bipolar switching is attributed to the electric field assisted migration of oxygen vacancies [49] near the Al/PCMO interface. Due to differences in the oxidation energies when the devices are in the pristine state, an oxide layer is formed at the interface, generating a Schottky-like barrier [35].

Passing a current through the device produces a large electric field at the interface due to the high resistivity of the barrier. The electric field enables movement of oxygen vacancies towards or away from the interface, which modulates the oxide layer thickness, resulting in either lowered or increased conductivity across the entire device. The process is reversed by applying an opposite voltage which causes migration of mobile oxygen vacancies to the opposite direction. The effect is limited to the interface due to the lower electric field inside the bulk. In addition, electric transport inside the PCMO bulk is a result of double-exchange interaction, which relies on oxygen atoms, thus introducing more oxygen vacancies decreases the conductivity [53]. Aluminum oxide formation at metal-manganite interfaces has been observed experimentally and changes depending on the RS state [37,54,55].

3.2. Conduction mechanism

In order to better understand the physical origin of the RS, we need to study the conduction mechanism in more detail. For this, we utilize the power exponent representation [45] which allows for a more in-depth determination of the dominant conduction mechanism than the commonly used method where power exponents are obtained by fitting to manually selected regions of interest. The analysis considers a quantity $\gamma = d(\ln(|I|))/d(\ln(|V|))$ for the whole voltage range, giving power exponents for all the datapoints. Different non-linear (NL) elements [56] produce distinct γ to |V| dependencies, which can be used to differentiate between conduction models. For example, an Ohmic junction ($I \propto V$) will result in a constant $\gamma = 1$, while a SCLC ($I \propto V^2$) dominated interface will have a constant of $\gamma = 2$. Conduction mechanisms that have an exponential dependence between current and voltage, such as Poole-Frenkel (PF) and Schottky, will present a straight line which

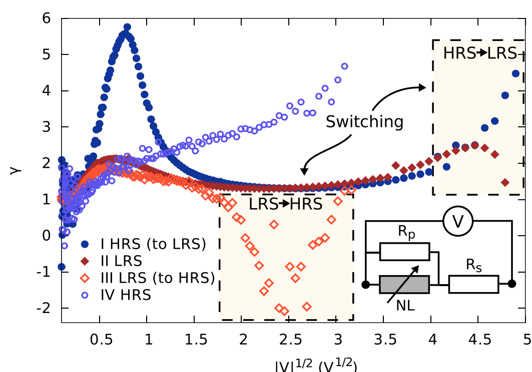

Fig. 3. A $\gamma(V)$ plot where $\gamma = d(\ln(|I|))/d(\ln(|V|))$, showing the power exponent at each point of the bipolar switching loop of Fig. 2 with the same correspondence between the curves I-IV. The inset shows an equivalent circuit for the system, consisting of a non-linear element (NL) with parallel and series resistances R_p and R_s.

will only differ in the y-intercept value (0 for Schottky and 1 for PF).

The analysis of the IV characteristics for both the HRS and LRS is presented in Fig. 3. Starting the loop in the HRS and at the positive polarity (curve I) we can distinguish 3 main regions. At low voltages there is a clear Ohmic behavior where γ is 1. At intermediate voltages (200 mV–3 V) there is a peak with a maximum exponent of 6 and then a stabilization to an exponent between 1 and 2. Switching towards the LRS begins at a voltage of around 12 V. Once in the LRS (curve II) the situation is fairly similar, but the peak is less pronounced, with a maximum of 2. The LRS at the negative polarity (curve III) mirrors the positive polarity LRS dependence until the switching to HRS begins at a voltage of 3 V. After the switch from LRS to HRS, the conduction mechanism of the negative polarity changes (curve IV) and the curve resembles a line with an intercept value between 0 and 1.

It is clear that LRS and HRS have different characteristics. On one hand the LRS is symmetrical indicating a bulk-dominated conduction mechanism. On the other hand, the HRS presents rectifying behavior and shows a linear γ-dependence in the curve IV, suggesting that a Schottky-like barrier is dominant in this state. To properly explain the peak shape of $\gamma(V)$, a more complex circuit needs to be introduced. For this we consider an equivalent circuit (Fig. 3) consisting of a switching non-linear element (NL) with Ohmic series and parallel resistances R_s and R_p. The non-linear element (NL) representing the contribution of the Al/PCMO interface can be thought as a bulk-limited PF conduction in series with a Schottky diode [57]. The series resistance R_s represents the contribution from the oxide layer and the parallel resistance R_p the contribution from regions of the interface which do not contribute to the switching.

The resistive switching influences the AlO_x layer, which translates into changing the Schottky barrier of the NL-element [58] and determines whether or not it has a significant contribution to the total conductivity. In the LRS the barrier is thinner and the amount of rectification is reduced. Conversely, in the HRS the barrier is thicker and the interface becomes rectifying. When the NL element is forward biased the PF contribution dominates over the Schottky mechanism and while in the reverse bias the dominating mechanism can be either Schottky or PF depending on the RS state.

Indeed, in the real device the forward biased HRS curve I and both of the LRS state curves II and III have a distinct shape which corresponds to a PF conduction with Ohmic series and parallel resistances R_s and R_p (Fig. 3) and the reverse biased HRS curve IV

resembles rectifying Schottky conduction. Out of the PF-shaped curves the HRS has a higher maximum exponent than the LRS. In terms of the equivalent circuit, this means that in the HRS the ratio of non-linear resistance to parallel resistance R_p is higher, thus we can determine HRS and LRS solely from the $\gamma(V)$ curve shape [45].

3.2.1. Conduction model fitting

By considering a model consisting of a PF-element with series and parallel resistances R_s and R_p we can form an implicit equation for I and V:

$$I = A(V - I \cdot R_s)\left[\exp\left(B\sqrt{V - I \cdot R_s}\right)\right] + \frac{V - I \cdot R_s}{R_p}, \quad (1)$$

with $A = \tilde{A}_{PF}\exp\left(-\frac{q\phi_B}{k_B T}\right)$, $B = \frac{q^{3/2}}{k_B T(\pi\varepsilon_0\varepsilon' d)^{1/2}}$, where T is the temperature, $\tilde{A}_{PF}$ is a constant, q the electron charge, ϕ_B the trap energy level, k_B the Bolzmann constant, ε_0 the vacuum permittivity, ε' the real part of the dielectric constant, d the distance where the voltage drop is produced, R_s the series resistance and R_p the parallel resistance [45].

Table 1
Fit results for parameters A, B, R_p and R_s for HRS and LRS.

State	A (Ω^{-1})	B ($V^{-1/2}$)	R_p (Ω)	R_s (Ω)
HRS	$8.0 \cdot 10^{-10}$	12.87	1923	$6.0 \cdot 10^{6}$
LRS	$1.4 \cdot 10^{-6}$	6.79	1586	$5.0 \cdot 10^{4}$

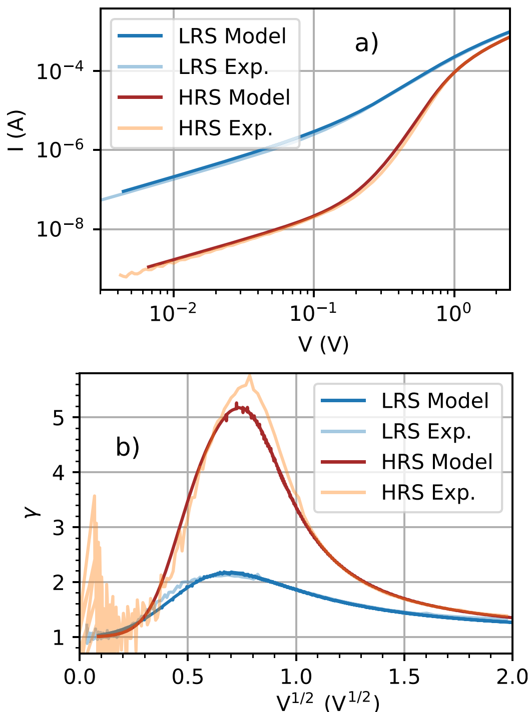

Fig. 4. Comparison between experimental values and a fitted PF conduction model with series and parallel resistances for a) V-I and b) $V^{1/2}$-γ at positive polarity.

Equation (1) has 4 fit parameters A, B, R_s and R_p. By performing a fit to the measured HRS and LRS I-V curves at positive polarity (Table 1) we obtain results which agree with experimental observations and reproduce the γ behavior (Fig. 4). The series resistance values R_s are close to the measured experimental values of $6.8 \cdot 10^6$ Ω for HRS and $5.6 \cdot 10^4$ Ω for LRS, and the parallel resistance R_p is close to the resistance of 1575 Ω measured from Ohmic Ag/PCMO/Ag interfaces, which corresponds to a situation where the oxide layer R_s and the PF-element are not present. From the parameter A we can qualitatively deduce that the trap energy level ϕ_B is larger in HRS than in the LRS.

The results from the conduction model fitting further reinforce the proposed switching based on an AlO_x interface layer. The changing non-linear interface resistance is associated with the oxide layer at the Al/PCMO-interface. The HRS corresponds to a thicker AlO_x layer with high resistance and an asymmetric contact where the conduction is limited by the Schottky barrier. In the LRS the oxide layer is reduced, weakening the rectifying contact enough to make the symmetric PF conduction dominate.

3.3. State retention and endurance

Since reliability is a very important factor in the design of new electronic elements and a known weakness of the RS-based devices, we analyzed the endurance and state retention of our devices. To do so we utilize a single write pulse protocol with asymmetrical voltages of 18 V and −16 V. The results for repeated alternating HRS and LRS writes are presented in Fig. 5a. The resistance was read with a voltage of −200 mV between the writes. The read voltage was selected to be in the Ohmic region to secure a correct reading of the non-volatile state and to avoid possible accidental writes.

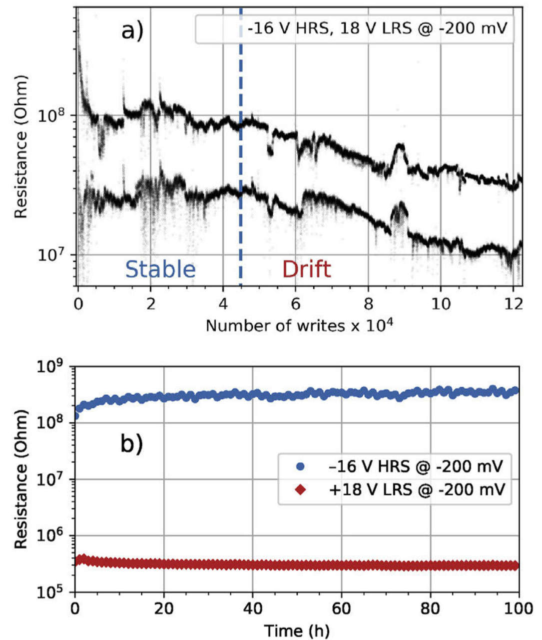

Fig. 5. a) Device resistance over 10^5 repeated writes. b) State retention measurements for HRS and LRS over a timespan of 100 h.

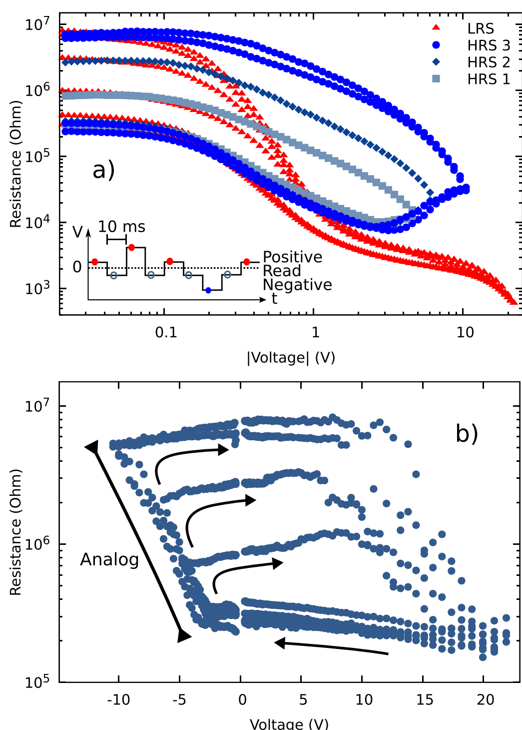

Fig. 6. Multilevel switching showing both a) instantaneous and b) remnant resistances for multiple loops of varying LRS write amplitudes. The remanent resistance shows a well-defined dependence on write voltage on negative polarity.

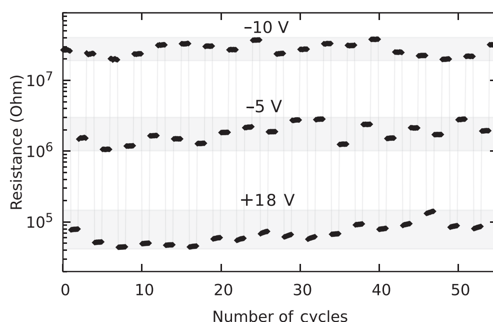

Fig. 7. Demonstration of the multilevel capabilities of the devices. Switching was done by applying constant voltage pulses.

The endurance tests were done with over 10^5 repeated writes without losing the RS. Initially the device showed large changes in HRS and LRS resistances, after which the switching ratio stabilized. HRS and LRS states stayed distinguishable with respect to the previous state over the whole experiment, although a visible drift towards lower resistances was seen after $5 \cdot 10^4$ writes. The drift was caused by the constant write voltages and has been observed in other RS compounds [59]. The local electric field inside the bulk region is much lower than at the interface, which causes some vacancies to get stuck inside the bulk instead of returning to the interface region. This effect lowers the amount of vacancies at the interface over repeated cycling with constant write voltage amplitudes, which lowers the interface resistance. It can be corrected by introducing a feedback loop which adjusts voltage amplitudes for the optimal switching ratio during operation [59,60].

State retention over time was tested by applying LRS or HRS state to the device and then measuring the resistance over a timespan of 100 h (Fig. 5b). The HRS and LRS states stay mostly unchanged after the initial relaxation. The resistance drift is small, which is beneficial for the multilevel RS since multiple levels require the device to be stable. The initial relaxation could be beneficial for neuromorphic applications, as it can be used to implement leaky-integrate-and-fire neurons [20].

3.4. Multilevel switching

The dependence of the HRS-resistance on the HRS writing voltage amplitude was used to achieve analog multilevel switching (Fig. 6). In order to do this, we utilized the pulsing protocol depicted in Fig. 6, which consists of several negative writing pulses of different amplitudes and an erase pulse of higher positive amplitude. After each writing (or erasing) pulse we measured the remnant resistance with a small probe voltage of −50 mV which was low enough not to affect the resistive state.

The HRS write amplitude was varied to give rise to multiple different intermediate resistance states spanning from the HRS resistance to the LRS resistance. The applied LRS write placed the device into a known and stable state which worked as a reference point. The remnant resistance (Fig. 6 inset) measured between the writes shows a well-defined dependence to the write amplitude on the negative polarity. As a result, the resistance of the device can be tuned to a desired value between the limiting HRS and LRS resistances. Additionally, multilevel switching was demonstrated with constant amplitude voltage pulses of 100 ms (Fig. 7).

As long as the resistance can be changed in small increments, an error correction algorithm can be used to fine-tune the resistance for improved accuracy [60]. For conventional discrete memory applications, the demonstrated 4 states can be extended by introducing more steps in the writing voltage. The devices are also suited for neuromorphic applications as the switching doesn't have discontinuities in the negative polarity, which allows the storing of synaptic weights [21,22].

4. Conclusions

To summarize, RS devices were manufactured from the perovskite $Pr_{0.6}Ca_{0.4}MnO_3$ with an asymmetric pair of Ag and Al metal interfaces. The devices exhibited stable bipolar switching with multiple intermediate resistive states. The switching was shown to be non-volatile and repeatable. The conduction model analysis indicates an interplay of bulk-limited Poole-Frenkel conduction and interface-limited Schottky conduction depending on the device state, hinting to a modulation of the AlO_x barrier thickness due to field-assisted oxygen vacancy migration. The resistance states show a well-defined dependence on write voltage which allows for a selection of resistance values between two limiting values when a suitable programming sequence is used. The multilevel switching makes the device a candidate for neuromorphic memory applications, although further work is needed in optimizing the devices and taking advantage of their conduction mechanisms in order to better mimic the special functionalities of biological systems.

Acknowledgments

This work was financially supported by the Academy of Finland

project 308285. The authors also acknowledge the Jenny and Antti Wihuri Foundation for financial support. V.L. is also grateful for the support provided by the University of Turku Graduate School.

References

[1] D. Ielmini, Brain-inspired computing with resistive switching memory (RRAM): devices, synapses and neural networks, Microelectron. Eng. 190 (2018) 44–53.
[2] D. Ielmini, H.-S.P. Wong, In-memory computing with resistive switching devices, Nat. Electron. 1 (2018) 333–343.
[3] M.A. Zidan, J.P. Strachan, W.D. Lu, The future of electronics based on memristive systems, Nat. Electron. 1 (2018) 22.
[4] E. Linn, R. Rosezin, S. Tappertzhofen, U. Böttger, R. Waser, Beyond von neumannlogic operations in passive crossbar arrays alongside memory operations, Nanotechnology 23 (2012) 305205.
[5] S. Moradi, R. Manohar, The impact of on-chip communication on memory technologies for neuromorphic systems, J. Phys. D Appl. Phys. 52 (2019), 014003.
[6] W. Maass, Energy-efficient neural network chips approach human recognition capabilities, Proc. Natl. Acad. Sci. U.S.A. 113 (2016) 11387–11389.
[7] K. Kalantar-zadeh, J.Z. Ou, T. Daeneke, A. Mitchell, T. Sasaki, M.S. Fuhrer, Two dimensional and layered transition metal oxides, Appl. Mater. Today 5 (2016) 73–89.
[8] C.-l. Liu, S.-h. Luo, H.-b. Huang, Y.-c. Zhai, Z.-w. Wang, Layered potassium-deficient P2– and P3–type cathode materials KxMnO2 for k–ion batteries, Chem. Eng. J. 356 (2019) 53–59.
[9] F. Bella, A.B. Muoz-Garca, G. Meligrana, A. Lamberti, M. Destro, M. Pavone, C. Gerbaldi, Unveiling the controversial mechanism of reversible na storage in TiO2 nanotube arrays: amorphous versus anatase TiO2, Nano Res. 10 (2017) 2891–2903.
[10] F. Bella, A.B. Muoz-Garca, F. Col, G. Meligrana, A. Lamberti, M. Destro, M. Pavone, C. Gerbaldi, Combined structural, chemometric, and electrochemical investigation of vertically aligned TiO2 nanotubes for Na-ion batteries, ACS Omega 3 (2018) 8440–8450.
[11] S. Galliano, F. Bella, G. Piana, G. Giacona, G. Viscardi, C. Gerbaldi, M. Grtzel, C. Barolo, Finely tuning electrolytes and photoanodes in aqueous solar cells by experimental design, Sol. Energy 163 (2018) 251–255.
[12] T.D. Lee, A.U. Ebong, A review of thin film solar cell technologies and challenges, Renew. Sustain. Energy Rev. 70 (2018) 1286–1297.
[13] F. Bella, A. Verna, C. Gerbaldi, Patterning dye-sensitized solar cell photoanodes through a polymeric approach: a perspective, Mater. Sci. Semicond. Process. 73 (2018) 92–98.
[14] B. Miccoli, V. Cauda, A. Bonanno, A. Sanginario, K. Bejtka, F. Bella, M. Fontana, D. Demarchi, One-dimensional ZnO/gold junction for simultaneous and versatile multisensing measurements, Sci. Rep. 6 (2016) 29763.
[15] S. Bagdzevicius, K. Maas, M. Boudard, M. Burriel, Interface-type resistive switching in perovskite materials, J. Electroceram. 39 (2017) 157–184.
[16] A. Sawa, Resistive switching in transition metal oxides, Mater. Today 11 (2008) 28–36.
[17] X. Hong, D.J. Loy, P.A. Dananjaya, F. Tan, C. Ng, W. Lew, Oxide–based RRAM materials for neuromorphic computing, J. Mater. Sci. 53 (2018) 8720–8746.
[18] P. Stoliar, J. Tranchant, B. Corraze, E. Janod, M.-P. Besland, F. Tesler, M. Rozenberg, L. Cario, A leaky-integrate-and-fire neuron analog realized with a mott insulator, Adv. Funct. Mater. 27 (2017), 1604740.
[19] Y. Pan, T. Wan, H. Du, B. Qu, D. Wang, T.-J. Ha, D. Chu, Mimicking synaptic plasticity and learning behaviours in solution processed SnO2 memristor, J. Alloys Compd. 757 (2018) 496–503.
[20] C. Adda, J. Tranchant, P. Stoliar, B. Corraze, E. Janod, R. Gay, R. Llopis, M. Besland, L.E. Hueso, L. Cario, An artificial neuron founded on resistive switching of Mott insulators, in: 2017 IEEE Int. Mem. Workshop (IMW), 2017, pp. 1–4.
[21] S.H. Jo, T. Chang, I. Ebong, B.B. Bhadviya, P. Mazumder, W. Lu, Nanoscale memristor device as synapse in neuromorphic systems, Nano Lett. 10 (2010) 1297–1301.
[22] K. Moon, A. Fumarola, S. Sidler, J. Jang, P. Narayanan, R.M. Shelby, G.W. Burr, H. Hwang, Bidirectional non–filamentary RRAM as an analog neuromorphic synapse, part i: Al/mo/Pr0.7Ca0.3MnO3 material improvements and device measurements, IEEE J. Electron. Devices Soc. 6 (2018) 146–155.
[23] N. Panwar, U. Ganguly, Variability assessment and mitigation by predictive programming in Pr0.7Ca0.3MnO3 based RRAM, in: 73rd Annu. Dev. Res. Conf. (DRC), 2015, pp. 141–142.
[24] Z. Wang, S. Joshi, S. Savelev, W. Song, R. Midya, Y. Li, M. Rao, P. Yan, S. Asapu, Y. Zhuo, et al., Fully memristive neural networks for pattern classification with unsupervised learning, Nat. Electron. 1 (2018) 137.
[25] D.S. Jeong, C.S. Hwang, Nonvolatile memory materials for neuromorphic intelligent machines, Adv. Mater. 30 (2018) 1704729.
[26] S. Yu, Neuro-inspired Computing Using Resistive Synaptic Devices, Springer International Publishing, 2017.
[27] T.-G. Seong, B.-S. Lee, K.B. Choi, S.-H. Kweon, B.Y. Kim, K. Jung, J.W. Moon, K.J. Lee, K. Hong, S. Nahm, Unipolar resistive switching properties of amorphous $Pr_{0.7}Ca_{0.3}MnO_3$ films grown on a $Pt/Ti/SiO_2/Si$ substrate, Curr. Appl. Phys. 14 (2014) 538–542.
[28] K. Tsubouchi, I. Ohkubo, H. Kumigashira, M. Oshima, Y. Matsumoto, K. Itaka, T. Ohnishi, M. Lippmaa, H. Koinuma, High-throughput characterization of metal electrode performance for electric-field-induced resistance switching in metal/$Pr_{0.7}Ca_{0.3}MnO_3$/metal structures, Adv. Mater. 19 (2007) 1711–1713.
[29] S.-L. Li, J. Li, Y. Zhang, D.-N. Zheng, K. Tsukagoshi, Unipolar resistive switching in high-resistivity $Pr_{0.7}Ca_{0.3}MnO_3$ junctions, Appl. Phys. A 103 (2011) 21–26.
[30] A.M. Sheri, H. Hwang, M. Jeon, B. Lee, Neuromorphic character recognition system with two PCMO memristors as a synapse, IEEE Trans. Ind. Electron. 61 (2014) 2933–2941.
[31] S. Lashkare, S. Chouhan, T. Chavan, A. Bhat, P. Kumbhare, U. Ganguly, PCMO RRAM for integrate-and-fire neuron in spiking neural networks, IEEE Electron. Device Lett. 39 (2018) 484–487.
[32] P. Kumbhare, I. Chakraborty, A. Khanna, U. Ganguly, Memory performance of a simple Pr0.7Ca0.3MnO3-based selectorless RRAM, IEEE Trans. Electron. Dev. 64 (2017) 3967–3970.
[33] X. Liu, K.P. Biju, E.M. Bourim, S. Park, W. Lee, J. Shin, H. Hwang, Low programming voltage resistive switching in reactive metal/polycrystalline Pr0.7Ca0.3MnO3 devices, Solid State Commun. 150 (2010) 2231–2235.
[34] A. Sawa, T. Fujii, M. Kawasaki, Y. Tokura, Hysteretic current–voltage characteristics and resistance switching at a rectifying Ti/$Pr_{0.7}Ca_{0.3}MnO_3$ interface, Appl. Phys. Lett. 85 (2004) 4073–4075.
[35] T. Nakamura, K. Homma, K. Tachibana, Thin film deposition of metal oxides in resistance switching devices: electrode material dependence of resistance switching in manganite films, Nanoscale Res. Lett. 8 (2013) 76.
[36] S. Asanuma, H. Akoh, H. Yamada, A. Sawa, Relationship between resistive switching characteristics and band diagrams of Ti/$Pr_{1-x}Ca_xMnO_3$ junctions, Phys. Rev. B 80 (2009) 235113.
[37] Z.L. Liao, Z.Z. Wang, Y. Meng, Z.Y. Liu, P. Gao, J.L. Gang, H.W. Zhao, X.J. Liang, X.D. Bai, D.M. Chen, Categorization of resistive switching of metal-$Pr_{0.7}Ca_{0.3}MnO_3$-metal devices, Appl. Phys. Lett. 94 (2009) 253503.
[38] M. Fujimoto, H. Koyama, Y. Nishi, T. Suzuki, Resistive switching properties of high crystallinity and low-resistance $Pr_{0.7}Ca_{0.3}MnO_3$ thin film with point-contacted ag electrodes, Appl. Phys. Lett. 91 (2007) 223504.
[39] T. Kramer, M. Scherff, D. Mierwaldt, J. Hoffmann, C. Jooss, Role of oxygen vacancies for resistive switching in noble metal sandwiched Pr0.67Ca0.33MnO3-, Appl. Phys. Lett. 110 (2017) 243502.
[40] P. Kumbhare, I. Chakraborty, A.K. Singh, S. Chouhan, N. Panwar, U. Ganguly, A selectorless RRAM with record memory window and nonlinearity based on trap filled limit mechanism, in: 2015 15th Non–Volatile Mem. Technol. Symp. (NVMTS), 2015, pp. 1–3.
[41] H.-S. Lee, H.-H. Park, The observation of valence band change on resistive switching of epitaxial Pr0.7Ca0.3MnO3 film using removable liquid electrode 107 (2015) 231603.
[42] T. Harada, I. Ohkubo, K. Tsubouchi, H. Kumigashira, T. Ohnishi, M. Lippmaa, Y. Matsumoto, H. Koinuma, M. Oshima, Trap-controlled space-charge-limited current mechanism in resistance switching at Al/$Pr_{0.7}Ca_{0.3}MnO_3$ interface, Appl. Phys. Lett. 92 (2008) 222113.
[43] M.A. Lampert, P. Mark, Current Injection in Solids, Academic Press, 1970.
[44] A. Odagawa, H. Sato, I. Inoue, H. Akoh, M. Kawasaki, Y. Tokura, T. Kanno, H. Adachi, Colossal electroresistance of a $Pr_{0.7}Ca_{0.3}MnO_3$ thin film at room temperature, Phys. Rev. B 70 (2004) 224403.
[45] C. Acha, Graphical analysis of current-voltage characteristics in memristive interfaces, J. Appl. Phys. 121 (2017) 134502.
[46] M. Nyman, T. Elovaara, J. Tikkanen, S. Majumdar, H. Huhtinen, P. Paturi, Epitaxially textured Pr0.6Ca0.4MnO3 thin films under considerably low substrate temperature, Phys. Proced. 75 (2015) 1122–1132.
[47] D.W. Reagor, S.Y. Lee, Y. Li, Q.X. Jia, Work function of the mixed-valent manganese perovskites, J. Appl. Phys. 95 (2004) 7971–7975.
[48] D. Lide, CRC Handbook of Chemistry and Physics, CRC Press I, LLC, 2009.
[49] M.J. Rozenberg, M.J. Snchez, R. Weht, C. Acha, F. Gomez-Marlasca, P. Levy, Mechanism for bipolar resistive switching in transition-metal oxides, Phys. Rev. B 81 (2010) 115101.
[50] T. Kramer, M. Scherff, D. Mierwaldt, J. Hoffmann, C. Jooss, Role of oxygen vacancies for resistive switching in noble metal sandwiched Pr0.67Ca0.33MnO3-δ, Appl. Phys. Lett. 110 (2017) 243502.
[51] N.A. Tulina, A.A. Ivanov, A.N. Rossolenko, I.M. Shmytko, A.M. Ionov, R.N. Mozhchil, S.I. Bozhko, I.Y. Borisenko, V.A. Tulin, X-ray photoelectron spectroscopy studies of electronic structure of Nd2–xCexCuO4–y and YBa2Cu3O7–y epitaxial film surfaces and resistive switchings in high temperature superconductor-based heterostructures, Mater. Lett. 203 (2017) 97–99.
[52] S. Toyoda, T. Namiki, E. Sakai, K. Nakata, M. Oshima, H. Kumigashira, Chemical-state-resolved depth profiles of Al/Pr0.7Ca0.3MnO3 stacked structures for application in resistive switching devices, J. Appl. Phys. 114 (2013) 243711.
[53] E. Dagotto, J. Burgy, A. Moreo, Nanoscale phase separation in colossal magnetoresistance materials: lessons for the cuprates? Solid State Commun. 126 (2003) 9–22.
[54] R. Yang, X.M. Li, W.D. Yu, X.J. Liu, X. Cao, Q. Wang, L.D. Chen, Multiform resistance switching effects in the Al/$La_{0.7}Ca_{0.3}MnO_3$/Pt structure, Electrochem. Solid State Lett. 12 (2009) H281–H283.
[55] D.-J. Seong, M. Hassan, H. Choi, J. Lee, J. Yoon, J.-B. Park, W. Lee, M.-S. Oh, H. Hwang, Resistive-switching characteristics of Al/$Pr_{0.7}Ca_{0.3}MnO_3$ for nonvolatile memory applications, IEEE Electron. Device Lett. 30 (2009) 919–921.
[56] F.-C. Chiu, A review on conduction mechanisms in dielectric films, Adv. Mater.

Sci. Eng. (2014) 1–18, 2014.
[57] W.S. Lau, An extended unified Schottky-poole-frenkel theory to explain the current-voltage characteristics of thin film metal-insulator-metal capacitors with examples for various high-k dielectric materials, ECS J. Solid State Sci. Technol. 1 (2012) N139–N148.
[58] A. Sawa, T. Fujii, M. Kawasaki, Y. Tokura, Interface transport properties and resistance switching in perovskite-oxide heterojunctions, Proc. SPIE 5932 (2005) 59322C.
[59] F. Gomez-Marlasca, N. Ghenzi, P. Stoliar, M.J. Snchez, M.J. Rozenberg, G. Leyva, P. Levy, Asymmetric pulsing for reliable operation of titanium/manganite memristors, Appl. Phys. Lett. 98 (2011) 123502.
[60] P. Stoliar, P. Levy, M. Sánchez, A. Leyva, C. Albornoz, F. Gomez-Marlasca, A. Zanini, C.T. Salazar, N. Ghenzi, M. Rozenberg, Nonvolatile multilevel resistive switching memory cell: a transition metal oxide-based circuit, IEEE Trans. Circuits Syst. II, Exp. Briefs 61 (2014) 21–25.

A. Schulman & A. Beiranvand & V. Lähteenlahti & H. Huhtinen & P. Paturi

Appearance of glassy ferromagnetic behavior in $Gd_{1-x}Ca_xMnO_3$(0$\leq x \leq$1) thin films: A revised phase diagram

Journal of Magnetism and Magnetic Materials, 498, 2020, 166149

Journal of Magnetism and Magnetic Materials 498 (2020) 166149

Contents lists available at ScienceDirect

Journal of Magnetism and Magnetic Materials

journal homepage: www.elsevier.com/locate/jmmm

Research articles

Appearance of glassy ferromagnetic behavior in $Gd_{1-x}Ca_xMnO_3$ ($0 \leqslant x \leqslant 1$) thin films: A revised phase diagram

A. Schulman, A. Beiranvand, V. Lähteenlahti, H. Huhtinen, P. Paturi

Wihuri Physical Laboratory, Department of Physics and Astronomy, University of Turku, FI-20014 Turku, Finland

ARTICLE INFO

Keywords:
Rare earth alloys and compounds
Perovskite oxides
Thin films
Electrical transport
Magnetoresistance
Phase diagrams

ABSTRACT

We report on results of electrical transport properties of $Gd_{1-x}Ca_xMnO_3$ ($0 \leqslant x \leqslant 1$) thin films fabricated on top of $SrTiO_3$ substrates by pulsed laser deposition. The lowest studied doping level ($x < 0.1$) was enough to trigger a transition from the antiferromagnetic state present in the parent compound ($x = 0$) to a ferrimagnetic state. Up to $x = 0.3$, the system exhibits a high temperature insulator paramagnetic state and a low temperature insulator ferrimagnetic one. At higher concentrations, the electrical and magnetical properties of the films differ drastically from the bulk form which shows a strong antiferromagnetic behavior. At mid Ca substitution ($0.4 \leqslant x \leqslant 0.7$), samples show a high temperature charge ordered state with ordering temperatures around room temperature and a low temperature glassy state which was not observed in their bulk counterparts. In contrast, high x samples show a high temperature conductive paramagnetic state and a low temperature insulator antiferromagnetic phase. More interestingly, sample $x = 0.9$ shows a distinct minimum in the resistivity versus temperature plots and a region of thermal hysteresis which indicate a first order transition. Magnetoresistance measurements display a strong irreversibility which we attributed to phase separation effect of a kinetically arrested ferromagnetic metallic phase and a stable antiferromagnetic insulator phase. Based on the above observations and previous magnetic results, we have reconstructed a phase diagram and characterized the properties of each phase.

1. Introduction

The exceptional electrical transport properties of mixed valence perovskite manganites $R_{1-x}A_xMnO_3$ (R = rare earth cation, A = alkaline earth cation) have created a surge in interest due to their possible technological capabilities [1]. This is largely due to the colossal magnetoresistance effect (CMR) which stems from an intrinsically inhomogeneous ground state usually comprised of metallic ferromagnetic (FMM) and insulating antiferromagnetic (AFI) domains [2,3]. This place them as key materials for applications in a variety of systems such as magnetic random access memories (MRAM) [4,5], magnetic sensors [6,7], and various spintronics devices [8,9]. Furthermore, interfaces made of these materials have shown non-volatile and reversible resistance properties, making them also suitable to perform as resistive random access memories (RRAM) [10,11].

It is well known that all the physical properties of manganites are extremely sensitive to the ionic size of both the rare-earth metal and the alkaline cation [12]. The more the lattice distorts from the cubic perovskite structure, the lower the electron bandwidth will be. While the higher bandwidth compounds (La, Pr, or Nd) have been intensively investigated [2,12,13], much fewer studies have been performed on the heavier R systems, which have a very distorted perovskite structure [14–16]. Due to the small size of the Gd^{3+} ion, the $Gd_{1-x}Ca_xMnO_3$ (GCMO) family is considered a low bandwidth manganite and is usually characterized by an insulating behavior [17–19]. There are very few comprehensive studies on the physical properties of $Gd_{1-x}Ca_xMnO_3$ compared to other manganite compounds, possibly due to its lack of transition to the metallic state and a large neutron absorption cross section which makes it very difficult to establish a reliable phase diagram.

It is known that for low x concentrations ($0 < x < 0.4$), the system shows a paramagnetic insulator behavior with a transition to a ferrimagnetic insulator state at low temperatures which can be interpreted as two interacting magnetic networks with a Mn-based and a Gd-based ferromagnetic sublattices with opposite orientations [18,20,21]. Additionally, Kimura et al. [22] showed that ferroelectricity can be induced by applying magnetic fields as low as 1T. This strong magnetodielectric coupling could be of interest for the design of future magneto-optic devices [23]. For mid x values ($0.4 \leqslant x \leqslant 0.7$), there is an insulating charge (and orbital) ordered state (CO/OO) at high temperatures where the carriers are localized in a checkerboard pattern [13,24]. Also, this substitution shows a metal-insulator transition

E-mail address: alejandro.schulman@utu.fi (A. Schulman).

https://doi.org/10.1016/j.jmmm.2019.166149
Received 9 September 2019; Received in revised form 8 November 2019; Accepted 13 November 2019
Available online 15 November 2019
0304-8853/ © 2019 Elsevier B.V. All rights reserved.

without a phase transition at high temperatures [17,25]. Nonetheless, it has been shown that a transition to a metallic phase (IMT) can be induced by the application of an external electric field even at room temperature [26]. High x concentrations ($0.8 \leqslant x$) present a low temperature antiferromagnetic state and hints of a competing ferromagnetic phase that leads to frustration and a glassy state [27–29] but very little information was found on the electrical transport properties in this substitution range at low temperatures [24].

Moreover, when such materials are prepared in thin film form, their physical properties can be different from the ones observed in bulk form and are usually sensitive to the choice of deposition method, parameters and substrate [30]. It is why is very important to construct a phase diagram with samples fabricated in similar conditions, especially for thin films. In our previous study [31], we surveyed the magnetic phase diagram of this family in thin film form. We found that transition temperatures of the CO/OO phase of mid range concentrations were shifted almost 100 degrees towards higher temperatures and that concentration $x = 0.4$ also presented the CO/OO phase which was not present in its bulk counterpart. Since a detailed study of the electrical transport properties as a function of composition and external factors (e.g. temperature and field) is still lacking; we have combined our previous study of magnetism with electronic transport measurements and reconstructed the completed phase diagram by characterizing each phase with its associated electrical and magnetical properties.

2. Experimental details

Epitaxial thin films of $Gd_{1-x}Ca_xMnO_3$ ($0 \leqslant x \leqslant 1$) (GCMO) were deposited by pulsed laser deposition (PLD) on top of $SrTiO_3$ (STO) substrates. For all the concentrations we utilized 1500 pulses of XeCl-laser ($\lambda = 308$ nm) with energy density 2 J/cm^2 and frequency of 5 Hz. The deposition temperature was 700 °C and the oxygen partial pressure was kept at 23 Pa, post-deposition annealing was performed *in situ* at atmospheric oxygen pressure for 10 min also at 700 °C. Phase purity and film crystallinity were examined by X-ray diffraction (XRD), and all samples were found to be single phase and of good quality, specifics of the deposition process and crystal structure can be found in our previous works [26,31]. To further assess the quality of the samples and their strain state, reciprocal space mappings (RSM) were collected with a Panalytical Empyrean diffractometer equipped a PixCel 3D detector. Electrical transport properties were measured using the four-probe method in a 9 T Quantum Design physical properties measurement system (PPMS). For this, four Au electrodes were sputtered on top of the samples with a distance between electrodes of 250 µm. Au electrodes were chosen because they form an ohmic junction with the GCMO samples if low enough bias is applied [26]. All the magnetotransport measurements were carried out in a configuration where the applied magnetic field is perpendicular to the sample surface.

3. Results and discussion

Our samples are grown as a single phase along the (00 l) direction as the out-of-plane direction, and the in-plane lattice is rotated 45° with respect to the STO lattice, as expected for these types of structures. In order to deepen the analysis of the crystal structure of the films, we performed reciprocal space mappings around the GCMO (116) reflection. In Fig. 1 we present the results for just three concentrations ($x = 0.2$, $x = 0.5$ and $x = 0.9$) but all samples display similar results. None of the samples showed any twinning, although the presence of nano-twinned domains cannot be discarded as it will not be distinguishable with these types of scans. In fact, such domains were very recently observed in $GdMnO_3$ thin films using high resolution transmission electron microscopy [33]. Fig. 1 show that the GCMO (116) reflection is not aligned with the substrate (031) reflection along the $Q_{[110]}$ direction. This strongly indicates that the samples are not fully strained. In Fig. 1, it can also be seen that the film's reflection changes

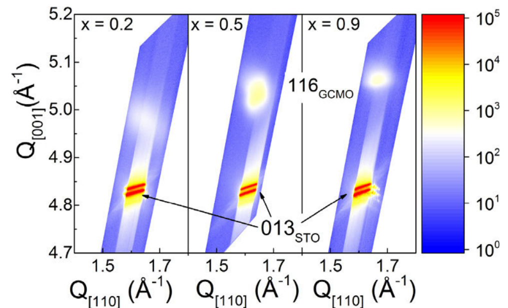

Fig. 1. Reciprocal space map around the (116) Bragg reflection for the x = 0.2 (left), x = 0.5 (center) and x = 0.9 (right) films.

from an elliptic to a circular shape by increasing the doping from 0.2 to 0.5, a broadening of the peak can be expected when trying to deposit an orthorombic structure on top of a cubic substrate [32] as it is the case for the samples in the low substitution range, while the higher Ca concentrations showed a tetragonal structure. The evolution of the out-of-plane lattice parameters can also be observed in Fig. 1 and show identical results to the ones obtained by the $\theta - 2\theta$ scans along the (00l), (0kk) and (hh2h) directions [31]. Results are summarized in Fig. 2(b) along with their bulk counterparts. Although there is a nominal mismatch between the films and the STO substrate that varies with Ca concentration, we found that the lattice parameters of the films follow closely the values observed in the bulk samples, indicating that the majority component of the films is fully relaxed in accordance with what was observed in Fig. 1.

Sample surface was probed by AFM to further assess the quality of the samples. They were found to be very smooth with a root mean square roughness between 0.69 nm and 0.95 nm for all samples. Thickness of the samples was determined from X-ray reflectivity measurements (XRR) from the positions of the interference minima [34]. The results can be found in [31] and they show that the films become thicker as the Ca concentration increases. This was not expected as we utilized exactly the same deposition parameters for all samples. This was caused by an unintended difference in the densities of our home-made PLD targets.

The lower the Ca concentration, the denser the targets are and the lower the films growing rate. Another cause for this could have been a difference of the deposition rate of the Gd as compared to Ca, which would result in an enrichment in Ca with respect to nominal concentration. To check for this effect, we have estimated the chemical compositions of all the samples by energy dispersive spectroscopy

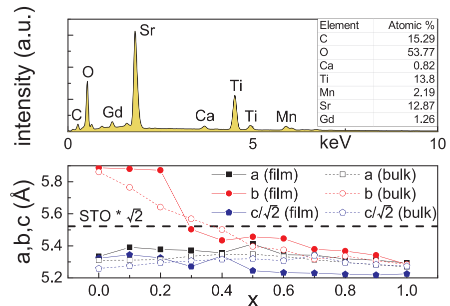

Fig. 2. (a) EDS analysis of the spectra obtained for the x = 0.4 film. (b) Lattice parameters of the films and bulk samples as function of the Ca substitution. The dashed line indicates the STO diagonal value (5.52 Å) as it is assumed that the film crystal lattices are rotated 45° with respect to the STO.

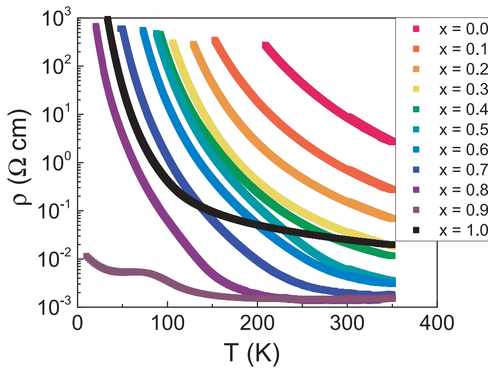

Fig. 3. Temperature dependence of the four wire resistivity for the whole studied concentration range ($0 \leqslant x \leqslant 1$).

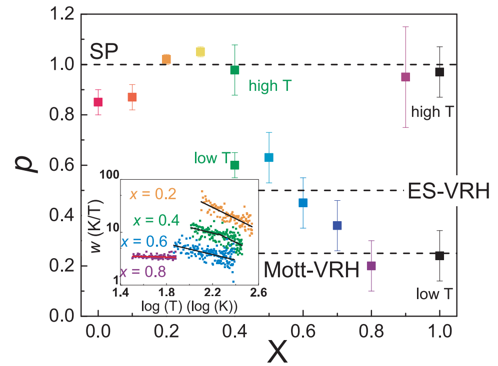

Fig. 4. Exponent p versus x. It can be seen that different concentrations have different conduction mechanisms. Samples $x = 0.4$ and $x = 1.0$ exhibit two exponents which corresponds to different temperature ranges, a small polaron conduction for high temperatures for both samples, and ES-VRH and Mott VRH at low temperatures for $x = 0.4$ and $x = 1.0$ respectively. Inset: dependence of the logaritmic derivative d(log(ρ))/d(log(T)) plotted in a double logarithmic scale. The curves are shifted for clarity.

(EDS). In Fig. 2(a), we show the spectra for sample $x = 0.4$ as an example, since all samples showed equivalent results. The EDS analysis confirmed the elemental compositions of all samples, which showed a composition similar to the nominal values and no systematic deviation of the nominal compositions in function of x was observed.

Fig. 3 shows the temperature dependence of the resistivity for all studied concentrations. It is clear that the resistivity changes consistently as the doping is modified until an insulator-to-metal transition can be observed for $x = 0.9$ at low temperatures. At first glance, the samples display very similar semiconducting-like behavior. However, detailed analysis of the curves reveal great differences in the conduction mechanism depending on the value of x. The resistivity data was analyzed using the procedure suggested by Zabrodskii and Shlimak [35]. As for all manganites in the insulator state, the resistivity data can be fitted to the general hopping law expression: $\rho(T) = \rho_0' T^s \exp\left(\frac{T_0}{T}\right)^p$, where ρ_0' is a prefactor, the exponents s and p determine the dominant type of conduction mechanism. For example, exponents $s = 0$ and $p = 1$ indicate a thermal activation of the charge carriers from valence band to the conduction band across the band gap, while $s = 1$ and $p = 1$ indicate that the adiabatic Emin–Holstein model or small polaronic hopping is dominant. The case of an exponent $s = 0$ and p lower than 1 is characteristic of the variable range hopping conduction (VRH). In the VRH case, p relates to the dimensionality of the conduction. The type of VRH can also be differentiated by the value of the exponent p (with $p = 0.25$ for a Mott type and $p = 0.5$ for the Efros and Shklovskii type (ES)). The Mott type takes place when Coulomb interactions are negligible while the theory of VRH conduction in the presence of a Coulomb gap is described by ES-VRH model [36,37]. To determine the dominant conduction mechanism, we utilize the so-called reduced activation energy $w = -d(\log(\rho))/d(\log(T))$ [35,38]. In the cases where $s = 0$, the conduction mechanism can then be objectively determined by analyzing the slopes of w vs. temperature in a double logarithmic scale, as showed in the inset of Fig. 4. The best fit of the slope directly produces the exponent p which are presented in Fig. 4. For the thermally activated mechanisms that have $s \neq 0$ and $p = 1$, we still expect to see an exponent p close to 1, due to the low temperature range that we are measuring and the typical band gap of the manganite system. Nevertheless, all the cases where exponent $p \approx 1$ will be further analyzed to determine their respective conduction mechanism. While all the samples were analyzed successfully by this method, we show the w vs. $log(T)$ plots for only half of them (the even numbered) in the inset of 4 as an example. The results of the complete analysis is summarized in the main panel of Fig. 4 and show four distinct doping regimes: $0 \leqslant x \leqslant 0.4$, $0.4 \leqslant x \leqslant 0.7$, $0.7 < x \leqslant 0.85$ and $0.85 < x < 1$.

In the low Ca concentration region ($0 \leqslant x \leqslant 0.4$), the obtained exponent is close to 1 which indicates a thermally activated conduction, either similar to bad-gap semiconductors (with $s = 0$) or polaronic in nature with $s = 1$ or $s = 3/2$ for adibatic and non-adiabatic polaronic conduction, respectively. After plotting the curves in the correct axis, it is clear that the conduction mechanism in this substitution range can be well explained by the adiabatic Emin–Holstein model [39] which gives a resistivity of the form $\rho(T) = \rho_0' T \exp(E_A/k_B T)$, where ρ_0' is a temperature independent pre-factor, k_B the Boltzmann constant and E_A the hopping energy. This thermally activated model is very common on manganites in their high temperature paramagnetic phase and is related to the electrons' coupling with the elastic lattice polarons originated from the strong Jahn–Teller effect of Mn^{3+} ions [40]. The small polaron mechanism implies that differently to the band-gap semiconductors, the highly temperature-dependent quantity is the mobility instead of the carrier density which is consistent with the Hall effect measurements [41]. Unlike other manganites, the GCMO in this substitution range does not exhibit a metal-insulator transition or a large magnetoresistance near the Curie temperature, probably due to the small ionic size of Gd^{3+}. To calculate the polaron hopping energies, we replotted the resistivity curves as $\ln(\rho/T)$ vs. $1/T$ (Fig. 5(a)), which yields a straight line where E_A can be directly obtained from the slope (see inset of Fig. 5(a)). We observe a decrease in the hopping energies with increasing Ca substitution and this can be explained by taking into account that an increase in x causes a larger bandwidth. This in turn causes a charge delocalization due to a decrease of the electron–phonon interactions, and thus, the energy required to liberate a free carrier is reduced, which is consistent with the trend observed in Fig. 3. Values for the inferred E_A are very similar to reported ones in other manganite compounds in the high-temperature paramagnetic insulator phase [42–45].

Sample $x = 0.4$ displayed a crossover of conduction mechanisms. At around 180 K the exponent changes from 1 to 1/2, as can be seen in the inset of Fig. 4. The electronic transport below the transition point corresponds to the ES-VRH mechanism. Interestingly, between the concentrations 0.4 and 0.7 a high temperature charge-order phase was observed in the magnetic measurements. Therefore, the observed transition from small polarons to VRH conduction in the $x = 0.4$ sample, is most likely related to this different magnetic phase. Indeed, in half-doped manganites, the Coulomb interaction is believed to be the source for the charge ordering [46]. Fig. 5(b) shows the fit for $p = 0.5$ in samples with Ca concentration between 0.4 and 0.7. For $x = 0.4$ and

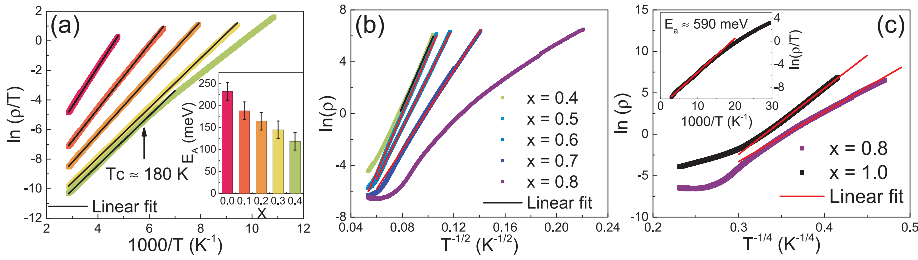

Fig. 5. (a) Arrhenius-type plot ($\ln(\rho/T)$ vs. $1/T$) for the resistivity in the $0 \leqslant x \leqslant 0.4$ range showing a good fit to the adiabatic, small-polaron hopping model. In sample 0.4 a transition to another transport mechanism is clearly observed at around 180 K. Inset: Hopping energies obtained with the fitting according to the small polaron model. (b) Semilog plot of the resistivity vs. $T^{-\frac{1}{2}}$ for $0.4 \leqslant x \leqslant 0.8$ concentrations with the linear fit showing the ES-VRH conduction regime, and a comparison with sample $x = 0.8$ which does not show signs of charge-order effect or ES-VRH conduction at any temperature. (c) Semilog plot of the resistivity vs. $T^{-\frac{1}{4}}$ for $x = 0.8$ and $x = 1.0$, indicating that Mott VRH is the dominant conduction mechanism for this Ca concentrations in the AFM phase. The inset show the fit to the SP conduction model for sample $x = 1.0$ at higher temperatures.

0.7, it can be seen that the transition temperatures are much lower than for samples with $x = 0.5$ and 0.6, which is consistent with the magnetic phase diagram. We also observe that sample $x = 0.8$ does not follow the ES-VRH theory in any temperature range which is also consistent with magnetic measurements since this composition does not show the charge-ordered phase. In contrast, sample $x = 0.8$ shows the metallic-like phase in the paramagnetic phase and for the insulator antiferromagnetic phase we found that the exponent was closer to 1/4 (see Fig. 4) which signatures the dominance of the Mott VRH conduction mechanism, as can be seen in Fig. 5(c). The parent compound $CaMnO_3$ shows similar results to the ones reported elsewhere [2,47–49] and, it is known that this sample is a Mott insulator with a transition to a G-type antiferromagnetic state at around 100 K. As expected, once the sample is in the AFM state, the dominant transport mechanism becomes Mott-VRH as is evidenced by the reduction of the observed exponent from 1 at higher temperatures to 1/4 below the transition. The high temperature transport mechanism was also found to be dominated by the Emin-Holstein model as shown by the straight line present in the inset of Fig. 5(c). This is also supported by the fitting where we obtained an activation energy of around 590 eV which is well consistent with values reported earlier [50].

Sample $x = 0.9$ shows a very interesting behavior that was not observed for the same concentration in bulk form [24]. While at high temperatures it shows signs of polaronic conduction (see Fig. 4 and the inset of Fig. 6) similar to samples with low Ca concentration ($x < 0.4$); at lower temperatures, an unexpected metal-insulator transition was observed (Fig. 6), followed by a resistivity minima and an upturn at lower temperatures. Interestingly, the sample shows a clear thermal hysteresis that signifies the first-order nature of the transition. This transition can be dramatically influenced with the application of magnetic field and the resistivity shows a history effect, *i.e.* distinct paths can be achieved by utilizing different measurement protocols. We explored three different protocols, as shown in Fig. 6: (i) Resistivity was measured during both cooling and warming at zero magnetic field. (ii) Resistivity was measured during the warming path at zero field after cycling the magnetic field at 10 K (the response of the resistivity during the magnetic cycling is presented in Fig. 7 (top). (iii) Resistivity was measured during cooling and warming while applying a magnetic field of 9 T.

It can be seen that at high temperatures all paths are identical and that the bifurcation between curve (i) and (ii) appears at the transition temperature, while the bifurcation of curve (iii) occurs at a higher temperature. This behavior can be explained through a phase separation scenario with a coexistence between an insulating antiferromagnetic phase and a metallic ferromagnetic one. When a magnetic field is applied in this coexistence region, the FMM domains will spread rapidly and the resistivity will possess a metallic behavior which

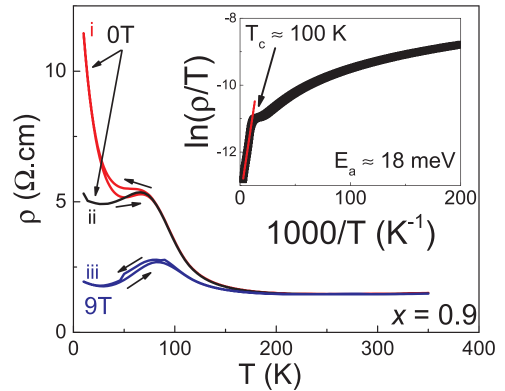

Fig. 6. Resistivity of the sample $x = 0.9$ as a function of temperature in both zero field (i) and in presence of 9 T (iii) perpendicular to the surface of the sample. Curve (ii) shows the warming up at zero field after cycling the field up for the magnetoresistance effect at 10 K (Fig. 7 (top)). A large difference between the different measuring protocols is clearly noticeable. Inset shows that adiabatic small polaron hopping is dominant conduction mechanism in the high temperature paramagnetic phase.

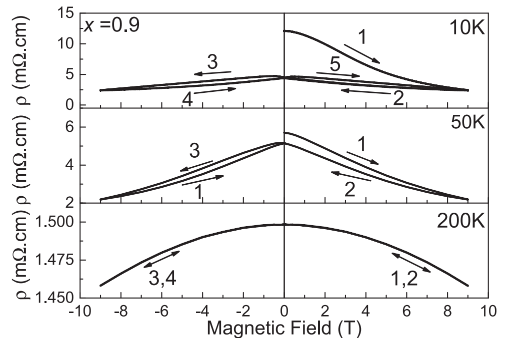

Fig. 7. Magnetic field dependence of the resistivity of the sample $x = 0.9$ at various constant temperatures.

has a non-volatile character. This is due to the critically slow dynamics of the phase transition as the transformation from high temperature to low temperature phase is thwarted on the measurement timescale [51].

As a result, a glass-like arrest of a long range ordered state at low temperatures is observed [52]. With this assumption of a two phase component system the resistivity can be described through an effective medium approximation [53], where f is the fraction of volume of the FMM phase and $(1 - f)$ is the fraction of volume of the AFI phase. In this scenario, the application of a magnetic field increases f (decreasing $(1 - f)$) which generates a strong negative CMR. Since the FMM is arrested and cannot go back to the equilibrium, the coexistence remains to the lowest measured temperature. Moreover, when the field is switched off at a temperature much lower than the transition, the CMR effect is maintained as demonstrated by the difference in the (i) and (ii) curves. Another verification of this arrested phase is the observed logarithmic dependence of the time relaxation (not shown here), which is a typical signature of glassy states. Although similar arrested phases have been observed in other manganite materials such as $Nd_{0.5}Sr_{0.5}MnO_3$ [54] and $Gd_{0.5}Sr_{0.5}MnO_3$ [55], in most cases in bibliography the arrested phase is present only at half doping and rarely at high substitution ranges as in this case [2].

To study this arrested phase in more detail, we performed isothermal measurements of ρ vs. H at temperatures above and below the transition temperatures (Fig. 7). Above the transition, no hysteresis was observed and the sample shows a small negative magnetoresistance of around 2%. As expected, the behavior at lower temperatures is much more complicated. The virgin curve (path 1 in Fig. 7) is different than the subsequent cycles and it shows the transition from the AFI to the arrested FMM phase. The resistivity change was found to be irreversible, since reversing the field only partially restores the sample to the original AFI phase, indicating the non-volatile property of the CMR effect. The difference between the virgin curve and the stable cycles decreases with increasing temperature because the thermal energy starts to compete with the energy barriers between the FMM and AFI phases which will result in a lowering of the arrested FMM fraction.

By combining all the transport measurements results along with previous magnetization studies [31], we were able to reconstruct a phase diagram as shown in Fig. 8. We were able to identify the dominant conduction mechanism for all concentrations and link them with their respective magnetic phase. The resulting phase is somewhat similar to other low bandwidth manganites, especially $Tb_{1-x}Ca_xMnO_3$ [14] where a CO/OO phase near room temperature was observed at half doping levels and a mixture of phases is present at higher dopings.

The adding of Ca to $GdMnO_3$ introduces a hole in the vicinity of the Ca^{2+} ion, which in turn is compensated by adding an electron from the Mn, thus creating a Mn^{4+}. This process creates a transition from the AFM phase existent at $x = 0$ to a ferrimagnetic (FiM) one for $0 < x < 0.4$. This was verified by the magnetization measurements which show the magnetization changing sign towards negative results for $x < 0.5$. This is the result of the Gd spins being anti-parallelly oriented with respect to the Mn spins. We also noticed that in this region the Curie temperature rises as the value of x increases which could be attributed to an increase of the Mn-O-Mn angle as well as a decrease in b cell parameter [24], indicating a reduction in the Jahn–Teller distortion [56,57].

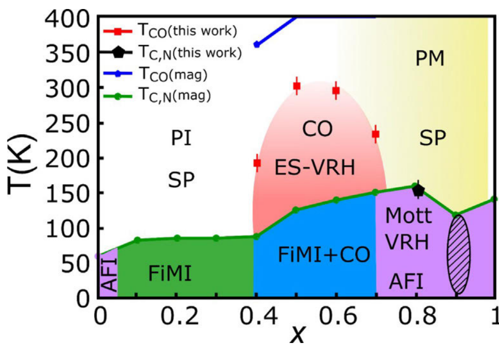

Fig. 8. Phase diagram (in the $x - T$ plane) for $Gd_{1-x}Ca_xMnO_3$. PI, PM, FiMI, AFI, CO, Mott-VRH, ES-VRH and SP abbreviations denote paramagnetic insulator, paramagnetic metal, ferrimagnetic insulator, antiferromagnetic insulator, charge-order, Mott variable range hopping, Efros and Shklovskii variable range hopping, and small polaronic conduction, respectively. The crosshatched region denotes the range over which the coexistence between the AFI phase and an arrested FMM phase was found. The various lines are simply guides to the eye. Previously obtained transition temperatures measured by magnetic measurements are also included for comparison.

Mid concentration samples showed a clear signs of ES-VRH conduction consistent with the observed charge-ordered phase. At lower temperatures the samples show a transition to an ordered ferrimagnetic state which is a sharp contrast to bulk results which displayed AFM ordering. It is possible that the AFM ordering is also present in the film samples and that the true ground state is a mixture of phases. More studies are needed to understand the nature of the ground state and the difference between bulk and thin film properties.

When comparing samples with both high and low Ca substitution, we noticed that they both possess a high temperature paramagnetic state but with wildly different electronic transport properties. While low x concentrations show semiconducting behavior, high x samples exhibit a low conductivity behavior which is a common feature in lightly electron doped Ca-based manganites [15,58,59].

At low temperatures for sample $x = 0.8$, the AFM ordering becomes predominant. Sample $x = 0.9$ show a different behavior as $x = 0.8$ did not show any sign of a metal–insulator transition or CMR effect in the whole studied temperature range even though it possesses a magnetic transition at around 100 K. The $x = 0.9$ sample shows a very distinct behavior when compared with the rest of the series and their bulk counterparts, although more studies are necessary to understand the exact nature of the coexistence region and the properties of the arrested FMM state which seems to have a glassy behavior. Unfortunately, due to the large neutron cross section of Gd, it is very difficult to determine the true magnetic ground state of the system and therefore other complementary techniques such as electron magnetic resonance [60] or X-ray Magnetic Circular Dichroism (XMCD) are necessary to achieve this task.

4. Conclusions

We have presented detailed electronic transport results on epitaxial $Gd_{1-x} Ca_xMnO_3$ thin films in the whole substitution range ($0 \leqslant x \leqslant 1$). For $x \leqslant 0.4$ the curves show an insulator behavior with a conduction mechanism dominated by small polaronic hopping. Sample $x = 0.4$ shows a transition from small polaronic hopping to ES-VRH at around 180 K which is related to the magnetic transition between a paramagnetic state and a charge-ordered one. Samples with $0.4 \leqslant x \leqslant 0.7$ all exhibit the high temperature high order phase accompanied with ES-VRH conduction while $x = 0.8$ shows a high temperature paramagnetic state low conductivity behavior and a low temperature antiferromagnetic state characterized by Mott-VRH conduction. Sample $x = 0.9$ showed a very intriguing behavior where the system shows a clear thermomagnetic history dependence in its electronic transport properties and a non-volatility of the magnetic field induced resistivity change. The observed phenomena have been explained through the phase separation scenario and a kinetic arrest of the electronic phase. This leads to a coexistence of an AFI and kinetically arrested FMM phases at low temperatures. The sample can be stabilized in the metastable FMM phase by applying magnetic field where the sample remains in the arrested phase even if the field is removed. Based on all the experimental results, the phase diagram has been constructed and the dominant characteristic of each phase has been established.

Declaration of Competing Interest

The authors declare that they have no known competing financial interests or personal relationships that could have appeared to influence the work reported in this paper.

Acknowledgments

Authors are indebted to M. Boudard and H. Palonen for valuable discussions. The authors wish to thank the Jenny and Antti Wihuri Foundation and the Academy of Finland Grant No. 308285. A.B. also acknowledges the Väisälä foundation and V.L. the University of Turku Graduate School for general resources and finance.

References

[1] Y. Tokura, Colossal Magnetoresistive Oxides, Gordon and Breach Science, New York, 2004.
[2] E. Dagotto, T. Hotta, A. Moreo, Phys. Rep. 344 (2001) 1.
[3] Y. Tokura, Rep. Prog. Phys. 69 (2006) 797.
[4] M. Bowen, M. Bibes, A. Barthélémy, J.-P. Contour, A. Anane, Y. Lemaı˘tre, A. Fert, Appl. Phys. Let. 82 (2003) 233.
[5] P.K. Siwach, H.K. Singh, N. Srivastava, J. Phys. Condens. Matter 20 (2008) 273201.
[6] Y. Xu, M. Meier, P. Das, M.R. Koblischka, U. Hartmann, Crystal Eng. 5 (2002) 383.
[7] F.M. Araujo-Moreira, M. Rajeswari, A. Goyal, K. Ghosh, V. Smolyaninova, C.J. Lobb, R.L. Greene, Appl. Phys. Lett. 73 (1998) 3456.
[8] M. Bibes, A. Barthélémy, IEEE Trans. Electron Dev. 54 (2007) 1003.
[9] M. Saloaro, M. Hoffmann, W.A. Adeagbo, S. Granroth, H. Dieniz, H. Palonen, H. Huhtinen, S. Majumdar, P. Laukkanen, W. Hergert, A. Ernst, P. Paturi, A.C.S. Appl, Mater. Inter. 8 (2016) 20440.
[10] A. Sawa, Mater. Today 1 (2008) 28.
[11] M.J. Rozenberg, M.J. Sánchez, R. Weht, C. Acha, F. Gomez-Marlasca, P. Levy, Phys. Rev. B 81 (2010) 115101.
[12] M.B. Salamon, M. Jaime, Rev. Mod. Phys. 73 (2001) 583.
[13] T. Tomioka, Y. Tokura, Phys. Rev. B 70 (2004) 014432.
[14] J. Blasco, C. Ritter, J. García, J.M. de Teresa, J. Pérez-Cacha, M.R. Ibarra, Phys. Rev. B 62 (2000) 5609.
[15] N.N. Loshkareva, E.V. Mostovshchikova, Phys. Metals Metallogr. 113 (2011) 19.
[16] M. Rosić, D. Zagorac, D. Milivojević, N. Paunović, J. Zagorac, Z. Dohvević-Mitrović, B. Matović, J. Alloys Comp. 113 (2016) 219.
[17] H. Taguchi, M. Nagao, M. Shimada, J. Solid State Chem. 82 (1989) 914.
[18] S.K. Estemirova, V.F. Balakirev, A.M. Yankin, V.Y. Mitrofanov, S.A. Uporov, V.M. Kozin, T.I. Filinkova, Glass Phys. Chem. 41 (2015) 224.
[19] H.Y. Hwang, S.-W. Cheong, P.G. Radaelli, M. Marezio, B. Batlogg, Phys. Rev. Lett. 75 (1995) 914.
[20] G.J. Snyder, C.H. Booth, F. Bridges, R. Hiskes, S. DiCarolis, M.R. Beasley, T.H. Geballe, Phys. Rev. B 55 (1997) 6453.
[21] O. Peña, M. Bahout, K. Ghanimi, P. Duran, D. Gutierrez, C. Moure, Mater. Chem. 12 (2002) 2480.
[22] T. Kimura, G. Lawes, T. Goto, Y. Tokura, A.P. Ramirez, Phys. Rev. B 71 (2005) 224425.
[23] A. Pimenov, A.A. Mukhin, V.Y. Ivanov, V.D. Travkin, A.M. Balbashov, A. Loidl, Nat. Phys. 2 (2006) 97.
[24] A. Beiranvand, J. Tikkanen, H. Huhtinen, P. Paturi, J. Alloys Comp. 720 (2017) 126.
[25] H. Taguchi, M. Nagao, J. Solid State Chem. 94 (1991) 210.
[26] P. Paturi, J. Tikkanen, H. Huhtinen, J. Magn. Magn. Mater. 432 (2017) 164.
[27] M. Rosić, M. Logar, A. Devecerski, M. Prekajski, A. Radosavljević-Mihajlović, V. Kusigerski, V. Spassojević, B. Matović, Ceram. Int. 37 (2011) 1313.
[28] M. Rosić, M. Logar, J. Zagorac, A. Devecerski, A. Egelja, V. Kusigerski, V. Spassojević, B. Matović, Ceram. Int. 39 (2013) 1853.
[29] M. Rosić, L. Kljaljević, D. Jordanov, M. Stoiljković, V. Kusigerski, V. Spassojević, B. Matović, Ceram. Int. 41 (2015) 14964.
[30] M. McCormack, A. Jin, T.H. Tiefel, R.M. Fleming, J.M. Phillips, J. Appl. Phys. 64 (1994) 3045.
[31] A. Beiranvand, J. Tikkanen, H. Huhtinen, P. Paturi, J. Magn. Magn. Mater. 469 (2019) 253.
[32] P.R. Willmott, J.R. Huber, Rev. Mod. Phys. 72 (2000) 315.
[33] X. Li, C. Lu, J. Dai, S. Dong, Y. Chen, N. Hu, G. Wu, M. Liu, Z. Yan, J.-M. Liu, Sci. Rep. 4 (2014) 7019.
[34] T.C. Huang, R. Gilles, G. Will, Thin Solid Films 230 (1993) 99.
[35] G. Zabrodskii, I.S. Shlimak, Sov. Phys. Semicond. 9 (1975) 391.
[36] R. Rosebaum Phys, Rev. B 44 (1991) 3599.
[37] X.J. Chen, C.L. Zhang, J.S. Gardner, J.L. Sarrao, C.C. Almasan, Phys. Rev. B 68 (2003) 064405.
[38] G. Zabrodskii, Philos. Mag. B 81 (2001) 1131.
[39] D. Emin, T. Holstein, Ann. Phys. 53 (1969) 439.
[40] A.-M. Haghiri-Gosnet, J.-P. Renard, J. Phys. D: Appl. Phys. 36 (2003) 127.
[41] G.J. Snyder, R. Hiskes, S. DiCarolis, M.R. Beasley, T.H. Geballe, Appl. Phys. Lett. 69 (1996) 4254.
[42] M. Jaime, H.T. Hardner, M.B. Salamon, M. Rubinstein, P. Dorsey, D. Emin, Phys. Rev. Lett. 78 (1997) 951.
[43] D.C. Worledge, L. Miéville, T.H. Geballe, J. Appl. Phys. 83 (1998) 5913.
[44] Ch. Jooss, L. Wu, T. Beetz, R.F. Klie, M. Beleggia, M.A. Schofield, S. Schramm, J. Hoffmann, Y. Zhu, Proc. Natl. Acad. Sci 104 (2007) 13597.
[45] E.V. Mostovshchikova, R.I. Zainullina, N.G. Bebenin, T. Arbuzova, N.I. Solin, S.V. Naumov, J. Alloys Comp. 615 (2017) 761.
[46] A.L. Efros, B.I. Shklovskii, J. Phys. C 8 (1974) 49.
[47] C.L. Flint, A.J. Gutter, C.A. Jenkins, E. Arenholz, Y. Suzuki, Appl. Phys. Lett. 115 (2014) 17D712.
[48] H. Taguchi, Phys. Stat. Sol. (a) 88 (1985) 79.
[49] M.E. Melo, A. Correia dos Santos, M.R. Nunes, Int. J. Inorg. Mater. 3 (2001) 915.
[50] W.E. Pickett, D.J. Singh, Phys. Rev. B 53 (1996) 1146.
[51] S. Kundu, T.K. Nath, J. Phys. Condens. Matter 23 (2011) 356001.
[52] M.K. Chattopadhyay, S.B. Roy, P. Chaddah, Phys. Rev. B 72 (2005) 180401.
[53] S. Ju, H. Sun, Z.-Y. Li, J. Phys. Condens. Matter 14 (2002) 631.
[54] R. Rawat, K. Mukherjee, K. Kumar, A. Banerjee, P. Chaddah, J. Phys. Condens. Matter 19 (2007) 256211.
[55] A.A. Wagh, P.S.A. Kumar, H.L. Bhat, S. Elizabeth, J. Phys. Condens. Matter 22 (2010) 026005.
[56] N.G. Bebenin, R.I. Zainullina, S.V. Maikov, V.V. Ustinov, Ya.M. Mukovskii, Phys. Met. Metallogr. 110 (2010) 442.
[57] N.N. Loshkareva, Y.P. Sukhorukov, E.A. Neifel'd, V.E. Arkhipov, A.V. Korolev, V.S. Gaviko, E.V. Panfilova, V.P. Dyakina, Y.M. Mukovskii, D.A. Shulyatev, J. Exp. Theor. Phys. 90 (2000) 389.
[58] X.J. Fan, H. Koinuma, T. Hasegawa, Physica B 323 (2003) 723.
[59] D. Sousa, M.R. Nunes, C. Silveira, I. Matos, A.B. Lopes, M.E. Melo Jorge, Mater.Chem. and Phys. 109 (2008) 311.
[60] V.A. Atsarkin, V.V. Demidov, J. Exp. Theor. Phys. 103 (2006) 589.

V. Lähteenlahti & A. Schulman & A. Beiranvand & H. Huhtinen & P. Paturi

Electron doping effect in resistive switching properties of Al/$Gd_{1-x}Ca_xMnO_3$/Au memristor devices

ACS Applied Materials & Interfaces, 3, 2021, 18365–18371

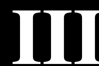

ACS APPLIED MATERIALS & INTERFACES

www.acsami.org Research Article

Electron Doping Effect in the Resistive Switching Properties of Al/$Gd_{1-x}Ca_xMnO_3$/Au Memristor Devices

Ville Lähteenlahti,* Alejandro Schulman, Azar Beiranvand, Hannu Huhtinen, and Petriina Paturi

Cite This: ACS Appl. Mater. Interfaces 2021, 13, 18365−18371 Read Online

ACCESS | Metrics & More | Article Recommendations

ABSTRACT: We report on the resistive switching (RS) properties of Al/$Gd_{1-x}Ca_xMnO_3$ (GCMO)/Au thin-film memristors. The devices were studied over the whole calcium substitution range x as a function of electrical field and temperature. The RS properties were found to be highly dependent on the Ca substitution. The optimal concentration was determined to be near $x = 0.9$, which is higher than the values reported for other similar manganite-based devices. We utilize an equivalent circuit model which accounts for the obtained results and allows us to determine that the electrical conduction properties of the devices are dominated by the Poole−Frenkel conduction mechanism for all compositions. The model also shows that lower trap energy values are associated with better RS properties. Our results indicate that the main RS properties of Al/GCMO/Au devices are comparable to those of other similar manganite-based materials, but there are marked differences in the switching behavior, which encourage further exploration of mixed-valence perovskite manganites for RS applications.

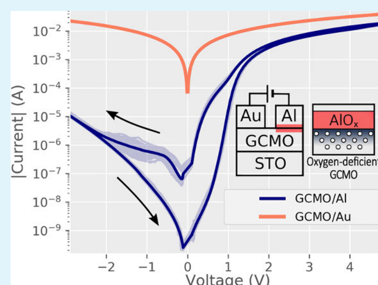

KEYWORDS: *Resistive switching, Perovskite oxides, Poole-Frenkel, $Gd_{(1-x)}Ca_xMnO_3$ and Memristor*

INTRODUCTION

In recent years, many memory technologies have emerged with the goal to replace traditional charge storage-based memory technologies, which are approaching their physical limits of scalability. The most prominent of them are random access memories based on phase change, resistivity change (RRAM), spin-transfer torque magnetoresistance, and ferroelectricity. Out of them, the resistive switching (RS)-based RRAM has been recently gaining traction due to its promising characteristics. The research on RRAM devices has been active since the early 00's, and many candidate materials and explanations for the phenomenon have been proposed.[1−6]

In RS, the resistance of the device can be controlled with an electric field in a nonvolatile way, enabling two-terminal devices with good spatial scalability and minimal supporting circuitry. The phenomenon is based on controllable and reversible structural modification, which is most commonly achieved by the movement of oxygen vacancies.[1] This contrasts with conventional transistor-based memory technologies, where the state is stored nonstructurally in the electrical charge. The advances in RS research have led to device demonstrations with high switching speeds, robust endurance, low power consumption, and compatibility with existing electronics.[7,8] RS devices have also found use in information processing applications, such as neuromorphic computing,[9] matrix-vector multiplication,[10] and convolution kernel operations,[11,12] which pave the way for efficient hardware-based machine learning.

A lot of promising research, including many of the mentioned demonstrations have been performed using mixed-valence perovskite manganites $R_{1-x}A_xMnO_3$, where R is a rare-earth cation and A is an alkali or alkaline earth cation. These compounds are versatile for RS applications since as the concentration of divalent A cations x changes, the compounds go through significant changes in the RS properties. Manganite-based RS devices have been shown to possess good device-to-device variability,[13] forming-less operation,[14] and well-controlled analogue resistance states,[15] all of which are beneficial in building neuromorphic circuits.[16]

The most commonly studied manganite compound is $Pr_{1-x}Ca_xMnO_3$ (PCMO) with $x = 0.3$, which has been proven suitable for both memory and neuromorphic applications with well-performing single devices and large-scale crossbar arrays integrated into existing semiconductor technology.[8,9,13,14,17−19] Other members of the mixed-valence manganite family, such as $La_{1-x}Ca_xMnO_3$[20] and $La_{1-x}Sr_xMnO_3$ (LSMO),[21] share a

Received: February 13, 2021
Accepted: March 30, 2021
Published: April 9, 2021

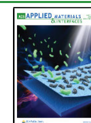

© 2021 American Chemical Society

https://doi.org/10.1021/acsami.1c02963
ACS Appl. Mater. Interfaces 2021, 13, 18365−18371

similar RS mechanism[22] but have distinct RS characteristics which vary over the calcium substitution range. Currently, many of the possible cation combinations remain unexplored, and the optimal manganite material for neuromorphic applications remains undecided.

Manganite-based RS devices usually consist of metal-oxide-metal layer structures, in which one of the metal-oxide interfaces acts as an active electrode where the RS happens. The active interface is made from a reactive material, such as Al, Ti, or TiN, which forms an insulating oxide barrier layer with the manganite[1,23] (Figure 1 inset). The properties of the barrier are modified with a controlled electric field. The field causes oxygen vacancy drift at the interface and the perovskite structure in the vicinity of the interface.[24] These changes in turn enable nonvolatile control of the resistivity and capacitance of the RS device.[1,22]

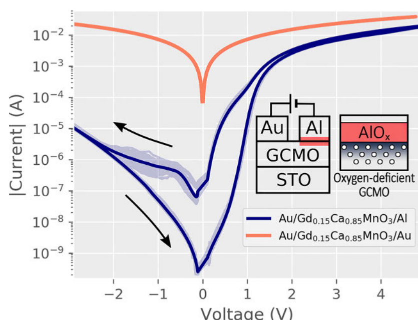

Figure 1. Averaged $I(V)$ curves for Al/GCMO/Au and Au/GCMO/Au interfaces with $x = 0.85$ over 50 repeated measurements; the lighter shade indicates individual measurements. The conduction in Au interfaces is Ohmic, and the switching happens at the Al interface. The inset shows the measurement configuration and the active aluminum switching interface with the oxygen-deficient GCMO region and the AlO_x barrier layer.

In this article, we report the RS properties of $Gd_{1-x}Ca_xMnO_3$ (GCMO) ($0 \leq x \leq 1$) for the first time. GCMO is studied with aluminum as the active electrode, and the resulting devices are characterized and analyzed over the whole calcium substitution range as a function of temperature and electric field. As a mixed-valence perovskite manganite, GCMO is structurally similar to PCMO, but the Gd cation has a smaller ionic radius than Pr, which entails a more distorted structure. This causes a lower bandwidth and more insulating bulk, which is beneficial in RS applications due to lower leakage currents. The calcium concentration series of the GCMO is found to have optimal RS properties at high calcium doping, which cannot be predicted from previous studies on other manganite materials.

EXPERIMENTAL DETAILS

$Gd_{1-x}Ca_xMnO_3$ thin films with a thickness of approximately 100 nm were deposited on $5 \times 5 \times 0.5$ mm^3 (100) $SrTiO_3$ (Crystal GmbH) substrates by pulsed laser deposition using $\lambda = 308$ nm XeCl-laser. The pulse duration was 25 ns, repetition rate 5 Hz, laser fluence 2 J/cm^2, and the pressure of flowing oxygen in the chamber 0.175 Torr. Each sample was deposited using 1500 pulses. The films were grown at 700 °C with *in situ* postannealing treatment of 10 min in atmospheric oxygen pressure. The films were made from deposition targets which were fabricated for the whole calcium range in increments of 0.1 and for concentrations $x = 0.85$ and $x = 0.95$.[25] The grown films were verified to be well-crystallized and epitaxially textured by X-ray diffraction (XRD). The elemental compositions of the samples were verified using energy-dispersive spectroscopy, which showed compositions similar to the nominal values and no systematic deviation.[26] More details on the fabrication process and XRD analysis can be found in refs 27 and 28.

The Al/GCMO/Au RS devices were made by depositing 0.5 mm diameter metal electrodes on top of the films using room-temperature Ar-ion DC sputtering. Wiring was done with a wedge wire bonder using a 40 μm diameter Al wire. The separation distance between the electrodes was approximately 200 μm. The reproducibility of the RS was confirmed by testing multiple thin-film devices made on separate substrates. The characteristics were found to be consistently similar.

Electrical measurements were performed in a planar configuration as schematized in the inset of Figure 1 using a Keithley 2614b sourcemeter. The $I(V)$ loops were measured by sweeping the voltage in a sequence of steps $0 \rightarrow V_{max} \rightarrow -V_{min} \rightarrow 0$ with logarithmic amplitude progression, 100 ms step width, and a 100 ms low-voltage read between each step. Each room-temperature loop measurement was repeated 50 times in order to confirm the stability of the RS device. The voltage amplitudes for inducing high resistance state (HRS) and low resistance state (LRS) were chosen to give maximum switching ratio without damaging the device. The voltages represent extremes, and the optimal values for applications could be lower. Datapoints were measured during and after the writing pulse. The low-voltage current read was set at 450 mV, which was determined to be in the Ohmic region for all calcium concentrations.

RESULTS AND DISCUSSION

The fabricated devices were designed to have only one active interface. This was achieved by using gold and aluminum electrodes. The gold interface does not contribute to the switching and forms an Ohmic interface with GCMO (Figures 1 and 2). Similarly, when Kelvin probe measurements are done on the bulk of the GCMO thin film, the conduction is linear and the switching is not present, narrowing the switching phenomenon to the vicinity of the aluminum interface.

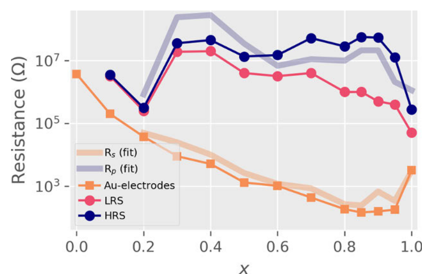

Figure 2. Resistance values for GCMO with Ohmic interfaces (Au electrodes) and Al interfaces (HRS and LRS) over the calcium substitution range x at room temperature. R_s and R_p show results from the conduction model fit (Figure 6 inset); R_s coincides with the Ohmic interface, and R_p coincides with the HRS.

The aluminum electrode forms a rectifying AlO_x layer and depletes the perovskite structure of GCMO from oxygen in the region near the interface (Figure 1 inset). The effects of the interface layer and oxygen depletion compound create an insulating interface. The extent of these effects can be modulated by applying an electric field to the device, which moves oxygen vacancies in and out of the interface depending

https://doi.org/10.1021/acsami.1c02963
ACS Appl. Mater. Interfaces 2021, 13, 18365−18371

on the polarity of the field. The movement of oxygen vacancies modifies the AlO_x layer and the oxygen deficiency level of the interfacial GCMO, which leads to nonvolatile hysteresis in the $I(V)$ properties.[22] Both the AlO_x layer and the formation of oxygen-deficient perovskite region have been observed in other manganite oxides.[24,29−32]

The switching in the devices is bipolar, where the high and low resistive states can be achieved by the application of opposite voltage polarities, similar to what has been reported for other manganite compounds.[1,17,22,24,33−36] The voltage amplitudes for RS are asymmetrical, and the transition to the negative polarity-induced HRS happens at a lower amplitude than the positive polarity-induced LRS transition. The pristine state of the devices is close to the LRS. The switching between HRS and LRS happens gradually, which makes it possible to program intermediate states. The switching in the devices does not require a high-field forming step or current limitation, contrary to many other RS materials.

Effect of Calcium Doping. The calcium substitution x greatly affects both the bulk and RS properties of the GCMO (Figure 2). The Au interface remains Ohmic over the whole substitution range and does not contribute to the switching. The resistivity of the Au interface is lower at higher x, with the minimum at x = 0.85. The resistance values of the Au interface coincide with the existing four-point measurements on GCMO thin films.[26]

The averages of 50 stable $I(V)$ loops of the Al interface as a function of calcium substitution level x are shown in Figure 3

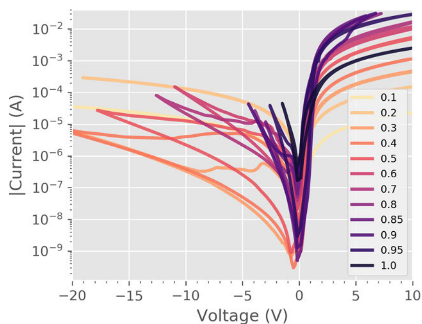

Figure 3. Averages of 50 repeated $I(V)$ loops for each calcium substitution level. Required switching voltages decrease at higher x, and the switching becomes more asymmetric.

and the corresponding switching ratios are shown in Figure 5. The switching ratio is defined as the ratio of stable minimum and maximum resistances measured at 450 mV, which is in the linear region and below the switching threshold for all concentrations. The switching is linked to the nonlinearity of the Al interface, since below x = 0.4, the samples show nearly Ohmic behavior and the switching is weak.

The nonvolatile bipolar RS is present in the range $0.4 < x < 0.95$, and the switching properties peak in the range $0.7 < x < 0.95$. The concentrations with a low x have high bulk resistivity and require large voltage amplitudes to induce switching. The required switching voltages decrease, and the asymmetry in switching voltages increases at substitution levels above x = 0.7.

The optimal calcium concentration for RS was found to be x = 0.85, which is the point where the maximum HRS resistance,

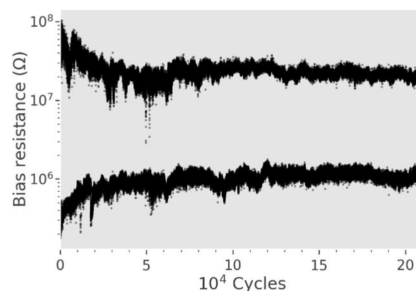

Figure 4. Device endurance of the calcium substitution x = 0.85 over 2×10^5 repeated alternating HRS and LRS pulses. The reading was done between the pulses at the Ohmic region with 450 mV voltage amplitude.

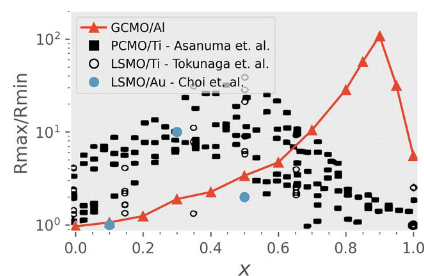

Figure 5. Switching ratio over x for Al/GCMO, Ti/PCMO,[24] Ti/LSMO,[37] and Au/LSMO.[38] The ratio for GCMO was determined from after-pulse measurements of switching loops at 450 mV, where the samples were Ohmic. Results for Ti/LSMO reprinted with permission from[37] Copyright 2006 AIP publishing. Results for Ti/PCMO reprinted with permission from[24] Copyright 2009 American Physical Society. Results for Au/LSMO reprinted with permission from[38] Copyright 2013 Elsevier.

the lowest switching voltages, and the lowest bulk resistivity are reached (Figures 2 and 3). The optimal concentration of x = 0.85 was also confirmed to withstand over 2×10^5 repeated cycles between HRS and LRS (Figure 4). The HRS remains above 10^7 Ω in all switching samples, which is beneficial in reducing the sneak-path currents in crossbar arrays, although full mitigation requires additional measures.[39]

The range of calcium substitution where nonvolatile switching is present coincides with changes in the magnetic properties.[26] The phase diagram has a gradual transition from insulating to metallic state (where the derivative of resistivity with respect to temperature is positive), which begins at x = 0.5 and ends at a region between x = 0.95 and x = 1.0, after which the bulk becomes insulating at x = 1.0. The conditions for magnetic charge ordering also set in at x = 0.4 and disappear approximately at x = 0.7, with effect being the strongest at half-doping.

Other Manganites. In order to highlight the differences between GCMO and other manganite materials, the switching ratios obtained from Al/GCMO over the calcium concentration range x were compared with other studies on manganites (Figure 5). The switching ratio was used in the comparison, since absolute values, such as resistances and

https://doi.org/10.1021/acsami.1c02963
ACS Appl. Mater. Interfaces 2021, 13, 18365−18371

threshold voltages, depend on the size and geometry of the device.

The other materials used in the comparison were Ti/LSMO,[37] Au/LSMO,[38] and Ti/PCMO.[24] The comparison was made against studies which included a series of devices made with different calcium concentrations, and this allowed the determination of the optimal x for each material/electrode combination. The authors of the Ti/LSMO study point out that the Al switching in LSMO is similar to the Ti switching with a slightly lesser switching ratio.[37]

The behavior of the GCMO is different from the LSMO and PCMO samples. What can be seen is that the optimal ratio is in a different part of the phase diagram. While LSMO and PCMO have the maximum at half-doping, the optimal region for the GCMO is at $x = 0.9$, a composition where the other materials do not show switching at all. This is remarkable since the compared materials share similar structural and magnetic properties, and the physical mechanism behind the RS process has been established as universal for the family of Mn-based devices.[1,22,40]

RS in PCMO-based devices has been extensively studied, and most works tend to agree that a moderate hole-carrier concentration of manganites is a prerequisite for the RS and that heavy hole doping suppresses the effect.[24] Our results on GCMO indicate that we cannot generalize this conclusion to the whole manganite family-based devices. This unexpected result demonstrates that the understanding of the physics beneath this phenomenon is still incomplete, and RS materials are being neglected due to their similarity to those already reported.

Conduction Model. The effects of x in the RS and conduction properties were studied in more detail by analyzing the conduction mechanism from the measured $I(V)$ curves. The quantity $\gamma = d(\ln(|I|))/d(\ln(|V|))$ was utilized to analyze changes in the conduction exponent. Different nonlinear (NL) elements and their combinations[41] produce distinct $\gamma(V^{1/2})$ relations, which can be used to differentiate between different conduction models. An Ohmic interface ($I \propto V$) will result in a constant $\gamma = 1$, while a space-charge limited conduction ($I \propto V^2$) dominated interface will have a constant of $\gamma = 2$. Conduction mechanisms that have an exponential dependence between current and voltage, such as Poole−Frenkel (PF) and Schottky, will present a straight line which will only differ in the y-intercept value (0 for Schottky and 1 for PF).[42]

However, since the electric transport in our devices is not dominated by a single conduction mechanism, $\gamma(V^{1/2})$ will take on varying shapes (Figure 6) due to different dominant conduction mechanisms over the voltage range. The positive polarity has a peak-shaped γ-dependence in both HRS and LRS resulting from an interplay of PF and Ohmic conduction mechanisms. The γ-dependence of the negative polarity has two different modes of conduction depending on the resistive state. The change from LRS to HRS in the negative polarity γ initially mirrors the positive polarity, until the transition to HRS begins. In the negative HRS, the γ-relation changes into a Schottky-like conduction with a constant slope and a y-intercept of approximately 0. The simultaneous presence of both Schottky and PF conduction models has previous support.[43] The negative polarity was not utilized in the final model analysis due to the highly rectifying interface and the stochastic transition from PF to Schottky-like conduction, which is difficult to reproduce using physical models.[44]

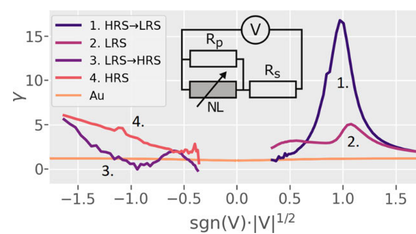

Figure 6. Voltage sweep $\gamma(V^{1/2})$ curves of Ohmic Au interfaces and Al/GCMO/Au for $x = 0.85$. RS and nonlinear conduction happen only when an Al interface is present. The inset shows the equivalent circuit used in model fits, which consists of a NL element with series and parallel linear resistances R_s and R_p.

In order to properly explain the peak-shaped $\gamma(V^{1/2})$ behavior in the positive polarity of GCMO, a more complex circuit needs to be introduced. The positive polarity curves of Al/GCMO can be reproduced by creating an equivalent circuit consisting of a NL conduction element with Ohmic series and parallel resistances R_s and R_p (Figure 6). The NL element representing the contribution of the Al/GCMO interface can be thought of as a bulk-limited PF conduction in series with a Schottky diode.[43] The circuit can be used in the positive polarity, where the PF-based conduction dominates. A similar peak shape has also been seen in other perovskite compounds, such as PCMO[14] and LSCO.[45]

The model can be expressed as an implicit equation for I and V at constant temperature

$$I = A(V - I \cdot R_s)[\exp(B\sqrt{V - I \cdot R_s})] + \frac{V - I \cdot R_s}{R_p} \tag{1}$$

with $A = \tilde{A}_{PF} \exp\left(-\frac{q\phi}{k_B T}\right)$ and $B = \frac{q^{3/2}}{k_B T \sqrt{\pi \epsilon_0 \epsilon' d}}$, where T is the temperature, $\tilde{A}_{PF}$ is a normalization factor which also depends on temperature, q is the electron charge, ϕ is the trap energy level, k_B is the Boltzmann constant, ϵ_0 is the vacuum permittivity, ϵ' is the real part of the dielectric constant, d is the distance where the voltage drop is produced, R_s is the series resistance, and R_p is the parallel resistance.[42] The series resistance R_s represents the Ohmic RS-state dependent contribution from the oxide layer and the bulk, that is, R_s is high in HRS and low in LRS. The parallel resistance R_p represents the Ohmic contribution from regions of the interface which do not contribute to the switching; an R_p higher than the bulk resistivity is a requirement for RS.

Model Fit. The model makes it possible to separate Ohmic components from the positive $I(V)$ curve and examine the underlying PF conduction, which combined with temperature measurements gives access to the PF trap energy level ϕ.

The fitting for free parameters A, B, R_s, and R_p of eq 1 was done by numerically solving the implicit equation and iteratively minimizing the error with respect to the experimental data by using a combination of basin-hopping and Broyden−Fletcher−Goldfarb−Shanno algorithm. The data used for the fits was the nonrectifying positive polarity in the HRS. The HRS was used because there is a continuum of possible states between HRS and LRS, out of which HRS represents the maximal difference from the nonswitching Ohmic interface (Figure 6).

https://doi.org/10.1021/acsami.1c02963
ACS Appl. Mater. Interfaces 2021, 13, 18365−18371

The room-temperature fits were made for samples in the range $0.1 \le x \le 1.0$. The model coincided with the experimental data at room temperature, reproducing the $I(V)$ relations for voltages above 400 mV (Figure 7). The series resistances R_s coincide with the resistance of GCMO with Ohmic electrodes (Table 1) (Figure 2). The parallel resistances R_p were of the same order of magnitude as the HRS states in switching Al/GCMO interfaces (Figure 2).

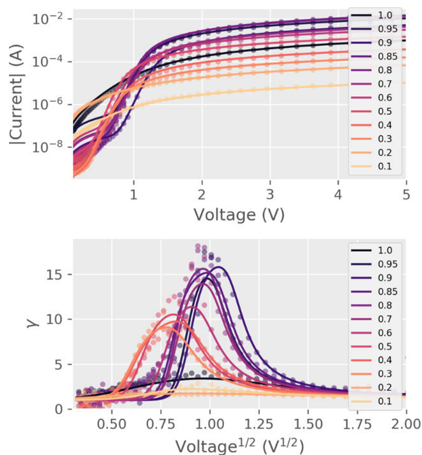

Figure 7. Fitted and experimental values for $\gamma(V^{1/2})$ and $I(V)$ over the calcium range at room temperature. The transition becomes more abrupt at higher substitutions.

Table 1. Table with Parameters R_s, R_p, and ϕ from the Model Fit and Experimentally Measured Resistances R_{Au} from Symmetric Au Interfaces at Room Temperature

x	R_s (Ω)	R_p (Ω)	ϕ (eV)	R_{Au} (Ω)
0.0				3.7×10^6
0.1	3.6×10^5	3.7×10^6		1.9×10^5
0.2	4.9×10^4	8.3×10^5		3.7×10^4
0.3	2.4×10^4	2.4×10^8		8.9×10^3
0.4	1.0×10^4	2.8×10^8	1.00	5.0×10^3
0.5	2.6×10^3	3.5×10^7	0.99	1.3×10^3
0.6	1.1×10^3	6.8×10^6	0.98	1.0×10^3
0.7	8.4×10^2	1.1×10^7	0.85	4.2×10^2
0.8	2.6×10^2	9.9×10^6	0.30	1.8×10^2
0.85	2.4×10^2	2.1×10^7	0.44	1.4×10^2
0.9	6.7×10^2	2.1×10^7	0.67	1.5×10^2
0.95	3.3×10^2	2.0×10^6	0.70	1.7×10^2
1.0	2.9×10^3	1.1×10^6		3.1×10^3

Temperature Dependence. We determined the PF trap energy level ϕ by measuring the $I(V)$ curves as a function of temperature. The measurements were performed in a physical property measurement system. The samples were set to the HRS at 300 K, after which they were measured over the temperature range with the Keithley 2614b sourcemeter. The $I-V$ measurements were run using a maximum voltage amplitude, which did not induce switching at any temperature. The measurements consisted of initially going to the maximum temperature of 350 K, after which the temperature was lowered to 250 K in steps of 25 K. Experimental data from each temperature measurement was fitted to the conduction model (Figure 8). Fitting for ϕ was performed for concentrations which had RS and linear Arrhenius relation $\ln(A) - 1/T$; this corresponded to the x range from 0.4 to 0.95 (Table 1) (Figure 9).

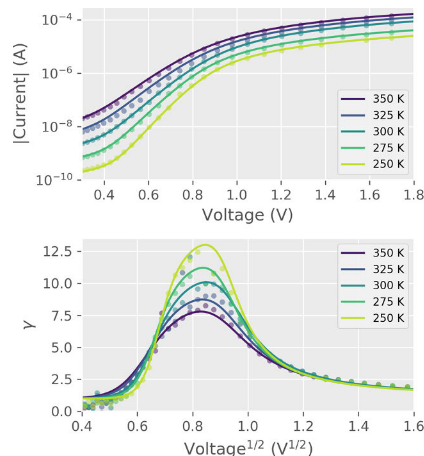

Figure 8. Fitted and experimental values for $\gamma(V^{1/2})$ and $I(V)$ for x = 0.4 over the temperature range.

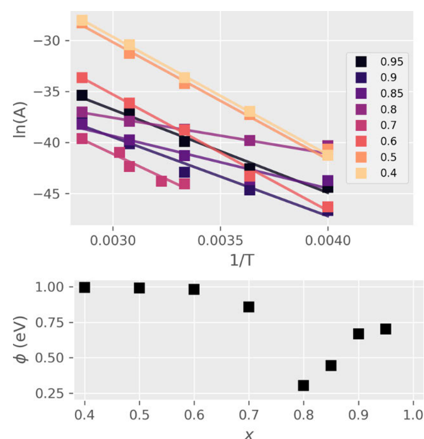

Figure 9. Arrhenius plots and PF trap energy levels ϕ from the model fit. The substitution values x where trap energy level ϕ deviates from 1 eV also correspond to good RS properties.

The trap energy level for x in the range from 0.4 to 0.6 is close to 1 eV. From 0.6 to 0.8, the value of ϕ decreases to 0.3 eV and begins to increase again at higher x. The lowest point of ϕ at x = 0.8 coincides with the region of highest switching ratio (Figure 5), which suggests that the magnitude of RS is related to changes in the trap energy level. The minimum also has the lowest threshold voltage needed for inducing HRS to

https://doi.org/10.1021/acsami.1c02963
ACS Appl. Mater. Interfaces 2021, 13, 18365−18371

LRS transition and corresponds to the lowest point in the bulk resistance of GCMO (Table 1) (Figure 2). The RS in Al/GCMO seems to favor low bulk resistance and shallow traps at the active interface. These findings could be useful as heuristics for finding optimal RS parameters in other similar materials.

CONCLUSIONS

In summary, we have demonstrated that the RS effect is present in the $Al/Gd_{1-x}Ca_xMnO_3$-interface at certain calcium substitution values. The devices showed bipolar switching when combined with an asymmetric combination of Ohmic interface and a rectifying Al interface. The optimum concentration for RS with operating voltages and switching ratio taken into account was determined to be near $x = 0.9$. This conclusion completely opposes the behavior in similar manganites, where the optimal value is close to half-doping and no switching is observable at high substitution values.

The positive polarity of Al/GCMO was found to obey PF conduction with linear series and parallel resistances and the negative polarity HRS conduction was Schottky-like. The temperature measurements showed changes in the PF trap energy ϕ in the range from 0.3 to 1.00 eV. The lower ϕ values were associated with good RS properties, high switching ratio, and low bulk resistivity.

These RS studies show that the GCMO-based devices are on par with the other manganite-based RS materials and open the question on whether the other unexplored members of the manganite family could be used for RS as well. The next step in the GCMO-based memristor devices is to use the knowledge gained from our research to optimize the devices up to their fullest potential and to study their properties from the neuromorphics standpoint. This will lead to the development of new technologies in the form of more robust and energy-efficient memory devices and neuromorphic circuits.

AUTHOR INFORMATION

Corresponding Author

Ville Lähteenlahti — *Wihuri Physical Laboratory, Department of Physics and Astronomy, University of Turku, FI-20014 Turku, Finland;* orcid.org/0000-0003-2491-407X; Email: visalah@utu.fi

Authors

Alejandro Schulman — *Wihuri Physical Laboratory, Department of Physics and Astronomy, University of Turku, FI-20014 Turku, Finland*

Azar Beiranvand — *Wihuri Physical Laboratory, Department of Physics and Astronomy, University of Turku, FI-20014 Turku, Finland*

Hannu Huhtinen — *Wihuri Physical Laboratory, Department of Physics and Astronomy, University of Turku, FI-20014 Turku, Finland*

Petriina Paturi — *Wihuri Physical Laboratory, Department of Physics and Astronomy, University of Turku, FI-20014 Turku, Finland*

Complete contact information is available at: https://pubs.acs.org/10.1021/acsami.1c02963

Notes

The authors declare no competing financial interest.

ACKNOWLEDGMENTS

This work was financially supported by the Academy of Finland project 308285. V. L. acknowledges support from the University of Turku Graduate School (UTUGS). The authors also acknowledge the Jenny and Antti Wihuri Foundation for financial support.

REFERENCES

(1) Sawa, A. Resistive Switching in Transition Metal Oxides. *Mater. Today* **2008**, *11*, 28−36.

(2) Yoon, J. H.; Han, J. H.; Jung, J. S.; Jeon, W.; Kim, G. H.; Song, S. J.; Seok, J. Y.; Yoon, K. J.; Lee, M. H.; Hwang, C. S. Highly Improved Uniformity in the Resistive Switching Parameters of TiO_2 Thin Films by Inserting Ru Nanodots. *Adv. Mater.* **2013**, *25*, 1957.

(3) Kwon, D.-H.; Kim, K. M.; Jang, J. H.; Jeon, J. M.; Lee, M. H.; Kim, G. H.; Li, X.-S.; Park, G.-S.; Lee, B.; Han, S.; Kim, M.; Hwang, C. S. Atomic Structure of Conducting Nanofilaments in TiO_2 Resistive Switching Memory. *Nat. Nanotechnol.* **2010**, *5*, 148.

(4) Shi, Y.; Liang, X.; Yuan, B.; Chen, V.; Li, H.; Hui, F.; Yu, Z.; Yuan, F.; Pop, E.; Wong, H.-S. P.; Lanza, M. Electronic Synapses Made of Layered Two-Dimensional Materials. *Nat. Electron.* **2018**, *1*, 458.

(5) Ishibe, T.; Kurokawa, T.; Naruse, N.; Nakamura, Y. Resistive Switching at the High Quality metal/insulator Interface in $Fe_3O_4/SiO_2/\alpha$-$FeSi_2$/Si Stacking Structure. *Appl. Phys. Lett.* **2018**, *113*, 141601.

(6) Ishibe, T.; Maeda, Y.; Terada, T.; Naruse, N.; Mera, Y.; Kobayashi, E.; Nakamura, Y. Resistive Switching Memory Performance in Oxide Hetero-Nanocrystals With Well-Controlled Interfaces. *Sci. Technol. Adv. Mater.* **2020**, *21*, 195.

(7) Zahoor, F.; Azni Zulkifli, T. Z.; Khanday, F. A. Resistive Random Access Memory (RRAM): an Overview of Materials, Switching Mechanism, Performance, Multilevel Cell (MLC) Storage, Modeling, and Applications. *Nanoscale Res. Lett.* **2020**, *15*, 90.

(8) Lee, D.; Hwang, H. Neuro-inspired Computing Using Resistive Synaptic Devices. *$Pr_{0.7}Ca_{0.3}MnO_3$ (PCMO)-Based Synaptic Devices*; Springer, 2017; pp 53−71.

(9) Lashkare, S.; Chouhan, S.; Chavan, T.; Bhat, A.; Kumbhare, P.; Ganguly, U. PCMO RRAM for Integrate-And-Fire Neuron in Spiking Neural Networks. *IEEE Electron Device Lett.* **2018**, *39*, 484−487.

(10) Li, C.; et al. Analogue Signal and Image Processing With Large Memristor Crossbars. *Nat. Electron.* **2018**, *1*, 52.

(11) Yao, P.; Wu, H.; Gao, B.; Tang, J.; Zhang, Q.; Zhang, W.; Yang, J. J.; Qian, H. Fully Hardware-Implemented Memristor Convolutional Neural Network. *Nature* **2020**, *577*, 641−646.

(12) Gao, L.; Chen, P.-Y.; Yu, S. Demonstration of Convolution Kernel Operation on Resistive Cross-Point Array. *IEEE Electron Device Lett.* **2016**, *37*, 870−873.

(13) Park, S. et al. *RRAM-Based Synapse for Neuromorphic System with Pattern Recognition Function, 2012*; International Electron Devices Meeting, 2012; pp 10−12.

(14) Lähteenlahti, V.; Schulman, A.; Huhtinen, H.; Paturi, P. Transport Properties of Resistive Switching in $Ag/Pr_{0.6}Ca_{0.4}MnO_3/Al$ Thin Film Structures. *J. Alloys Compd.* **2019**, *786*, 84−90.

(15) Jang, J.-W.; Park, S.; Burr, G. W.; Hwang, H.; Jeong, Y.-H. Optimization of Conductance Change in $Pr_{1-x}Ca_xMnO_3$-based Synaptic Devices for Neuromorphic Systems. *IEEE Electron Device Lett.* **2015**, *36*, 457−459.

(16) Zhao, M.; Gao, B.; Tang, J.; Qian, H.; Wu, H. Reliability of Analog Resistive Switching Memory for Neuromorphic Computing. *Appl. Phys. Rev.* **2020**, *7*, 011301.

(17) Bagdzevicius, S.; Maas, K.; Boudard, M.; Burriel, M. Interface-Type Resistive Switching in Perovskite Materials. *J. Electroceram.* **2017**, *39*, 157−184.

(18) Kanegami, N.; Nishi, Y.; Kimoto, T. Unique Resistive Switching Phenomena Exhibiting both Filament-Type and Interface-Type Switching in $Ti/Pr_{0.7}Ca_{0.3}MnO3$- δ/Pt ReRAM Cells. *Appl. Phys. Lett.* **2020**, *116*, 013501.

(19) Park, S.; Sheri, A.; Kim, J.; Noh, J.; Jang, J.; Jeon, M.; Lee, B.; Lee, B.; Lee, B.; Hwang, H.-J. *Neuromorphic Speech Systems Using Advanced Reram-Based Synapse, 2013*; IEEE IEDM, 2013; pp 25−26.
(20) Miranda, E.; Román Acevedo, W.; Rubi, D.; Lüders, U.; Granell, P.; Suñé, J.; Levy, P. Modeling of the Multilevel Conduction Characteristics and Fatigue Profile of $Ag/La_{1/3}Ca_{2/3}MnO_3/Pt$ Structures Using a Compact Memristive Approach. *J. Appl. Phys.* **2017**, *121*, 205302.
(21) Ortega-Hernandez, R.; Coll, M.; Gonzalez-Rosillo, J.; Palau, A.; Obradors, X.; Miranda, E.; Puig, T.; Suñe, J. Resistive Switching in $CeO_2/La_{0.8}Sr_{0.2}MnO_3$ Bilayer for Non-Volatile Memory Applications. *Microelectron. Eng.* **2015**, *147*, 37−40.
(22) Rozenberg, M.; Sanchez, M. J.; Weht, R.; Acha, C.; Gomez-Marlasca, F.; Levy, P. Mechanism for Bipolar Resistive Switching in Transition-Metal Oxides. *Phys. Rev. B: Condens. Matter Mater. Phys.* **2010**, *81*, 115101.
(23) Lee, D.; Park, J.; Moon, K.; Jang, J.; Park, S.; Chu, M.; Kim, J.; Noh, J.; Jeon, M.; Lee, B. H.; Lee, B.; Lee, B.-G.; Hyunsang, H. *Oxide Based Nanoscale Analog Synapse Device for Neural Signal Recognition System, 2015*; IEEE International Electron Device Meeting, 2015; pp 4−7.
(24) Asanuma, S.; Akoh, H.; Yamada, H.; Sawa, A. Relationship Between Resistive Switching Characteristics and Band Diagrams of $Ti/Pr_{1-x}Ca_xMnO_3$ Junctions. *Phys. Rev. B: Condens. Matter Mater. Phys.* **2009**, *80*, 235113.
(25) Beiranvand, A.; Tikkanen, J.; Huhtinen, H.; Paturi, P. Electronic and Magnetic Phase Diagram of Polycrystalline $Gd_{1-x}Ca_xMnO_3$ Manganites. *J. Alloys Compd.* **2017**, *720*, 126−130.
(26) Schulman, A.; Beiranvand, A.; Lähteenlahti, V.; Huhtinen, H.; Paturi, P. Appearance of Glassy Ferromagnetic Behavior in $Gd_{1-x}Ca_xMnO_3$ ($0 < x < 1$) Thin Films: A Revised Phase Diagram. *J. Magn. Magn. Mater.* **2020**, *498*, 166149.
(27) Paturi, P.; Tikkanen, J.; Huhtinen, H. Room Temperature Charge-Ordered Phase in $Gd_{0.6}Ca_{0.4}MnO_3$ and $Sm_{0.6}Ca_{0.4}MnO_3$ Thin Films. *J. Magn. Magn. Mater.* **2017**, *432*, 164−168.
(28) Beiranvand, A.; Tikkanen, J.; Huhtinen, H.; Paturi, P. Metamagnetic Transition and Spin Memory Effect in Epitaxial $Gd_{1-x}Ca_xMnO_3$ ($0 < x < 1$) Thin Films. *J. Magn. Magn. Mater.* **2019**, *469*, 253−258.
(29) Liao, Z. L.; Wang, Z. Z.; Meng, Y.; Liu, Z. Y.; Gao, P.; Gang, J. L.; Zhao, H. W.; Liang, X. J.; Bai, X. D.; Chen, D. M. Categorization of Resistive Switching of metal-$Pr_{0.7}Ca_{0.3}MnO_3$-metal Devices. *Appl. Phys. Lett.* **2009**, *94*, 253503.
(30) Yang, R.; Li, X. M.; Yu, W. D.; Liu, X. J.; Cao, X.; Wang, Q.; Chen, L. D. Multiform Resistance Switching Effects in the $Al/La_{0.7}Ca_{0.3}MnO_3/Pt$ Structure. *Electrochem. Solid State Lett.* **2009**, *12*, H281−H283.
(31) Seong, D.-J.; Hassan, M.; Choi, H.; Lee, J.; Yoon, J.; Park, J.-B.; Lee, W.; Oh, M.-S.; Hwang, H. Resistive-Switching Characteristics of $Al/Pr_{0.7}Ca_{0.3}MnO_3$ for Nonvolatile Memory Applications. *IEEE Electron Device Lett.* **2009**, *30*, 919−921.
(32) Nakamura, T.; Homma, K.; Tachibana, K. Thin Film Deposition of Metal Oxides in Resistance Switching Devices: Electrode Material Dependence of Resistance Switching in Manganite Films. *Nanoscale Res. Lett.* **2013**, *8*, 76.
(33) Baek, K.; Park, S.; Park, J.; Kim, Y.-M.; Hwang, H.; Oh, S. H. In Situ Tem Observation on the Interface-Type Resistive Switching by Electrochemical Redox Reactions at a TiN/PCMO Interface. *Nanoscale* **2017**, *9*, 582−593.
(34) Kramer, T.; Scherff, M.; Mierwaldt, D.; Hoffmann, J.; Jooss, C. Role of Oxygen Vacancies for Resistive Switching in Noble Metal Sandwiched $Pr_{0.67}Ca_{0.33}MnO_{3}$-$\delta$. *Appl. Phys. Lett.* **2017**, *110*, 243502.
(35) Seong, T.-G.; Lee, B.-S.; Choi, K. B.; Kweon, S.-H.; Kim, B. Y.; Jung, K.; Moon, J. W.; Lee, K. J.; Hong, K.; Nahm, S. Unipolar Resistive Switching Properties of Amorphous $Pr_{0.7}Ca_{0.3}MnO_3$ Films Grown on a $Pt/Ti/SiO_2/Si$ Substrate. *Curr. Appl. Phys.* **2014**, *14*, 538−542.
(36) Toyoda, S.; Namiki, T.; Sakai, E.; Nakata, K.; Oshima, M.; Kumigashira, H. Chemical-State-Resolved Depth Profiles of $Al/Pr_{0.7}Ca_{0.3}MnO_3$ Stacked Structures for Application in Resistive Switching Devices. *J. Appl. Phys.* **2013**, *114*, 243711.
(37) Tokunaga, Y.; Kaneko, Y.; He, J. P.; Arima, T.; Sawa, A.; Fujii, T.; Kawasaki, M.; Tokura, Y. Colossal Electroresistance Effect at Metal electrode/$La_{1-x}Sr_{1+x}MnO_4$ Interfaces. *Appl. Phys. Lett.* **2006**, *88*, 223507.
(38) Choi, S. G.; Lee, H.-S.; Choi, H.; Chung, S.-W.; Park, H.-H. The Effect of Sr Concentration on Resistive Switching Properties of $La_{1-x}Sr_xMnO_3$ Films. *Thin Solid Films* **2013**, *529*, 352−355.
(39) Zidan, M. A.; Fahmy, H. A. H.; Hussain, M. M.; Salama, K. N. Memristor-Based Memory: The Sneak Paths Problem and Solutions. *Microelectron. J.* **2013**, *44*, 176−183.
(40) Waser, R.; Dittmann, R.; Staikov, G.; Szot, K. Redox-Based Resistive Switching Memories - Nanoionic Mechanisms, Prospects, and Challenges. *Adv. Mater.* **2009**, *21*, 2632−2663.
(41) Chiu, F.-C. A Review on Conduction Mechanisms in Dielectric Films. *Adv. Mater. Sci. Eng.* **2014**, *2014*, 578168.
(42) Acha, C. Graphical Analysis of Current-Voltage Characteristics in Memristive Interfaces. *J. Appl. Phys.* **2017**, *121*, 134502.
(43) Lau, W. S. An Extended Unified Schottky-Poole-Frenkel Theory to Explain the Current-Voltage Characteristics of Thin Film Metal-Insulator-Metal Capacitors With Examples for Various High-K Dielectric Materials. *ECS J. Solid State Sci. Technol.* **2012**, *1*, N139.
(44) Aguirre, F. L.; Pazos, S. M.; Palumbo, F.; Suñé, J.; Miranda, E. Application of the Quasi-Static Memdiode Model in Cross-Point Arrays for Large Dataset Pattern Recognition. *IEEE Access* **2020**, *8*, 202174−202193.
(45) Acha, C.; Schulman, A.; Boudard, M.; Daoudi, K.; Tsuchiya, T. Transport Mechanism Through Metal-Cobaltite Interfaces. *Appl. Phys. Lett.* **2016**, *109*, 011603.

E. Miranda & V. Lähteenlahti & H. Huhtinen & A. Schulman & P. Paturi

Compact modeling and SPICE simulation of GCMO-based resistive switching devices

In peer-review, IEEE Transactions on Nanotechnology, 21, 2022, 285–288

IV

Compact Modeling and SPICE Simulation of GCMO-Based Resistive Switching Devices

E. Miranda, *Senior Member, IEEE*, V. Lähteenlahti, H. Huhtinen, A. Schulman, and P. Paturi

***Abstract*—This letter reports a compact behavioral model for the hysteretic conduction characteristics of Al/$Gd_{0.1}Ca_{0.9}MnO_3$(GCMO)/Au resistive switching devices suitable for SPICE simulations. The devices are nonvolatile, forming-less, compliance-free, and self-rectifying multistate memristive structures that make them of maximum interest for neuromorphic computing and memory applications. The proposed model relies on two coupled equations, one for the electron transport and a second one for the vacancy displacement. First, the fixed and variable current components that contribute to the total electronic flow are identified and modelled. They are tunneling- and diode-like conduction with series resistance through the sub-oxide layer formed at the GCMO/Al interface in combination with localized soft-breakdown conduction. Second, the memory equation accounts for the reversible movement of vacancies that causes the generation and self-healing of these micro-filaments. Importantly, the proposed model uses a novel approach for solving the internal state of the device based on the so-called generalized hysteron or memory map whose application can be extended to other structures and dynamics in addition to the ones discussed here.**

***Index Terms*—GCMO, memristor, resistive switching**

I. Introduction

PEROVSKITE manganites such as $Pr_{1-x}Ca_xMnO_3$ (PCMO), $La_{1-x}Ca_xMnO_3$ (LCMO), $La_{1-x}Sr_xMnO_3$ (LSMO), and $Gd_{1-x}Ca_xMnO_3$(GCMO) are considered good candidates as active layers in memristive devices [1-5]. In general, they exhibit good reproducibility, are forming-less and compliance-free, and allow precise control of the resistance state, features of utmost importance for neuromorphic and memory applications [6,7]. As expected, the electrical behavior of these materials largely depends on the substitution range x. In this letter, we focus the attention on GCMO devices with x=0.9, which has been demonstrated to provide the highest resistance window [8]. It has also been observed that the Au and Al metal electrodes are associated with ohmic and rectifying contacts with the GCMO layer, respectively [8]. The devices exhibit asymmetrical switching voltages (Fig. 1a) and generation of micro-filaments (Fig. 1b) in the AlO_x barrier (Fig. 1c) at the transition voltage V_T≈3V. The displacement of oxygen vacancies enables the formation and breakdown of these micro-filaments providing the nonvolatile memory effect [9].

This work was supported in part by the Ministerio de Ciencia e Innovación, Spain (TEC2017-84321-C4-4-R), the Academy of Finland (Project 308285), and The Nokia Foundation, Finland.

E. Miranda is with the Departament d'Enginyeria Electrònica, Universitat Autònoma de Barcelona, 08193, Cerdanyola del Valles, Spain.(e-mail: enrique.miranda@uab.cat).

V. Lähteenlahti, H. Huhtinen, A. Schulman, and P. Paturi are with the Wihuri Physical Laboratory, Department of Physics and Astronomy, University of Turku, FI-20014, Turku, Finland. (e-mail: petriina.paturi@utu.fi).

A. Schulman is also with the International Iberian Nanotechnology Laboratory, INL, Av. Mestre José Veiga s/n, 4715-330, Braga, Portugal. (e-mail: alejandro.schulman@utu.fi).

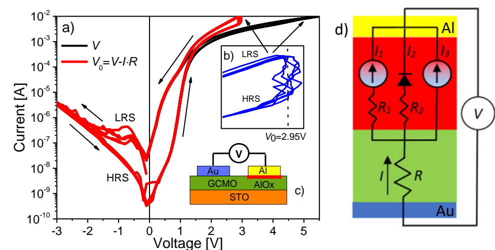

Fig. 1. a) Experimental *I-V* curve (R=265 Ω). b) Detail of the current increase at V_T. c) Structure of the investigated devices. d) Equivalent circuit model.

The aim of this letter is to show that a Spice compact model for this complex behavior is feasible. To this end, in Section II the device fabrication process and measurement details are presented. In Section III, the experimental *I-V* curves are investigated in connection with the model equations. In Section IV, the Spice script for the proposed model is described, ending with the conclusions of this work.

II. Device Fabrication and Measurements

The devices investigated are Al/$Gd_{0.1}Ca_{0.9}MnO_3$(80 nm)/Au structures deposited on $SrTiO_3$ (STO) substrates by pulsed laser deposition (λ=308 nm from a XeCl-laser) [8]. The pulse duration was 25 ns (1500 pulses), with a repetition rate of 5 Hz, laser fluence of 2 J/cm^2, and oxygen pressure of 0.175 Torr. The oxide was grown at 700 °C with *in situ* postannealing treatment of 10 min in atmospheric O_2 pressure. The quality of the film was assessed using X-ray diffraction (XRD) and energy-dispersive spectroscopy. The metal electrodes (0.5 mm diameter) were deposited using room-temperature Ar-ion DC sputtering. The electrical characterization was performed with a Keithley 2614b sourcemeter. The low-voltage current read was set at V_p=450 mV, which corresponds to the linear conduction region.

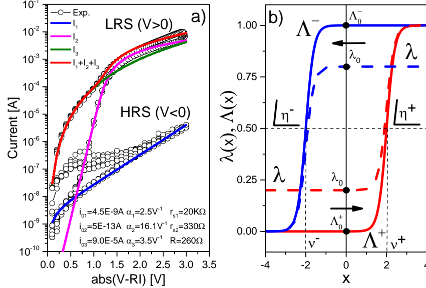

Fig. 2. a) Experimental and model (1-3) *I-V* curves. b) Hysteron (solid line) and minor loop (dashed line) corresponding to (5) and (4), respectively.

III. Model Equations

We start by analyzing the *I-V* curves of our devices. In view of Fig. 2a, the electron transport can be expressed by the following system of equations (see also Fig. 1b):

$$I_1 = I_{01}\sinh\left[\alpha_1\left(V_0 - I_1 R_1\right)\right] \quad (1)$$

$$I_2 = I_{02}\left\{exp\left[\alpha_2\left(V_0 - I_2 R_2\right)\right] - 1\right\} \quad (2)$$

$$I_3 = \lambda\left(V_0\right) I_{03} V_0^{\alpha_3} \quad (3)$$

where $V_0=V\text{-}IR$ and $I=I_1+I_2+I_3$. We associate I_1, I_2, and I_3 with tunneling, Schottky-like, and soft-breakdown conduction in the AlO_x layer, respectively [7-12]. Poole-Frenkel conduction is also a possibility which cannot be ruled out [8]. α_i, I_{0i}, and R_i, i=1,2,3 are fitting parameters. R is the GCMO bulk resistance and it is found from the vertical current increase ocurring at V_T. Notice that while (1) and (2) are independent of the memory state of the device $0\leq\lambda\leq1$, (3) takes into account the modulation of the effective area of the micro-filaments caused by the reversible movement of vacancies. More in general, the method considers the *I-V* curve expressed as $I=f(V)+\lambda(V)\cdot g(V)$ where f and g are two specific functions. λ in (3) is given by the affine transformation of $\Lambda^{\pm}$ [13]:

$$\lambda(x) = \begin{cases} \dfrac{\lambda_0 - 1}{\Lambda_0^+ - 1}\Lambda^+(x) + \dfrac{\Lambda_0^+ - \lambda_0}{\Lambda_0^+ - 1} & \dot{x} \geq 0 \\[2ex] \dfrac{\lambda_0}{\Lambda_0^-}\Lambda^-(x) & \dot{x} < 0 \end{cases} \quad (4)$$

where $\Lambda^{\pm}$ can be any sigmoidal function satisfying $\Lambda^{\pm}(x\rightarrow\infty)=1$ and $\Lambda^{\pm}(x\rightarrow-\infty)=0$. This generates different switching dynamics. $\Lambda_0^{\pm}=\Lambda^{\pm}(0)$ and $\lambda_0=\lambda(0)$. $\dot{x}$ is the derivative of x with respect to time. For the sake of simplicity, in this work, we used the logistic hysteron [14]:

$$\Lambda^{\pm}(x) = \left\{1 + exp\left[-\eta^{\pm}\left(x - v^{\pm}\right)\right]\right\}^{-1} \quad (5)$$

where $\eta^{\pm}$ is the transition rate and $v^{\pm}$ the set/reset parameter. Notice that (5) corresponds to Strukov's window function $\dot{\Lambda} \sim \Lambda(1-\Lambda)$ [15]. (4) generalizes the method proposed in [14] by introducing soft transitions within the hysteron structure. In order to solve the memory state evolution for an arbitrary input signal $V(t)=V_t$, we discretize (4) using $\lambda=\lambda_t$, $\lambda_0=\lambda_{t\text{-}1}$, $\Lambda^{\pm}=\Lambda^{\pm}_t$, and $\Lambda^{\pm}_0=\Lambda^{\pm}_{t\text{-}1}$, so that the current memory state (t) depends on the previous state ($t\text{-}1$) as expected for a Markovian behavior. (1)-(5) constitute a system of non-linear equations that must be solved numerically. This is carried out in Section IV using the Spice simulator.

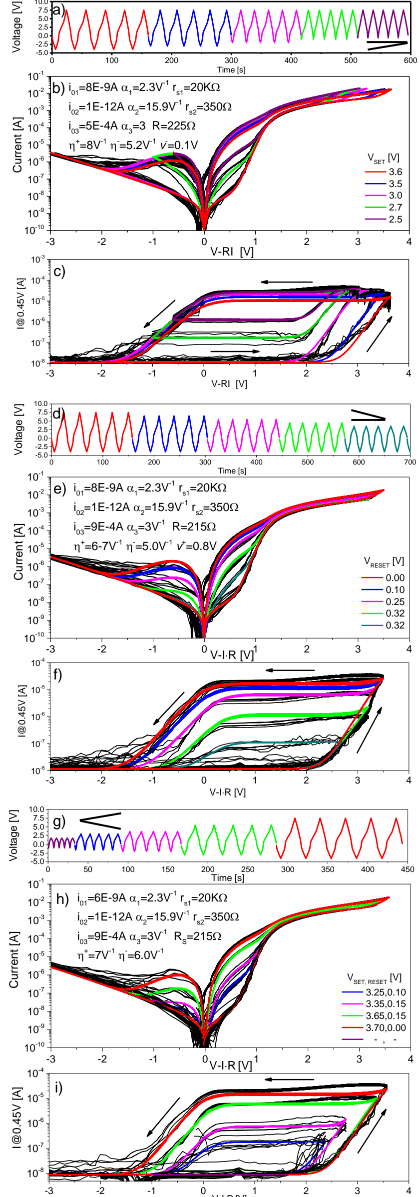

Fig. 3. Experimental and simulation results. *a*), *d*), *g*) illustrate different bipolar applied signals; *b*), *e*), *h*) show the corresponding *I-V* curves; *c*) ,*e*) ,*i*) demonstrate the ability of the model to simulate the read current (*I*@0.45V) as a function of the applied bias. Each loop was performed 5 times.

IV. SPICE IMPLEMENTATION AND SIMULATION RESULTS

This Section thoroughly describes the implementation of the proposed hysteretic conduction model. Experimental (black lines) and simulation (color lines) results obtained for increasing and/or decreasing amplitude voltage signals are presented in Fig. 3. In order to check the robustness of the reported approach, the experimental voltage, and not an ideal sweep, was used as the model input. The model script (Fig. 4a) is written as a subcircuit in the LTspice language [16]. It contains five modular sections which can be modified according to the transport properties and transition dynamics.

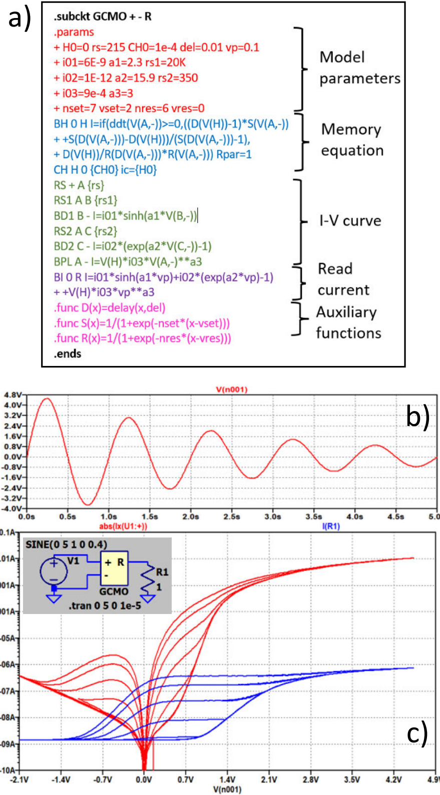

Fig. 4. a) Model script for LTspice. b) Input signal. c) Simulation results for the *I-V* characteristic and the read current at *vp*=0.1V.

While + and – in the subcircuit header refer to the physical terminals of the device, *R* provides the read current. First section in Fig. 4a defines the model parameters. *H0* is the initial memory state, *CH0* the capacitor used to store the initial memory state, *del* the delay parameter used to recall the previous state, and *vp* the read voltage. The second section deals with the discretized memory equation (4), which is represented by a behavioral voltage-controlled current source. The delay function *D* is used to recover the past information. *Rpar* provides an alternative path for the current generator. The third section represents the *I-V* port described by (1)-(3). Notice how the voltage node *V*(*H*), *i.e.* λ, modulates the power-law soft-breakdown current component. The fourth section is optional and calculates the read current at a fixed voltage *vp*. This can be accomplished by duplicating the *I-V* port for a fixed voltage *vp* (as done in Fig. 3) or neglecting the role played by the series resistances (as shown in Fig. 4c). The last section defines the delay function and the hysteron structure (5). For illustrative purposes, Figs. 4b and 4c show the model results for a damped sinusoidal signal generated by the simulator. Figure 4c's inset shows the circuit schematic.

To conclude, this letter reported a simple and compact behavioral model for GCMO-based structures suitable for Spice simulations. The model follows Prof. Chua's approach for memristive devices [17] and it consists in a set of electron transport equations driven by a hysteresis engine. We were able to simulate the experimental *I-V* curves as well as the low-voltage read current using a three-terminal subcircuit.

References

[1] S. Bagdzevicius, K. Maas, M. Boudard, M. Burriel, “Interface-type resistive switching in perovskite materials,” J. Electroceram, vol. 39, pp. 157-184, 2017. DOI: 10.1007/s10832-017-0087-9

[2] V. Lähteenlahti, A. Schulman, H. Huhtinen, P. Paturi, “Transport properties of resistive switching in $Ag/Pr_{0.6}Ca_{0.4}MnO_3/Al$ thin film structures,” J Alloys Compd, vol. 786, pp. 84–90, 2019. DOI: 10.1016/j.jallcom.2019.01.279

[3] J. Jang, S. Park, G. Burr, H. Hwang, Y. Jeong, “Optimization of conductance change in $Pr_{1-x}Ca_xMnO_3$-based synaptic devices for neuromorphic systems,” IEEE Electron Device Lett, vol. 36, pp. 457–459, 2015. DOI: 10.1109/LED.2015.2418342

[4] E. Miranda, W. Román Acevedo, D. Rubi, U. Lüders, P. Granell, J. Suñé, P. Levy, “Modeling of the multilevel conduction characteristics and fatigue profile of $Ag/La_{1/3}Ca_{2/3}MnO_3/Pt$ structures using a compact memristive approach,” J Appl Phys, vol. 121, 205302, 2017. DOI: 10.1063/1.4984051

[5] R. Ortega-Hernandez, M. Coll, J. Gonzalez-Rosillo, A. Palau, X. Obradors, E. Miranda, T. Puig, J. Suñe, “Resistive switching in $CeO_2/La_{0.8}Sr_{0.2}MnO_3$ bilayer for non-volatile memory applications,” Microelectron Eng, vol. 147, pp. 37–40, 2015. DOI: 10.1016/j.mee.2015.04.042

[6] E. Miranda, J. Suñé, “Memristors for neuromorphic circuits and artificial intelligence applications,” Materials, vol. 13, 938, 2020. DOI: 10.3390/ma13040938

[7] F. Zahoor, T. Azni Zulkifli, F. Khanday, “Resistive random access memory (RRAM): an overview of materials, switching mechanism, performance, multilevel cell (MLC) storage, modeling, and applications”, Nanoscale Res Lett, vol. 15, 90, 2020. DOI: 10.1186/s11671-020-03299-9

[8] V. Lähteenlahti, A. Schulman, A. Beiranvand, H. Huhtinen, P. Paturi, “Electron doping effect in the resistive switching properties of $Al/Gd_{1-x}Ca_xMnO_3/Au$ memristor devices,” ACS Appl. Mater. Interfaces, vol. 13, pp. 18365-18371, 2021. DOI: 10.1021/acsami.1c02963

[9] R. Yang, X. Li, M. Yu, X. Gao, X. Liu, X. Cao, Q. Wang, L. Chen, “Stable bipolar resistance switching behaviour induced by a soft breakdown process at the $Al/La_{0.7}Ca_{0.3}MnO_3$ interface,” J Phys D: Appl Phys, vol. 42, 175408, 2009. DOI: 10.1088/0022-3727/42/17/175408

[10] F. Chiu, “A review on conduction mechanisms in dielectric films,” Adv Mater Sci Eng, vol. 2014, 578168 (2014). DOI: 10.1155/2014/578168

[11] E. Miranda et al., "Soft breakdown conduction in ultrathin (3-5 nm) gate dielectrics," IEEE Transactions on Electron Devices, vol. 47, no. 1, pp. 82-89, 2000. DOI: 10.1109/16.817571

[12]G. Cellere, L. Larcher, M. G. Valentini and A. Paccagnella, "Micro breakdown in small-area ultrathin gate oxides," IEEE Transactions on Electron Devices, vol. 49, no. 8, pp. 1367-1374, 2002. DOI: 10.1109/TED.2002.801443

[13] E. Miranda, J. Suñé, “Memristive state equation for bipolar resistive switching devices based on a dynamic balance model and its equivalent circuit representation,” IEEE Trans Nanotech, vol. 19, pp. 837-840, 2020. DOI: 10.1109/TNANO.2020.3039391

[14] E. Miranda, “Compact model for the major and minor hysteretic I-V loops in nonlinear memristive devices,” IEEE Trans Nanotech, vol. 14, pp. 787-789, 2015. DOI: 10.1109/TNANO.2015.2455235

[15] D. Strukov, G. Snider, D. Stewart, and R. S. Williams, “The missing memristor found,” Nature, vol. 453, pp. 80–83, 2008. DOI: 10.1038/nature06932

[16] LTspice simulation software, https://www.analog.com

[17] L. O. Chua and Sung Mo Kang, "Memristive devices and systems," in Proceedings of the IEEE, vol. 64, no. 2, pp. 209-223, 1976. DOI: 10.1109/PROC.1976.10092

TURUN YLIOPISTO
UNIVERSITY OF TURKU

ISBN 978-951-29-9072-6 (PRINT)
ISBN 978-951-29-9073-3 (PDF)
ISSN 0082-7002 (PRINT)
ISSN 2343-3175 (ONLINE)

Painosalama Oy, Turku, Finland 2022